THE PRODUCTION AND DETECTION OF OPTIMIZED LOW-Z LINEAR ACCELERATOR TARGET BEAMS FOR IMAGE GUIDANCE IN RADIOTHERAPY

by

David D. M. Parsons

Submitted in partial fulfilment of the requirements
for the degree of Master of Science

at

Dalhousie University
Halifax, Nova Scotia
August 2012

DALHOUSIE UNIVERSITY

DEPARTMENT OF PHYSICS AND ATMOSPHERIC SCIENCE

The undersigned hereby certify that they have read and recommend to the Faculty of Graduate Studies for acceptance a thesis entitled “THE PRODUCTION AND DETECTION OF OPTIMIZED LOW-Z LINEAR ACCELERATOR TARGET BEAMS FOR IMAGE GUIDANCE IN RADIOTHERAPY” by David D. M. Parsons in partial fulfilment of the requirements for the degree of Master of Science.

Dated: August 22, 2012

Supervisor: _____

Dr. James L. Robar

Readers: _____

Dr. Christopher Thomas

_____

Dr. Laurent Kreplak

DALHOUSIE UNIVERSITY

DATE: August 22, 2012

AUTHOR: David D. M. Parsons

TITLE: THE PRODUCTION AND DETECTION OF OPTIMIZED LOW-Z LINEAR ACCELERATOR TARGET BEAMS FOR IMAGE GUIDANCE IN RADIOTHERAPY

DEPARTMENT OR SCHOOL: Department of Physics and Atmospheric Science

DEGREE: MSc CONVOCATION: October YEAR: 2012

_____

David D. M. Parsons

Table of Contents

LIST OF TABLES vii

LIST OF FIGURES viii

ABSTRACT xiii

LIST OF ABBREVIATIONS USED xiv

ACKNOWLEDGEMENTS xvii

Chapter 1 INTRODUCTION 1

1.1 PREFACE 1

1.2 IMAGING IN RADIATION THERAPY 3

1.3 MEGAVOLTAGE IMAGING USING LOW-Z TARGETS 5

1.4 DETECTOR OPTIMIZATION 7

Chapter 2 RADIOLOGICAL PHYSICS AND BEAM GENERATION 10

2.1 CHARGED PARTICLE INTERACTIONS WITH MATTER 10

2.1.1 Soft Collisions 12

2.1.2 Hard Collisions 12

2.1.3 Radiative Collisions 13

2.1.4 Stopping Power 14

2.1.5 CSDA Range 18

2.2 BREMSSTRAHLUNG PRODUCTION 19

2.3 PHOTON INTERACTIONS WITH MATTER 23

2.3.1 Compton Scattering 25

2.3.2 Photoelectric Effect 28

2.3.3 Pair Production 30

2.3.4 Rayleigh Scattering 32

2.3.5 Summary of Photon Interactions 33

Chapter 3 BEAM GENERATION IN A LINEAR ACCELERATOR 36

Chapter 4 X-RAY DETECTION AND MEASUREMENT 41

4.1 Thermoluminescence Dosimetry **41**
4.2 Ionization Chamber Dosimetry **43**
4.2.1 Percent Depth Dose 45
4.3 Semiconductor Dosimetry **48**
4.4 Electronic Portal Imaging Devices **49**
Chapter 5 MONTE CARLO SIMULATIONS **52**
5.1 Introduction **52**
5.2 EGSnrc **54**
5.3 Variance Reduction Techniques **58**
Chapter 6 IMAGING PHYSICS **61**
6.1 Introduction **61**
6.2 Fourier Slice Theorem and Filtered Backprojection **62**
6.2.1 Parallel Ray Reconstruction 65
6.3 CT Reconstruction **67**
6.3.1 Fan-Beam Reconstruction 68
6.3.2 Cone-Beam Reconstruction 69
Chapter 7 MATERIALS AND METHODS **71**
7.1 Low-Z Target Beam Production **71**
7.1.1 Beam Tuning 72
7.1.2 Electron Energy Determination 74
7.1.3 Photon Measurements 76
7.1.4 Photon Monte Carlo Simulations 76
7.2 Imaging System and Image Quality **78**
7.2.1 aS1000/IAS3 Image System 78
7.2.2 Contrast-to-Noise Ratio 79
7.2.3 Relative Modulation Transfer Function 80
7.3 Planar Image Quality below 2.4 MeV **81**
7.3.1 Contrast-to-Noise Ratio 81
7.3.2 Spatial Resolution 83
7.3.3 Qualitative Planar Imaging 84
7.4 The Effect of Copper in the IDU20 ..... **85**

7.4.1 Monte Carlo Simulations 85
7.4.2 Planar Image Quality – Physical Measurement 87
7.4.3 Cone Beam CT Image Quality 88

Chapter 8 RESULTS AND DISCUSSION 91

8.1 Beam Current Maximization 91

8.2 Incident Electron Energy 92

8.3 Photon Beam Characteristics 93

8.4 Planar Image Quality 98

8.4.1 Contrast-to-Noise Ratio 98
8.4.2 Spatial Resolution 101
8.4.3 Qualitative Imaging 102

8.5 Monte Carlo Characterization of the IDU20 with Copper Thickness 105

8.6 Planar Image quality with Copper Thickness 108

8.6.1 Contrast-to-Noise Ratio 108
8.6.2 Spatial Resolution 109
8.6.3 Qualitative Imaging 110

8.7 Cone Beam CT Image Quality with Copper Thickness 112

8.7.1 Contrast-to-Noise Ratio 112
8.7.2 Qualitative Imaging 114

Chapter 9 CONCLUSIONS 117

9.1 Summary of Work 117

9.1.1 Beam Optimization 117
9.1.2 Detector Optimization 118

9.2 Current and Future Work 118

9.2.1 Volume-of-Interest CBCT 118
9.2.2 Integration of Low-Z beams to treatment planning software 119
9.2.3 Crystalline Based Detector Imaging 119
9.2.4 Integration with TrueBeam 119

BIBLIOGRAPHY 121

LIST OF TABLES

Table 2.1 Photon interactions in the radiotherapy energy domain and their associated energy ranges in tissue[4,5,26]. 24

Table 2.2 Main characteristics of Rayleigh, photoelectric, Compton and pair production[4–6] 33

Table 6.1 Properties of tissue constituents of the human body[6] 62

LIST OF FIGURES

Figure 1.1 An example of a 6 MV spectral distribution and subplot of the relative spectral distribution in the diagnostic energy domain (25 to 150 keV). 4

Figure 2.1 The three charged particle interactions[5] with matter including hard (b ≈ a), soft (b >> a) and radiative collisions (b << a). Illustrated is the atomic nucleus encompassed by the classical atomic radius a, an electron's trajectory and corresponding classical impact parameter b and a bremsstrahlung photon of energy hv. 10

Figure 2.2 Monte Carlo simulation using the DOSXYZnrc user code of five 1 MeV electrons incident on a homogeneous cube of water. Also shown are ejected delta rays…… 12

Figure 2.3 The mass radiative (thick lines) and collisional (thick dashed lines) stopping powers plotted against electron kinetic energies for tungsten, aluminum, carbon and water. Data was obtained from the National Institute of Standards and Technology (NIST), Washington, DC[25]. 17

Figure 2.4 An illustration of an electrons path through a medium[4–6]. 18

Figure 2.5 Bremsstrahlung characteristic angle (θ_{max}) plotted against electron kinetic energy[5]. 23

Figure 2.6 Relative atomic cross section for photoelectric effect ($_a\tau$), Compton effect ($_a\sigma$) and pair production ($_a\kappa$) as a function of photon energy and the atomic number of the absorbing medium[4,5]. 25

Figure 2.7 The Compton scatter with an incident photon with energy hv, scattered photon with energy hv' and Compton recoil electron with kinetic energy E_K.[4,5]..... 26

Figure 2.8 The photoelectric interaction of a photon with energy hv with an orbital electron with a binding energy of E_b. The electron is ejected from the atom with kinetic energy E_K[4,5]. 29

Figure 2.9 Pair production within the Coulomb field of the nucleus[4,5]..... 31

Figure 2.10 Mass attenuation coefficient μ/ρ plotted against photon energy $h\nu$ in the energy range of 1 keV to 100 MeV for water. Also shown are the individual coefficients for Rayleigh scattering (η/ρ), photoelectric effect (τ/ρ), Compton scattering (σ/ρ) and pair production including triplet production (κ/ρ). Data was obtained from the National Institute of Standards and Technology (NIST), Washington, DC[27]. 34

Figure 2.11 Measurement of exponential photon attenuation in a narrow beam geometry[4,5]. 35

Figure 3.1 A triode electron gun showing the cathode, grid, anode and their associated voltage ranges as well as electron trajectories within the gun[28]. 37

Figure 4.1 Geometry for measurement of PDD distributions. D is the measured dose at a depth z normalized to the maximum measured dose D_{max} at depth z_{max}, for a given field size A and source-to-source distance f. 46

Figure 4.2 Monte Carlo simulated PDD curves of a clinical 6 MV photon beam and 4 MeV electron beam. Illustrated on the 6 MV plot are the surface dose, $D_{surface}$, the maximum dose D_{max} and corresponding depth z_{max}, the exit dose, D_{exit}, and the buildup region. Illustrated on the 4 MeV plot is the practical range, R_p, the maximum range, R_{max}, and the 90% and 50% dose depths, R_{90} and R_{50}, respectively….. 48

Figure 4.3 A typical amorphous silicon (a-Si) EPID composed of a high-Z buildup plate, scintillating phosphor and a photodiode array. Also shown are megavoltage photons incident on the EPID, producing scattered photons and secondary electrons through Compton events. The secondary electrons are interacting with the phosphor to produce visible light, which can be detected by the photodiodes…… 50

Figure 5.1 An illustration of Comte de Buffon's needle problem. 53

Figure 5.2 BEAMnrc simulation of a 6 MV Varian Clinac with electrons incident on a tungsten and copper target with bremsstrahlung photons (yellow). Shown (from the top down) is the primary collimator and target (FLATFILT), flattening filter (FLATFILT), monitor chamber (SLABS), mirror (MIRROR), Y and X jaws (JAWS) and mylar exit window (SLABS)..... 57

Figure 6.1 Mass attenuation coefficients in the diagnostic and therapeutic energy domain for cortical bone, skeletal muscle and fat (adipose). Inserted figure shows the normalized mass attenuation coefficients for bone and fat, bone and muscle and muscle and fat. Data was obtained from the National Institute of Standards and Technology (NIST), Washington, DC[27]. 61

Figure 6.2 An object f(x,y) being irradiated by parallel rays to form a projection $P_\theta(t)$ at angle θ[43]. 63

Figure 6.3 Simple backprojection with increasing projections to show improvement in the reconstructed image. 65

Figure 6.4 An example of filtered and unfiltered backprojection and the resulting image quality of each. The figure was taken with permission from *The Scientist and Engineer's Guide to Digital Signal Processing*[44]. 66

Figure 6.5 (a) Fan-beam computered tomography and (b) cone-beam computered tomography. 67

Figure 6.6 Projection of the cone-beam data $R_\beta(\beta,u,v)$ at point (u,B) back onto the scanning plane (t,u) at point x'. 70

Figure 7.1 The two low-Z targets used to produce photon beams below 2.40 MeV. Shown are the 2.35 MeV carbon target, aluminum target and the 2.35 MeV carbon target in its aluminum holder. 71

Figure 7.2 Low-Z target being installed in the linac carousel. 72

Figure 7.3 BEAMnrc simulation of 2.35 MeV electrons (blue) incident on a tantalum electron scattering foil with bremsstrahlung photons (yellow). Shown (from the top down) is the primary collimator (FLATFILT), Ta scattering foil (FLATFILT), monitor chamber (SLABS), mirror (MIRROR), jaws (JAWS), mylar exit window (SLABS) and the electron applicator (PYRAIMDS). 75

Figure 7.4 Monte Carlo simulation of the Varian 2100EX Clinac with the therapeutic target and flattening filter removed and a carbon target placed at the level of the flatterning filter….. 78

Figure 7.5 The CNR phantom with tissue equivalent inserts. 80

Figure 7.6 The experimental setup for planar imaging. 83

Figure 7.7 The QC3 phantom with spatial resolution regions shown. 84

Figure 7.8 Diagram of the full imaging system, (a) A schematic drawing on the linac and detector. (b) A photo of the detector with the cover off with copper plates and Cerrobend weights. 86

Figure 7.9 The setup for CBCT imaging: the object (sheep head) on the rotation stage situated between the linac head and IDU20. 89

Figure 7.10 The CNR phantom used for CBCT with the tissue substitute materials. 90

Figure 8.1 MU rate in relation to electron energy for both electrons and photons. The upper plot shows observed MU rate with tantalum scattering foil in place. The lower plot shows observed MU rate with aluminum and carbon targets in place. Error bars are generated from the observed variation in MU rates. 92

Figure 8.2 Experimental (curves) and Monte Carlo (points) electron percent depth dose curves ranging from 1.90 MeV to 2.35 MeV. 93

Figure 8.3 Percent depth doses for both aluminum and carbon targets are shown as well as corresponding Monte Carlo modeled depth dose curves for the aluminum target…..... 95

Figure 8.4 Monte Carlo generated spectral distributions for carbon and aluminum targets over the diagnostic energy range (25 to 150 keV), for the maximum and minimum energies used..... 96

Figure 8.5 Left figure shows Monte Carlo generated spectral distributions for the beryllium exit window and the carbon and aluminum targets, at 2.35 MV. Right figure shows Monte Carlo generated spectral distributions at 2.35 MV for the carbon target with various thickness of copper (on the exit side) and the percentage of photons with energy less than 25 keV..... 97

Figure 8.6 Planar images of the cortical bone insert at 2.35 MV with both aluminum and carbon targets and 6 MV therapeutic beam at 0.01, 0.05 and 0.10 cGy for both thin (3 cm) and thick (15 cm) phantoms. 98

Figure 8.7 Contrast-to-noise ratio results of the thin (3 cm) phantom for the four materials used at 1.90, 2.15 and 2.35 MV with both aluminum and carbon targets. For comparison, a 6 MV therapy beam is also shown. 99

Figure 8.8 Contrast-to-noise ratio results of the thick (15 cm) phantom for the four materials used at 1.90, 2.15 and 2.35 MV with both aluminum and carbon targets. For comparison, a 6 MV therapy beam is also shown. 101

Figure 8.9 Relative modulation transfer function for 1.90, 2.15 and 2.35 MV/Carbon beams and a 6 MV therapeutic beam. 102

Figure 8.10 Planar sagittal images of a sheep head at 2.35 MV with both carbon and aluminum targets and a 6 MV therapeutic beam. 104

Figure 8.11 a) shows the diagnostic spectral distribution with 0 mm, 0.4 mm, 1.0 mm and 1.6 mm of copper present in the detector for 2.35 MV/Carbon and 7.00 MV/Carbon beams. b) shows the percentage of photons within the diagnostic energy domain (25 to 150 kV) at the phosphor surface as a function of copper thickness. 105

Figure 8.12 Response curves for 0 mm, 1.0 mm and 1.6 mm thick copper layers within the IDU20 and photon energy fluence produced with the 2.35 MV/Carbon and 7.00 MV/Carbon beams. 106

Figure 8.13 Planar image contrast-to-noise ratio as a function of copper thickness for both 2.35 MV/Carbon and 7.00 MV/Carbon beams, for cortical bone 60% (top-left), cortical bone 30% (top-right), inner bone (middle-left), brain (middle-right) and lung (bottom-left). 109

Figure 8.14 Relative modulation transfer function (RMTF) for 0.0mm, 1.0 mm and 1.6 mm thick copper layers in the IDU20 detector for 2.35 MV/Carbon and 7.00 MV/Carbon beams. 110

Figure 8.15 Planar imaging of a sheep head at 0.26 cGy (at isocenter) for both 0.0 mm (right) and 1.0 mm (left) of copper within the detector at both 2.35 (bottom) and 7.00 MV/Carbon (top). For comparison, the images where normalized to the pixel value at a point within all the images and with identical gray level window settings…. 111

Figure 8.16 Profiles of figure 8.15 with and without the copper conversion plate within the detector for 2.35 MV/Carbon and 7.00 MV/Carbon beams. 112

Figure 8.17 Cone beam computed tomography images at approximately 4.1 cGy with copper plate (top) and without copper (bottom) in the detector, with the 7.00 MV/Carbon and 2.35 MV/Carbon beams. 113

Figure 8.18 Contrast-to-noise ratios of tissue substitutes in CBCT images as a function of dose, comparing the 2.35 MV/Carbon and 7.00 MV/Carbon beams both with and without copper present in the detector. 114

Figure 8.19 CBCT images of a sheep head at approximately 4.1 cGy (at isocenter) with copper plate (top) and without copper (bottom) in the detector, the 7.00 MV/Carbon (left) and 2.35 MV/Carbon (center) beams. The two images on the right are magnified views of the nasal cavity for the 2.35 MV/Carbon beam. 116

ABSTRACT

Recent work has demonstrated improvement of image quality with low atomic number (Z) linear accelerator (linac) targets and energies as low as 3.5 MV compared to a standard 6 MV therapeutic beam. In this work, the incident electron beam energy has been lowered to energies between 1.90 and 2.35 MeV. The improvement of megavoltage planar image quality with the use of carbon and aluminum linac targets has been assessed and compared to a standard 6 MV therapeutic beam.

Common electronic portal imaging devices (EPIDs) contain a 1.0 mm copper conversion plate to increase detection efficiency of a therapeutic megavoltage spectrum. When used in imaging with a photon beam generated with a low-Z target, the conversion plate attenuates a substantial proportion of photons in the diagnostic energy range (25 to 150 keV), thereby reducing the achievable image quality. Also in this work, image quality as a function of copper plate thickness has been assessed for both planar imaging and cone beam computed tomography (CBCT).

The bending magnet shunt current was adjusted to allow the selection of mean electron energy between 1.90 and 2.35 MeV. Linac set points were altered to increase beam current to allow experimental imaging in a practical time frame.

Electron energy was determined through comparison of measured and Monte Carlo modeled depth dose curves. Planar image contrast-to-noise ratio (CNR) and spatial resolution measurements were performed to quantify the improvement of image quality with energy and copper thickness. CNR measurements were taken as a function of dose for CBCT imaging both with and without the copper plate present in the EPID. Magnitudes of improvement are explained with reference to Monte Carlo generated energy spectra.

After modifications to the linac, beam current was increased by a factor greater than four compared to the unaltered beam. Incident electron energy was determined to have an adjustable range from 1.90 MeV to 2.35 MeV. CNR of cortical bone was increased by a factor ranging from 6.2 to 7.4 and 3.7 to 4.3 for thin and thick phantoms, respectively, compared to a 6 MV therapeutic beam for both aluminum and carbon targets. Spatial resolution was degraded slightly, with a relative change of 3% and 10% at 0.20 lp/mm and 0.40 lp/mm, respectively, when reducing electron energy from 2.35 to 1.90 MV with a carbon target. The percentage of diagnostic energy x-rays for the energy spectra examined here, ranges from 46% to 54%.

The removal of copper in the EPID increased the diagnostic photon population reaching the phosphor by up to 20% and intensified the peak detector response (dose per incident particle deposited in the scintillator) at 60 keV by a factor of 6.4. Planar CNR was increased by a factor ranging from 1.4 to 4.0, depending on the material imaged. Planar spatial resolution was only slightly degraded with increasing copper thickness. Increases in CBCT image CNR ranged from a factor of 1.3 to 2.1 with the copper plate removed.

This study presents an optimized beam and detector for imaging using a 2.35 MV/Carbon beam line and copper-less EPID.

LIST OF ABBREVIATIONS USED

2D	Two-dimensional
3D	Three-dimensional
a-Si	Amorphous silicon
AEIT	Approximate efficiency improving technique
CBCT	Cone-beam computed tomography
CHT	Condensed history technique
CM	Component module
CNR	Contrast-to-noise ratio
CSDA	Continuously slowing down approximation
CT	Computed tomography
DRR	Digitally reconstructed radiograph
DSB	Directional bremsstrahlung splitting
D_{exit}	Exit dose
D_{max}	Maximum dose
$D_{surface}$	Surface dose
ECUT	Electron transport cutoff energy
EGS	Electron gamma shower
EPID	Electronic portal imaging device
f_{50}	Frequency where RMTF equals 0.5
FDK	Feldkamp Davis Kress
FOI	Field-of-interest

Gd_2O_2S:Tb	Gadolinium oxysulfate doped with terbium
HDR	High dose rate
HV	High voltage
ICRU	International Commission on Radiation Units and Measurements
IGRT	Image guided radiation therapy
IMRT	Intensity modulated radiotherapy
keV	kilo electron volt
kV	kilovoltage
LET	Linear energy transfer
Linac	Linear accelerator
MeV	Mega electron volt
MLC	Multileaf collimator
MU	Monitor unit
MV	Megavoltage
NIST	National Institute of Standards and Technology
NRC	National Research Council of Canada
PCUT	Photon transport cutoff energy
PDD	Percent depth dose
R_{50}	Depth of 50% PDD
R_{90}	Depth of 90% PDD
RF	Radiofrequency
R_{max}	Maximum range

RMTF	Relative modulation transfer function
R_p	Practical range
SBS	Selective bremsstrahlung splitting
SDD	Source-to-detector distance
SLAC	Stanford Linear Accelerator Center
SSD	Source-to-surface distance
TLD	Thermoluminescent dosimeter
UBS	Uniform bremsstrahlung splitting
VMAT	Volumetric modulated arc therapy
VOI	Volume-of-interest
Z	Atomic number
Z_{eff}	Effective atomic number
z_{max}	Depth of maximum PDD
ρ_e^w	Electron density relative to water

ACKNOWLEDGEMENTS

First off I would like to thank my supervisor, Dr. James L. Robar for his guidance, support and for all of the opportunities he has encouraged me to pursue. I'm extremely grateful for all of our discussions and your patience we me throughout them. I cannot believe all that I have experienced, learned and accomplished over the last two years; it has exceeded my every expectation.

I would like to thank Robert Moran for all of his late nights with me on the EX. His knowledge, expertise and technical support were vital to this project.

Thank you Drs. Chris Thomas, Edwin Sham, Mammo Yewondwossen, and Robin Kelly for sharing your knowledge with me over the last two years.

I would like to thank Ian Porter for fabrication of apparatus used in this project. Jim Allen and Joanna Mader thank you for your help with the tedious TLDs.

I would also like to thank my friends for providing many good memories and keeping me sane.

Lastly, I would like to thank my parents for all of their encouragement and support.

CHAPTER 1 INTRODUCTION

1.1 Preface

Cancer as described by Hall and Giaccia[1] is the general name for more than 100 diseases in which abnormal cells grow out of control and have the ability to infiltrate and destroy normal body tissue. According to the Canadian Cancer Society, Statistics Canada and the Public Health Agency of Canada, in 2012 there will be approximately 186 400 new cases of cancer and 75 700 deaths from cancer in Canada[2]. Furthermore in 2007, cancer accounted for approximately 30% of all deaths in Canada[2]. There are currently numerous types of treatments for cancer such as: surgery, radiation therapy, chemotherapy, hormone therapy and biological therapies. The treatment type used often depends on the site of origin, histological considerations and the extent of the disease.

Radiation therapy employs ionizing radiation to treat patients with cancer alone or in combination with other treatment modalities, this branch of medicine is known as radiation oncology. The objective of radiation therapy is to deliver a precise dose of radiation to a defined target volume with as small of dose as possible to the surrounding healthy tissue, with the goal of eradicating the cancer with minimal side effects to the patient. Nearly two-thirds of all cancer patients receive some form of radiation therapy as part of their treatment[3].

There are two modalities used in radiation therapy to delivery the radiation to the patient: brachytherapy and teletherapy. Brachytherapy involves placing sources of radiation within or adjacent to the target volume. The sources can be placed permanently or temporarily. Permanent implants generally emit low energy radiation; common sources include iodine 125, palladium 103 and gold 198. Temporary implants are currently performed with a high dose rate (HDR), called HDR brachytherapy, with treatments lasting on the order of a few minutes. The most common HDR source is iridium 192. In teletherapy or external beam radiotherapy radiation is administered at some distance from the body. The most common source of radiation used in external beam radiotherapy is of bremsstrahlung photons produced by accelerating electrons in a medical linear accelerator and colliding them on to a high atomic number (Z) target. As stated previously, the goals of radiation therapy are to delivery a precise dose of radiation to a target volume and spare the surrounding healthy tissue. Due to the nature of external beam radiotherapy, localization of the target volume within the patient can be difficult. As a result of the sharp dose gradients produced by today's treatment modalities (IMRT and VMAT), incorrect alignment of the patient by several millimeters could result in serious complications. Currently, images of the patient are taken prior to or during radiotherapy to determine if the patient is correctly aligned relative to isocenter, this is called image-guided radiation therapy (IGRT).

1.2 IMAGING IN RADIATION THERAPY

In the past, megavoltage (MV) portal imaging has been used to align a patient's position for radiation therapy. MV portal imaging is typically acquired using a 6 MV therapeutic beam and an electronic portal imaging device (EPID). In MV portal imaging two orthogonal images are taken to align the patient's internal anatomy to the computed tomography (CT) image set taken during CT simulation for treatment planning. However, these MV images have inherently poor contrast compared to the CT images. This is largely due to the absence of diagnostic quality photons in a 6 MV spectrum (Fig. 1.1), as highlighted in the sub figure showing fractional fluence in the diagnostic energy domain. As a result, Compton interactions are dominant when the 6 MV beam interacts in the patient's body. The Compton effect is independent of atomic number (Z) and depends on the electron density of the medium. In our bodies electron densities vary little between tissues[6]. As a result MV images have inherently poor image contrast.

In a Varian linear accerator, the 6 MV photon beam is produced by 6.45 MeV electrons incident on a tungsten and copper target and attenuated by a copper flattening filter. As a result of the photoelectric effect being dominant within the diagnostic energy range (25 to 150 keV) and its Z^3 dependence[4–6], most of the diagnostic quality photons generated are absorbed locally within the target or further downstream in the flattening filter. Orton and Robar[7] have shown that within a typical 6 MV spectrum only 0.3% of the total photon population is within the diagnostic energy

range. With diagnostic energy photons removed from the spectrum, Compton interactions are dominant when the 6 MV beam interacts in the patient's body.

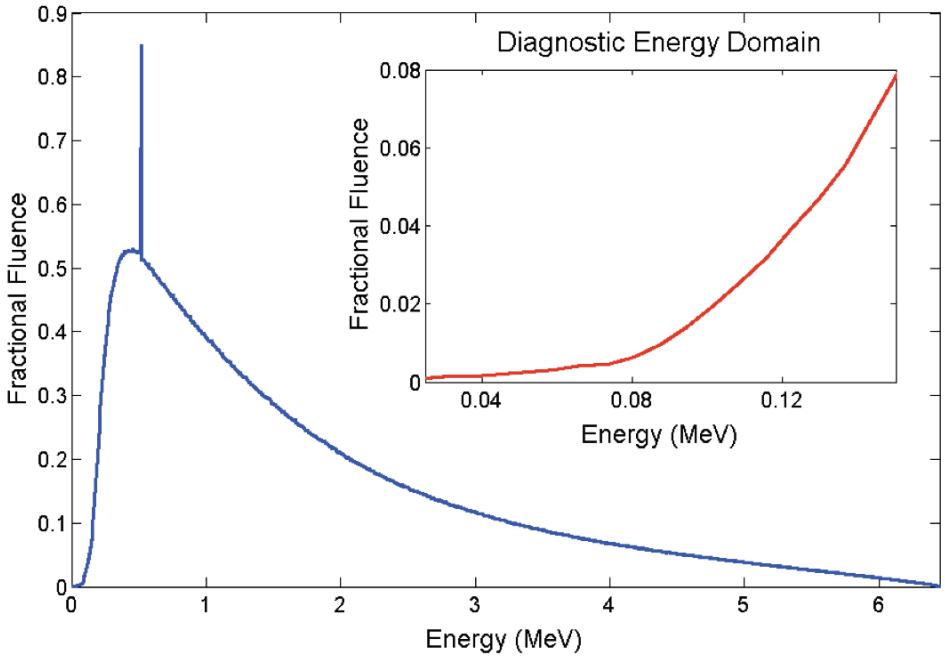

Figure 1.1 An example of a 6 MV spectral distribution and subplot of the relative spectral distribution in the diagnostic energy domain (25 to 150 keV).

The introduction of a diagnostic quality x-ray tube and detector, orthogonal to the therapy beam line[8] has largely replaced portal imaging as a means for image guided radiation therapy. While the use of this technology for planar imaging and cone beam computed tomography (kV CBCT) has greatly improved available image quality, it also involves greater cost, increased quality assurance and does not allow for beam's eye viewing. Beam's eye views are projections of the treatment beam axis, field and structures through the patient. Beam's eye view images are important, as they allow comparison of the beam collimation relative to the patient's anatomy.

1.3 MEGAVOLTAGE IMAGING USING LOW-Z TARGETS

Several groups have shown that the removal of the high-Z target and flattening filter from the therapy beam line and the introduction of a low-Z target can greatly enhance image quality compared to standard megavoltage therapy beams[9–13]. Most recently, Faddegon *et al.*[14] used a 1.32 cm thick carbon target placed in the high-energy electron scattering port of a high-energy linac with 4.2 MeV electrons incident on the target. This work showed that soft tissue contrast-to-noise ratio (CNR) was improved up to a factor of three in CBCT images compared to a 7.0 MV treatment beam line. Similarly, Roberts *et al.*[15] used a 2 cm thick carbon and nickel target placed in the high-energy collimator port of high-energy linac operating in 4 MeV electron mode with the primary and secondary scatter foils removed. This work showed that the megavoltage planar image contrast of dense bone in water was improved by a factor of 4.62 for thin phantoms (5.8 cm thick) and 1.3 for thicker phantoms (25.8 cm). Spatial resolution was improved when compared to the 6 MV therapy beam. Orton and Robar[7] modeled 6.0 MeV electrons incident on an aluminum and beryllium low-Z targets in a high-energy linac, with a QC3 phantom and 25-layer aS500 detector, demonstrating a contrast enhancement factor ranging from 1.6 to 2.8. Sawkey *et al.*[16] showed a 25% increase in contrast when decreasing the electron energy from 6 MeV to 4 MeV on a diamond target in a high-energy linac, with no appreciable change in spatial resolution. Similarly Robar *et al.*[17] showed CNR increases by factors ranging from of 1.2 to 1.7 for 7.0 MeV electrons incident on an Al target compared to a 6 MV therapeutic beam, and when incident electron energy was decreased to 3.5 MeV, this factor increased, ranging from

2.7 to 3.8. Connell and Robar[18] showed that spatial resolution is improved with certain combinations of low-Z material and thickness compared a 6 MV therapy beam. A slight decrease in spatial resolution was observed when decreasing the incident electron from 7.0 to 4.5 MeV[18]. More recently, Fast *et al*.[19] has shown that CBCT CNR is increased by a factor of 2.6 when using the commercial version of the beam line described by Faddegon *et al*.[14] compared to the 6 MV treatment beam line, with no significant change in spatial resolution. Fast *et al*.[19] also show that the dose must be increased by a factor of 5 with the treatment beam to achieve the same image quality as the low-Z beam.

It is clear that by lowering the incident electron energy in combination with a low-Z target, for a given imaging dose, CNR can be greatly enhanced. To date, the lowest energy examined in a Varian linac with a low-Z target beam has been 3.5 MeV[17]; in this work the following issues are addressed: i) the amount by which the incident electron energy can be lowered in a standard high energy linac, and ii) the resultant gains in planar image CNR. Practical limitations with regard to the reduction of beam current with lowered energy are demonstrated. Photon beams are characterized by percentage depth dose, imaging CNR and energy spectral characteristics, for beams generated with carbon and aluminum targets, with incident electron beams with energies below 2.4 MeV.

1.4 Detector Optimization

The replacement of the high-Z target with a low-Z target[7,9–18] has been shown to increase the low energy component of the beam, thereby improving the available image quality in MV-CBCT and planar imaging[14,17,20–22]. While the majority of the research regarding low-Z targets has focused on target composition, incident electron energy and their resulting effects on image quality for either planar or CBCT imaging, relatively little has been reported[7,13–15,21,23] with regard to optimizing the detector for a low-Z target energy spectrum. A typical EPID is composed of a metal conversion plate (typically copper or steel), a detection receptor (typically a scintillating phosphor) and photodiode array. In MV imaging, photons interact with the metal conversion plate to produce Compton recoil electrons, which interact with the scintillating phosphor to produce visible light that can be detected by the photodiodes[24]. Compton recoil electrons are generated when a photon of energy hv interacts with a loosely bound orbital electron. In a Compton interaction, the electron and photon are scattered with energy E_K and hv', respectively, where hv' is less than hv. While a typical flattened 6 MV beam contains less than 0.3% of photons in the diagnostic energy range, this fraction increases to as much as 50% for a low-Z target beam[7]. While this component of the spectrum is the most useful from the point of view of image formation, it also has a high probability of absorption in the copper conversion plate.

Several groups have investigated the effect of detector composition on image quality in combination with low-Z targets. Orton and Robar[7] modeled 4 MeV and 6 MeV electrons incident on aluminum and beryllium low-Z targets in a high-energy linac, with

an aS500 detector (Varian Medical Systems, Inc.), demonstrating that the removal of the copper conversion plate can result in a contrast enhancement factor of 1.2, at both 4 MeV and 6 MeV. Faddegon *et al.*[14] qualitatively showed that MV-CBCT image quality could be increased with the removal of the copper conversion plate when using a carbon target with 4.2 MeV incident electrons. Roberts *et al.*[15] demonstrated that altering the detector receptor from Gb_2S_2O:Tb to CsI:Tl crystal can increase the detector response at 60 keV approximately fourfold. More recently Roberts *et al.*[21] showed a two fold increase in contrast by reducing the incident electron energy to 1.4 MeV in combination with a CsI:Tl crystalline scintillator detector compared to a 6 MV therapeutic beam and a standard megavoltage EPID in the thick water phantom. However, with the increase in image quality the associated cost of a crystalline scintillator is greatly increased, as is the complexity of manufacturing a crystalline detector without defects. In lieu of a crystalline scintillator, Breitbach *et al.*[23] showed that the copper conversion plate and Gb_2S_2O:Tb could be replaced with a segmented scintillator composed of a Gb_2S_2O ceramic called a sintered pixelated array. Using the same imaging beam line as Faddegon *et al.*[14], they showed that it is possible to increase the CNR in CBCT images by a factor of 1.64 compared to the unaltered EPID with no statistically significant change in spatial resolution.

It is clear that by altering the detector composition, it is possible to significantly affect image contrast and CNR. However, to date the effect the copper conversion plate has on image CNR in standard MV EPID detectors has yet to be measured quantitatively. Through measurement the following is investigated: i) the effect that the thickness of

the copper conversion plate has on a 2.35 and 7.00 MV/Carbon spectra and the associated detector response, and ii) the resultant changes in image quality, both qualitatively and quantitatively.

CHAPTER 2 RADIOLOGICAL PHYSICS AND BEAM GENERATION

In this chapter, the various interactions between particles of interest in megavoltage radiation therapy and imaging are discussed. Charged particle interactions with matter are discussed first, followed by photon interactions with matter.

2.1 CHARGED PARTICLE INTERACTIONS WITH MATTER

Charged particle interactions with matter occur when the electric field of a charged particle interacts with the electric field of either an orbital electron (collisional loss) or the nucleus (radiative loss)[5]. Charged particle interactions can be divided into 3 categories depending on the size of the classical impact parameter b in relation to the classical atomic radius a. As illustrated in figure 2.1, these categories are hard (b ≈ a), soft (b >> a) and radiative collisions (b << a) [5].

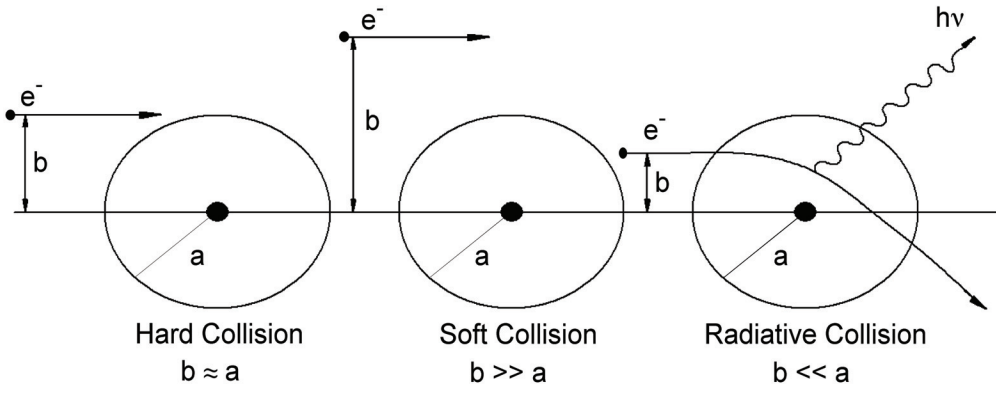

Figure 2.1 The three charged particle interactions[5] with matter including hard (b ≈ a), soft (b >> a) and radiative collisions (b << a). Illustrated is the atomic nucleus encompassed by the classical atomic radius a, an electron's trajectory and corresponding classical impact parameter b and a bremsstrahlung photon of energy hν.

Although most of these interactions can occur for all types of charged particles, for the purposes of this research, electrons are of particular interest. Electrons have a relatively low mass in comparison to other types of charged particles, such as a proton, which has a mass approximately 1836 times that of an electron. As a result, elastic scattering is more prevalent for electrons (or positrons) compared to heavy charged particles and this results in significant deflections. An example of this can be seen in figure 2.2, in which the paths of five 1 MeV electrons in water were simulated using the Monte Carlo technique. In a single collisional event the energy transferred from an electron to matter is generally small, and this results in many interactions with the medium until all of the charged particle's kinetic energy has been dissipated. The rate at which a charged particle transfers its kinetic energy to the medium is described by the stopping power. Stopping power[4,5] is the expectation value of the rate of energy loss per unit path length by a charged particle with a kinetic energy E_K in a medium with an atomic number of Z. Stopping power is composed of two terms or classes: collisional (ionization) stopping power that results from interactions with orbital electrons, and radiative stopping power that results from interactions with the nucleus. Stopping power depends on the charged particle's mass, charge, velocity and the atomic number of the medium[4,5].

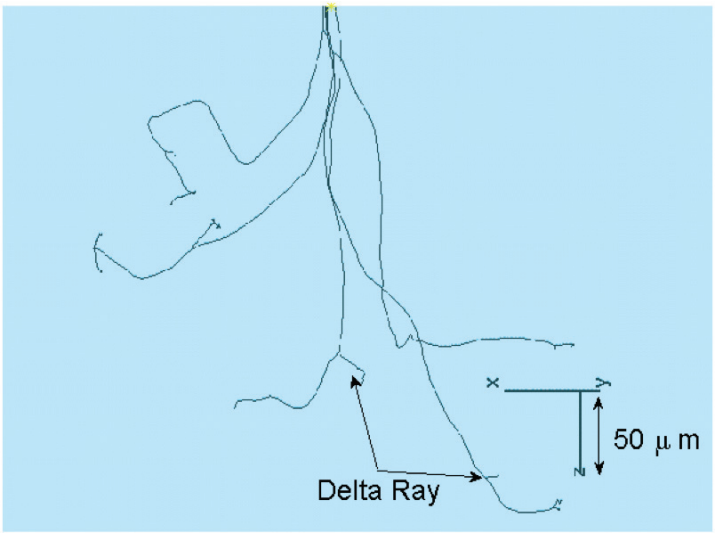

Figure 2.2 Monte Carlo simulation using the DOSXYZnrc user code of five 1 MeV electrons incident on a homogeneous cube of water. Also shown are ejected delta rays.

2.1.1 Soft Collisions

Soft collisions occur when a charge particle passes an atom at a considerable distance (b >> a). In a soft collision, the electric field of the charged particle distorts the Columbic field of the atom exciting it to a higher energy and sometimes ionizing it by ejecting a valence-shell electron. The typical energy transferred to the atom is on the order of a few eV, however due to the large values of b, soft collisions are by far the most numerous type of charged particle interaction with the medium and account for approximately half of the energy transferred to the medium[4,5].

2.1.2 Hard Collisions

Hard or "knock-on" collisions occur when the impact parameter is on the order of the atomic radius. In this scenario it becomes more likely that the charged particle will interact with a single atomic electron, thereby ejecting the electron from the atom with substantial kinetic energy. These ejected electrons, called delta rays, can then

deposit their kinetic energy in further Columbic force interactions along a separate path from the primary charged particle called a spur (Fig. 2.2). These interactions occur less frequently than soft collisions, however the fraction of the total charged particle's energy transferred to the atom is comparable between the two processes[4,5].

2.1.3 Radiative Collisions

Radiative collisions occur when the impact parameter of the charged particle is much smaller than the atomic radius. In this process, the electric field of the charged particle interacts directly with the electric field of the nucleus. In 97-98% of these interactions the charged particle is scattered elastically and does not emit an x-ray photon or excite the nucleus[4,5]. This process is not significant in transferring energy to the medium as only a small amount of kinetic energy is transferred to the medium to satisfy the conservation of momentum. In the other 2-3% of these collisions, an inelastic radiative interaction occurs in which an x-ray photon is emitted. In this process, the charged particle is deflected and can transfer up to 100% of its kinetic energy to the emitted photon[4,5]. These emitted photons are referred to as bremsstrahlung photons, German for "braking radiation." This interaction has a differential cross section that is proportional to Z^2 and the inverse square of the mass for a given velocity (see section 2.2, Bremsstrahlung Production). As a result of this relationship, this type of interaction is most important for electrons and positrons, and bremsstrahlung production by heavy charged particles is insignificant. The light charged particle's energy determines the characteristic angle of the produced bremsstrahlung photon. As the energy of the charged particle is increased, bremsstrahlung production becomes more forward

directed with an increased intensity compared to lateral scattering (see section 2.2, Bremsstrahlung Production).

2.1.4 Stopping Power

Linear stopping power is defined as the rate of kinetic energy loss per unit length by a charged particle in a medium. This can be divided by the density of the medium to give the mass stopping power, with units of MeV cm^2/g. Mass stopping power can be separated into two terms called collisional stopping power and radiative stopping power:

$$\left(\frac{dT}{\rho dx}\right)_{Total} = S_{Total} = S_{col} + S_{rad} \qquad \text{Eq 2.1}$$

Mass collisional stopping power results from charged particle Columbic interactions with orbital electrons of the absorber. For electrons and positrons the mass collisional stopping power can be expressed for both hard and soft collisions as:

$$S_{col} = \left(\frac{dT}{\rho dx}\right)_{col} = 2\pi r_e^2 \frac{Z}{A} N_A \frac{m_e c^2}{\beta^2}\left[\ln\frac{E_K}{I} + \ln\left(1+\frac{\tau}{2}\right) + F^{\pm}(\tau) - \delta\right] \qquad \text{Eq 2.2}$$

where

r_e is the classical electron radius,

N_A is Avogadro's number,

A is the number of nucleons,

m_e is mass of an electron,

β is the speed of the charged particle divided by the speed of light in a vacuum (v/c),

E_K is the kinetic energy of the charged particle,

I is the mean excitation potential,

τ is the electron or positron kinetic energy normalized to $m_e c^2$,

δ is the polarization function.

The function $F^{\pm}(\tau)$ depends upon the charge of the particle. For electrons, $F^{-}(\tau)$ is based on the Moller cross sections and is defined as:

$$F^{-}(\tau)=\left(1-\beta^2\right)\left[1+\frac{\tau^2}{8}-(2\tau+1)\ln 2\right], \qquad \text{Eq 2.3}$$

and for positrons, $F^{+}(\tau)$ is based on Bhabha cross sections and is defined as:

$$F^{+}(\tau)=2\ln 2-\frac{\beta^2}{12}\left[23+\frac{14}{\tau+2}+\frac{10}{(\tau+2)^2}+\frac{4}{(\tau+2)^3}\right]. \qquad \text{Eq 2.4}$$

In the simple geometry of charged particles striking a thin foil, the dose deposited by charged particles to the medium is a product of the charged particle fluence and the mass collisional stopping power.

Mass radiative stopping power describes the rate of energy deposition per unit length in a medium with density ρ caused by light charged particle Coulombic interactions with the nuclei of the absorber. Heavy charged particles, such as a proton, do not contain a mass radiative stopping power component due to their large mass (see section 2.2, Bremsstrahlung Production). S_{rad} is defined as:

$$S_{rad}=\left(\frac{dT}{\rho dx}\right)_{rad}=N_a\sigma_{rad}(E_K+m_e c^2), \qquad \text{Eq 2.5}$$

where

N_a is the number of atoms per unit mass ($N_a = N/m = N_A/A$),

σ_{rad} is the total cross section for bremsstrahlung production,

σ_{rad} varies depending upon the speed of the light charged particle.

For non-relativistic particles, equation 2.5 is defined as:

$$S_{rad} = \left(\frac{dT}{\rho dx}\right)_{rad} = \alpha r_e^2 Z^2 \frac{N_A}{A} B_{rad}(E_K + m_e c^2), \qquad \text{Eq 2.6}$$

where

α is the fine structure constant ($e^2/(4\pi\varepsilon_o\hbar c) \approx 1/137$),

B_{rad} is a slowly varying function of Z and E_K and has a value of 16/3 for non-relativistic light charged particles. B_{rad} has a value of approximately 6 at E_K = 1 MeV, 12 at E_K = 10 MeV and 15 at E_K = 100 MeV[4,5].

For all elements, with the exception of hydrogen, Z/A is approximately constant at 0.5; this means that S_{rad} is proportional to Z and E_K (for $E_K >> m_e c^2$). Figure 2.3 shows mass collisional and radiative stopping powers for the linear accelerator target materials used in this work (tungsten, aluminum and carbon) and water. This figure illustrates the dependence of the mass radiative stopping power to Z and E_K.

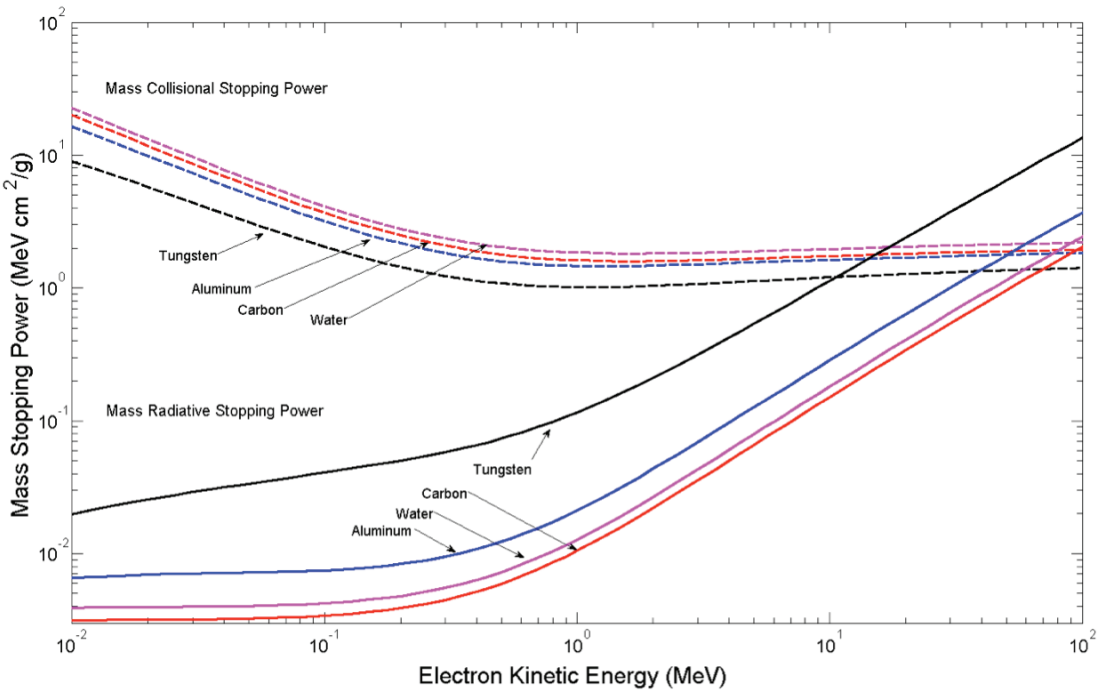

Figure 2.3 The mass radiative (thick lines) and collisional (thick dashed lines) stopping powers plotted against electron kinetic energies for tungsten, aluminum, carbon and water. Data was obtained from the National Institute of Standards and Technology (NIST), Washington, DC[25].

.

Mass collisional stopping power is the average rate of energy loss by a charged particle in all hard and soft collisions. However, under some circumstances the use of the mass collisional stopping power will overestimate the energy deposited in the medium, this is a result of delta rays resulting from hard collisions that may be energetic enough to transfer a large portion of energy a significant distance away from the primary track. This is particularly important when calculating the dose in a small object or thin foil[4,5]. The restricted mass stopping power is the fraction of the mass collisional stopping power that includes all the soft collisions plus those hard collisions that result in delta rays with an energy less than a cutoff value such that energy isn't carried away.

A form of the restricted mass stopping power is the linear energy transfer (LET). LET is described as:

$$\text{LET}\ \left(\text{units of } \frac{\text{keV}}{\mu\text{m}}\right) = \frac{\rho}{10}\left[\left(\frac{dT}{\rho dx}\right)_{\text{restricted}}\left(\text{units of } \frac{\text{MeV cm}^2}{\text{g}}\right)\right]. \qquad \text{Eq 2.7}$$

In equation 2.7, the divison of ρ by 10 is a result of changing units from MeV cm^2/g to keV/μm.

2.1.5 CSDA Range

The range of a charged particle in a medium is an experimental value of the thickness that a charged particle can just penetrate, as illustrated in figure 2.4[4–6]. It depends on the particles kinetic energy, mass, charge and the composition of the medium.

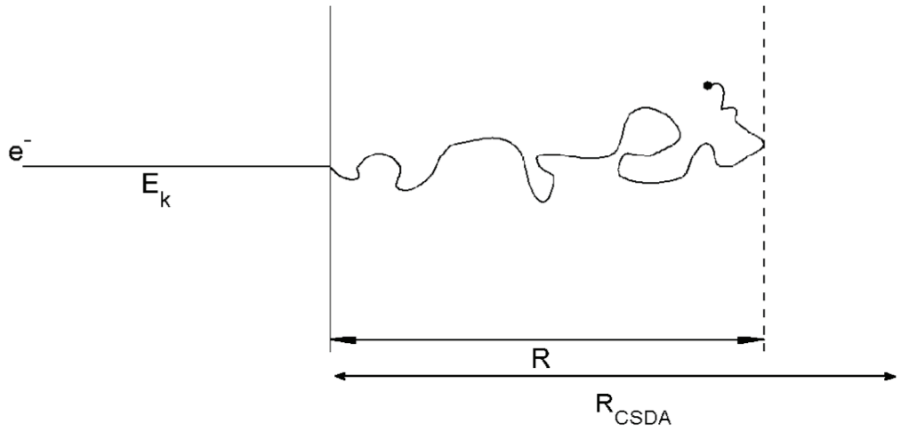

Figure 2.4 An illustration of an electrons path through a medium[4–6].

The range of a heavy charged particle in a medium is relatively simple to determine due to the relatively large mass prohibiting large angular deflections, with the heavy charged particle depositing most of its kinetic energy towards the end of its range, also known as a Bragg peak. In comparison, light charged particles can have significant deflections as a

result of elastic scattering, as previously observed in figure 2.2 and 2.4. As a result of this, the mean path length of the light charged particles can be difficult to determine. In 1983, Berger and Seltzer calculated a quantity called the CSDA (continuously slowing down approximation) range[4]. The CSDA range (R_{CSDA}) is defined as:

$$R_{CSDA} = \int_0^{E_K} dE \left(\frac{dT}{\rho dx}\right)^{-1}_{Total}. \qquad \text{Eq 2.8}$$

For electron and positrons the CSDA range can be up to twice the range, this is a result of elastic scattering that the electrons and positrons experience in the medium.

2.2 Bremsstrahlung Production

As described by Podgorsak[5], charged particles can be characterized as being in one of three states depending upon their velocity ($\vec{v}$) and kinetic energy (E_K). A charged particle can be described as either stationary ($\vec{v}$ = 0), moving with uniform velocity ($\vec{v}$ = constant) or accelerated with an acceleration $\vec{a} = d\vec{v}/dt$. When the charged particle is stationary its electric field, $\vec{E}$, is defined as:

$$\vec{E}(r) = \frac{1}{4\pi\epsilon_0}\frac{q}{r^2}, \qquad \text{Eq 2.9}$$

where

q is the charge of the charged particle,

r is the distance from the charged particle to the point of observation,

ϵ_0 is the permittivity of free space in vacuum (8.854 x 10^{-12} F/m).

With equation 2.9, the energy density, ξ, of a stationary charged particle can be defined as

$$\xi = \frac{1}{2}\epsilon_0 E^2, \qquad \text{Eq 2.10}$$

When the electron is moving at a uniform velocity, it has an accompanying magnetic field, $\vec{B}$, and equation 2.10 becomes:

$$\xi = \frac{1}{2}\epsilon_0 E^2 + \frac{1}{2\mu_0} B^2, \qquad \text{Eq 2.11}$$

where

μ_0 is the magnetic permittivity in vacuum ($4\pi \times 10^{-7}$ H/m).

However, if the charged particle is accelerated, the non-static electric and magnetic fields cannot adjust themselves in such a way that no energy is radiated away from the electron[5]. As a consequence of this, the charged particle emits some of its kinetic energy in the form of a bremsstrahlung photon. When the electron is accelerated, at far distances from the charged particle, equation 2.9 becomes:

$$\vec{E}(r) = \frac{1}{4\pi\epsilon_0}\frac{q}{c^2}\frac{\vec{a}\sin\theta}{\vec{r}}, \qquad \text{Eq 2.12}$$

where θ is the angle between the point of observation and the charged particle.

At this time, the electric and magnetic fields propagate outward with velocity c and form a bremsstrahlung photon. The intensity of the bremsstrahlung photon, $I(r,\theta)$, is determined by the Poynting vector, $\vec{S}$, where:

$$\vec{S} = \vec{E} \times \frac{\vec{B}}{\mu_0}. \qquad \text{Eq 2.13}$$

Recognizing that the electric and magnetic fields are perpendicular to one another and that $\vec{B} = \vec{E}/c$ and $c^2 = 1/\epsilon_0\mu_0$, the Poynting vector simplifies to:

$$\left|\vec{S}\right| = I(r,\theta) = \epsilon_0 c E^2 = \frac{1}{16\pi^2\epsilon_0}\frac{q^2a^2}{c^3}\frac{\sin^2\theta}{r^2}. \qquad \text{Eq 2.14}$$

Equation 2.14 indicates that intensity of the emitted radiation is proportional to the square of the particle's charge and acceleration. The intensity is maximized at right angles to the direction of motion and cannot be emitted in the forward or backwards direction (θ = 0° or 180°). Equation 2.14 also demonstrates the relationship the charged particle's mass plays in bremsstrahlung production. Through classical physics, if the charged particle were to interact with the nucleus through Coulombic interactions, the acceleration of the charged particle is:

$$\vec{a}=\frac{zeZe}{4\pi\epsilon_0 m r^2}, \qquad \text{Eq 2.15}$$

where

ze is the charge of the charged particle,

Ze is the charge of the nucleus,

m is the mass of the charged particle.

Equations 2.14 and 2.15 show that the intensity of bremsstrahlung production is proportional to the acceleration squared and inversely proportional to the mass of the charged particle squared. Since the mass of a proton is approximately 1836 more massive than an electron, the resulting bremsstrahlung intensity due to protons will be approximately three million times less than achievable from electrons.

If the charged particle obtains relativistic velocities the electric field becomes tipped forward, altering the classical expression shown in equation 2.12 to give:

$$\vec{E}(r)=\frac{1}{4\pi\epsilon_0}\frac{q}{c^2}\frac{\vec{a}}{\vec{r}}\frac{\sin\theta}{\left(\sqrt{1-\beta\cos\theta}\right)^5}. \qquad \text{Eq 2.16}$$

Substituting this into the Poynting vector gives the following relativistic bremsstrahlung intensity:

$$\left|\vec{S}\right| = I(r,\theta) = \frac{1}{16\pi\epsilon_0}\frac{q^2a^2}{c^3r^2}\frac{\sin^2\theta}{(1-\beta\cos\theta)^5}. \qquad \text{Eq 2.17}$$

As β increases, bremsstrahlung production becomes more and more forward peaked, with no bremsstrahlung production in the forward or backward direction (θ = 0° or 180°). Using equation 2.17 the maximum or characteristic angle can be determined as a function of the charged particle's kinetic energy by setting $dI(r,\theta)/dr = 0$ to arrive at a value for θ_{max}

$$\theta_{max} = \arccos\left[\frac{1}{3\beta}\left(\sqrt{1+15\beta^2}-1\right)\right]. \qquad \text{Eq 2.18}$$

A plot of equation 2.18 is illustrated in figure 2.5. This shows the characteristic angle plotted against electron kinetic energy.

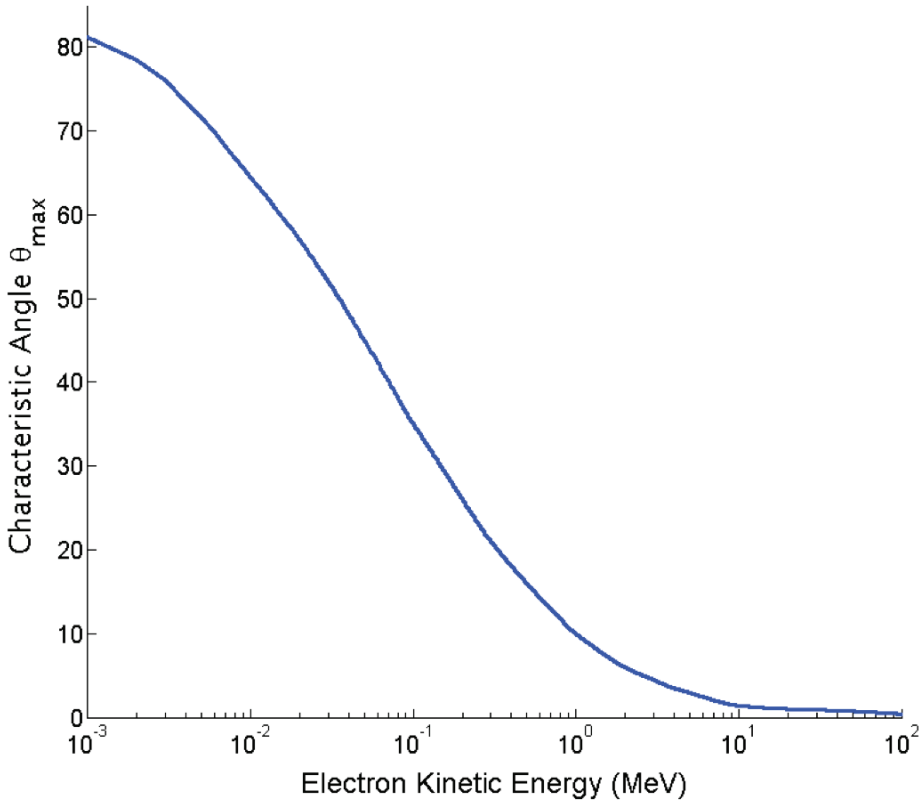

Figure 2.5 Bremsstrahlung characteristic angle (θ_{max}) plotted against electron kinetic energy[5].

2.3 Photon Interactions with Matter

Photon interactions with matter occur with either the nuclei or the orbital electrons of the absorbing medium. In the radiotherapy energy range, six dominant photon interactions exist. Table 2.1 shows these photon interactions and their associated energy range in tissue. Within this work, the highest energy used was 7 MeV, therefore photonuclear events had a small probability distribution or cross section for interaction and will not be discussed in this work.

Table 2.1 Photon interactions in the radiotherapy energy domain and their associated energy ranges in tissue[4,5,26].

Photon Interaction	Energy Range (MeV)
Thomson scatter	< 0.01
Photoelectric effect	0 to 0.2
Compton scatter	0.9 to 10
Rayleigh scatter	< 1
Pair production	< 5
Photonuclear scatter	> 10

The five remaining photon interactions can be separated into two subsets based on their energy transferred to matter. Thomson and Rayleigh scattering events are elastic in nature and only redirect the photon through small angles with very little or no energy loss. The remaining three prominent photon interactions are the most crucial as they can deposit up to all of the photon's energy during the event. The relative importance of the photoelectric effect, Compton effect and pair production depends on the atomic number, Z, of the absorbing medium and the interacting photon energy, hv. Figure 2.6 illustrates the relative predominance of each major interaction with photon energy for various absorbing mediums (Z = 1 to 100). The curves show where two interactions are equally probable[4,5]. For the purposes of this work the photoelectric effect is of most importance, due to the Z^3 dependence of the photoelectric mass attenuation coefficient. As a result, image quality is significantly improved compared to images taken with a 6 MV spectrum in which the Compton effect is dominant.

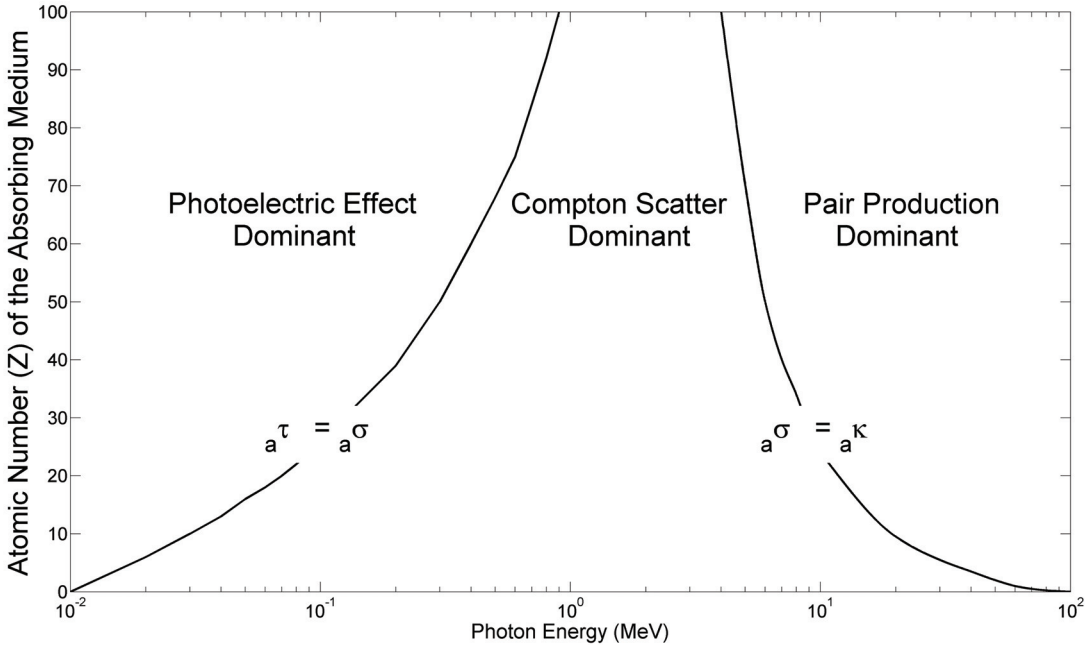

Figure 2.6 Relative atomic cross section for photoelectric effect ($_a\tau$), Compton effect ($_a\sigma$) and pair production ($_a\kappa$) as a function of photon energy and the atomic number of the absorbing medium[4,5].

2.3.1 Compton Scattering

Compton, or incoherent scattering, is the interaction of a photon of energy hν and a loosely bound orbital electron. The electron is assumed to be free and stationary at the time of the collision, i.e. the binding energy is negligible[4,5]. Figure 2.7 illustrates the Compton effect, in which a photon is scattered at an angle θ with energy hν', that is less than hν, and a Compton recoil electron is ejected from the atom at an angle φ with kinetic energy E_K.

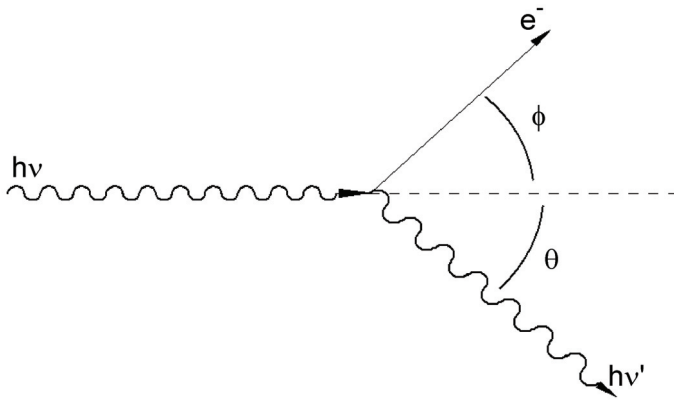

Figure 2.7 The Compton scatter with an incident photon with energy hν, scattered photon with energy hν′ and Compton recoil electron with kinetic energy E_K.[4,5].

The energy of the scattered photon is given as:

$$h\nu' = h\nu \frac{1}{1+\varepsilon(1-\cos\phi)}, \qquad \text{Eq 2.19}$$

where ε is the initial photon's energy normalized to the rest mass of an electron ($h\nu/m_ec^2$) and the energy of the scattered electron is given as:

$$E_K = h\nu \frac{\varepsilon(1-\cos\theta)}{1+\varepsilon(1-\cos\theta)}. \qquad \text{Eq 2.20}$$

The two angles share the following relationship defined as

$$\cot\phi = (1+\varepsilon)\tan\left(\frac{\theta}{2}\right). \qquad \text{Eq 2.21}$$

This shows that for higher photon energies the electron recoil angle, ϕ, becomes smaller. From equation 2.21, for photon scattering angles of π and π/2 the maximum scattered photon energy is 0.256 and 0.511 MeV, respectively, regardless of incident photon energy. For θ equal to zero there is no energy transferred to the electron, instead the electron is assumed to be free to oscillate under the electric vector created by the incident photon and a scattered photon emitted. This is known as Thomson scattering and is considered an elastic scattering event.

Joseph John Thomson determined that the interaction cross section per electron for a photon scattering angle of θ, per unit solid angle is given as:

$$_{e}\sigma_{Th} = \pi r_e^2 \int_0^{\pi} (1+\cos^2\theta) \sin\theta \, d\theta = \frac{8\pi r_e^2}{3} = 6.65 \text{ x } 10^{-25} \ \frac{cm^2}{electron}, \qquad \text{Eq 2.22}$$

where r_e is the classical electron radius. However, this failed to describe photon scattering higher than hν′ = 0.0096 MeV. As a result of this, in 1928, Klein and Nishina applied Dirac's relativistic theory of the electron to Compton scattering[4,5]. This resulted in the following Compton interaction cross section per electron:

$$_{e}\sigma = 2\pi r_e^2 \left[\frac{1+\varepsilon}{\varepsilon^2}\left(\frac{2(1+\varepsilon)}{1+2\varepsilon} - \frac{\ln(1+\varepsilon)}{\varepsilon}\right) + \frac{\ln(1+2\varepsilon)}{2\varepsilon} - \frac{1+3\varepsilon}{(1+2\varepsilon)^2}\right]. \qquad \text{Eq 2.23}$$

For incident photon energies of or below 0.001 MeV, equation 2.23 gives the following expression:

$$_{e}\sigma = \frac{8\pi r_e^2}{3}\left(1-2\varepsilon+\frac{26}{5}\varepsilon^2-\frac{133}{10}\varepsilon^3+\frac{1144}{35}\varepsilon^4-\cdots\right), \qquad \text{Eq 2.24}$$

and as ε approaches zero equation 2.24 yields the classical result derived by Thomson:

$$_{e}\sigma = \frac{8\pi r_e^2}{3}, \qquad \text{Eq 2.25}$$

Equation 2.23 shows that Compton electronic cross section is independent of atomic number, this is largely a result from the initial assumption that the electron is free and stationary[5].

Assuming that all elements, with the exception of hydrogen, have an atomic number to number of nucleons ratio of approximately one half, the Compton mass attenuation coefficient is given as:

$$\frac{\sigma}{\rho} = \frac{N_A}{A} \ {}_{a}\sigma = \frac{ZN_A}{A} \ {}_{e}\sigma \approx \frac{1}{2} N_A \ {}_{e}\sigma. \qquad \text{Eq 2.26}$$

where

ρ is the density of the absorbing medium,

N_A is Avogadro's number,

A is the number of nucleons,

Z is the atomic number.

This means that for most elements the Compton mass attenuation coefficient is independent of the atomic number.

2.3.2 Photoelectric Effect

The photoelectric effect is the most important interaction of low energy photons with matter and strongly depends on the atomic number of the medium. The photoelectric effect occurs when a photon with energy hv strikes a tightly bound orbital electron. As illustrated in figure 2.8, the incident photon is completely absorbed, transferring all of its energy to the electron. As a result, the electron is ejected from the atom with kinetic energy E_K equal to the photon's energy minus the binding energy E_b[4,5]. The photoelectric effect can only occur if the incident photon's energy is greater than that of the binding energy. Through conversation of momentum, the atom recoils with a negligible kinetic energy.

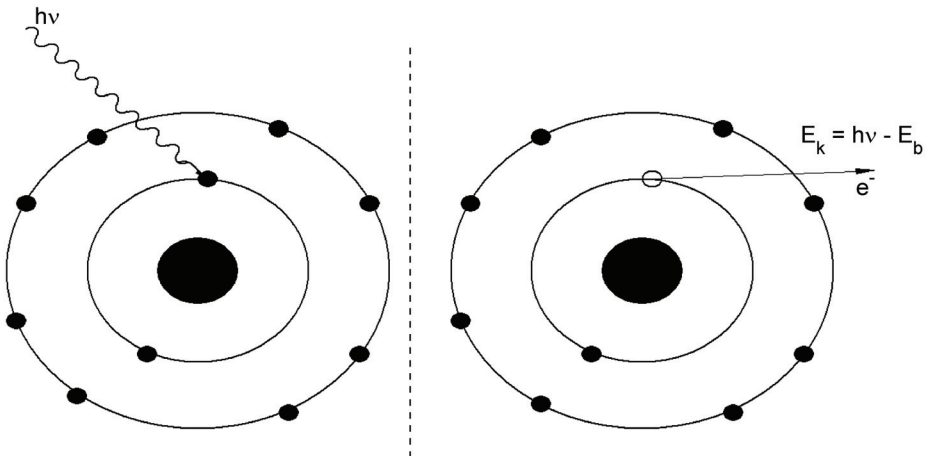

Figure 2.8 The photoelectric interaction of a photon with energy hν with an orbital electron with a binding energy of E_b. The electron is ejected from the atom with kinetic energy E_K[4,5].

In general, a theoretical derivation of the interaction cross section per atom is difficult and uncertain[4,5]. For k-shell electrons the interaction cross section per atom integrated over all angles of emission may be written as:

$$ {}_a\tau \cong \alpha^4 \, {}_e\sigma_{Th} Z^n \sqrt{\frac{32}{\varepsilon^7}}, \qquad \text{Eq 2.27} $$

where

α is the fine structure constant (1/137),

${}_e\sigma_{Th}$ is the total Thomson interaction cross section per atom (equation 2.22),

Z is the atomic number,

ε is the normalized photon energy ($h\nu/m_ec^2$),

n is a slowly varying constant that is a function of incident photon energy with a value of 4 at hν = 0.1 MeV, gradually rising to 4.6 at 3 MeV and gradually decreasing to 1 at 5 MeV[4,5].

In the diagnostic energy domain, the atomic interaction cross section is proportional to Z^4 and inversely proportional to $(h\nu)^3$. The photoelectric mass attenuation coefficient then becomes:

$$\frac{\tau}{\rho} = \frac{N_A}{A}\ {}_a\tau \approx \propto \left(\frac{Z}{h\nu}\right)^3. \qquad \text{Eq 2.28}$$

Unlike Compton scattering, the photoelectric effect mass attenuation coefficient is proportional to the cube of the atomic number in the diagnostic energy domain. As a result, images taken with x-rays with energy in the photoelectric energy domain have inherently better contrast due to variation in interaction cross sections between the various elements being imaged.

2.3.3 Pair Production

Pair production is an absorption process that can occur when the incident photon energy exceeds $2m_ec^2$, in which the photon is completely absorbed and an electron and positron pair are created. As illustrated in figure 2.9, pair production normally occurs within the Coulomb field surrounding the nucleus, however it can occur with a low probability in the Coulomb field of an atomic electron. This is called "triplet production", where the host electron acquires significant kinetic energy and is ejected from the atom, and has a threshold energy of $4m_ec^2$.

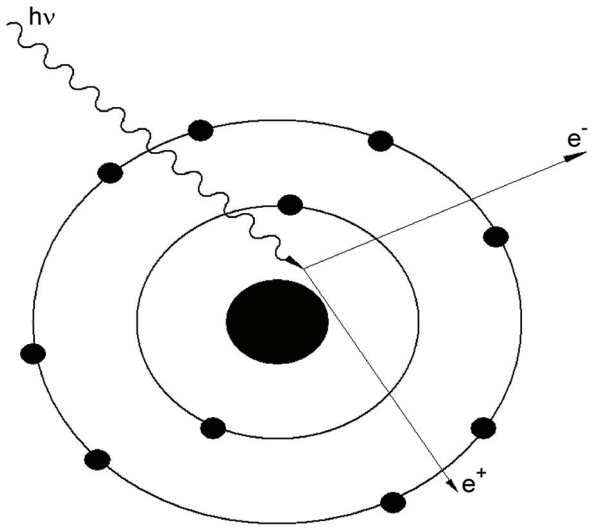

Figure 2.9 Pair production within the Coulomb field of the nucleus[4,5].

The mean kinetic energy of the electron and positron are given as:

$$\overline{E_K} = \frac{1}{2}\left(h\nu - 2m_e c^2\right). \qquad \text{Eq 2.29}$$

Like the photoelectric effect, a small negligible kinetic energy is given to the nucleus. Both the electron and positron do not necessarily receive equal kinetic energy, $\overline{E_K}$ is merely their average.

The mass attenuation coefficient for pair production is defined as:

$$\frac{\kappa}{\rho} = \frac{N_A}{A}\,{}_a\kappa \cong \frac{1}{2} N_A \alpha r_e^2 Z P(h\nu, Z), \qquad \text{Eq 2.30}$$

where P(hν,Z) is a function of photon energy and atomic number of the absorbing medium. This shows that atomic cross section is proportional to the square of the atomic number of the medium and the mass attenuation coefficient is linear with the atomic number of the medium.

In addition to the ionizing and radiative collisions that the positron will undergo an annihilation event in the medium, the positron will also annihilate upon losing all of

its kinetic energy. The positron will annihilate with a free and stationary electron, which results in two photons with equal energy of $m_e c^2$, and moving in approximately opposite directions. In 2% of annihilations, in-flight annihilation can occur with a tightly bound or free electron[4,5]. When the electron is tightly bound to the nucleus, the nucleus recoils with some kinetic energy resulting in only one photon. When in-flight annihilation occurs with a free electron, the two photons have two different energies.

2.3.4 Rayleigh Scattering

Rayleigh, or coherent scattering, is the process in which photons are elastically scattered by bound atomic electrons. The atom is neither excited nor ionized after the event. Rayleigh scattering is considered an elastic process since the photon loses essentially no energy and the atom recoils enough to conserve momentum. The photon is generally only scattered by a small angle. Rayleigh scattering occurs mostly at low photon energies hv and for high-Z media[4,5]. The atomic cross section for Rayleigh scattering is given by:

$$ {}_a\eta \widetilde{\propto} \frac{Z^2}{(h\nu)^2}. \qquad \text{Eq 2.31} $$

The mass attenuation coefficient for Rayleigh scattering is then given by:

$$ \frac{\eta}{\rho} \widetilde{\propto} \frac{Z}{(h\nu)^2}. \qquad \text{Eq 2.32} $$

Rayleigh scattering is fairly insignificant compared to the competing photoelectric and Compton interactions and only contributes a few percent or less to the narrow-beam mass attenuation coefficient.

2.3.5 Summary of Photon Interactions

The main characteristics of Rayleigh scattering, photoelectric effect, Compton scattering and pair production is shown in Table 2.2.

Table 2.2 Main characteristics of Rayleigh, photoelectric, Compton and pair production[4–6].

	Rayleigh Scattering	**Photoelectric Effect**	**Compton Scattering**	**Pair Production**
Photon Interaction	With bound electrons	With bound electrons	With free electrons	With nuclear Coulomb field
Mode Interaction	Photon scattered	Photon disappears	Photon scattered	Photon disappears
Energy Dependence	$\frac{1}{(h\nu)^2}$	$\frac{1}{(h\nu)^3}$	Decreases with energy $\sim(h\nu)^{-1}$	Increases with energy $\sim h\nu$
Threshold Energy	No	Shell binding energy	Shell binding energy	$2m_ec^2$ or $4m_ec^2$ (triplet production)
Atomic Coefficient Dependence on Z	${}_a\eta \propto Z^2$	${}_a\tau \propto Z^4$	${}_a\sigma \propto Z$	${}_a\kappa \propto Z^2$
Mass Coefficient Dependence on Z	$\frac{\eta}{\rho} \propto Z$	$\frac{\tau}{\rho} \propto Z^3$	Independent of Z	$\frac{\kappa}{\rho} \propto Z$
Particles Released	None	Photoelectron	Compton recoil electron	Electron-positron pair

For a given medium, the electronic cross section, atomic cross section and mass attenuation coefficient are the sum of the individual interactions that a photon may have with an atom:

$${}_e\mu = {}_e\eta + {}_e\tau + {}_e\sigma + {}_e\kappa, \qquad \text{Eq 2.33}$$

$${}_a\mu = {}_a\eta + {}_a\tau + {}_a\sigma + {}_a\kappa, \qquad \text{Eq 2.34}$$

$$\frac{\mu}{\rho} = \frac{\eta}{\rho} + \frac{\tau}{\rho} + \frac{\sigma}{\rho} + \frac{\kappa}{\rho}. \qquad \text{Eq 2.35}$$

An example of this summation is shown in figure 2.10, in which the mass attenuation coefficient for water is plotted as a function of energy for Rayleigh scattering, photoelectric effect, Compton scattering and pair production.

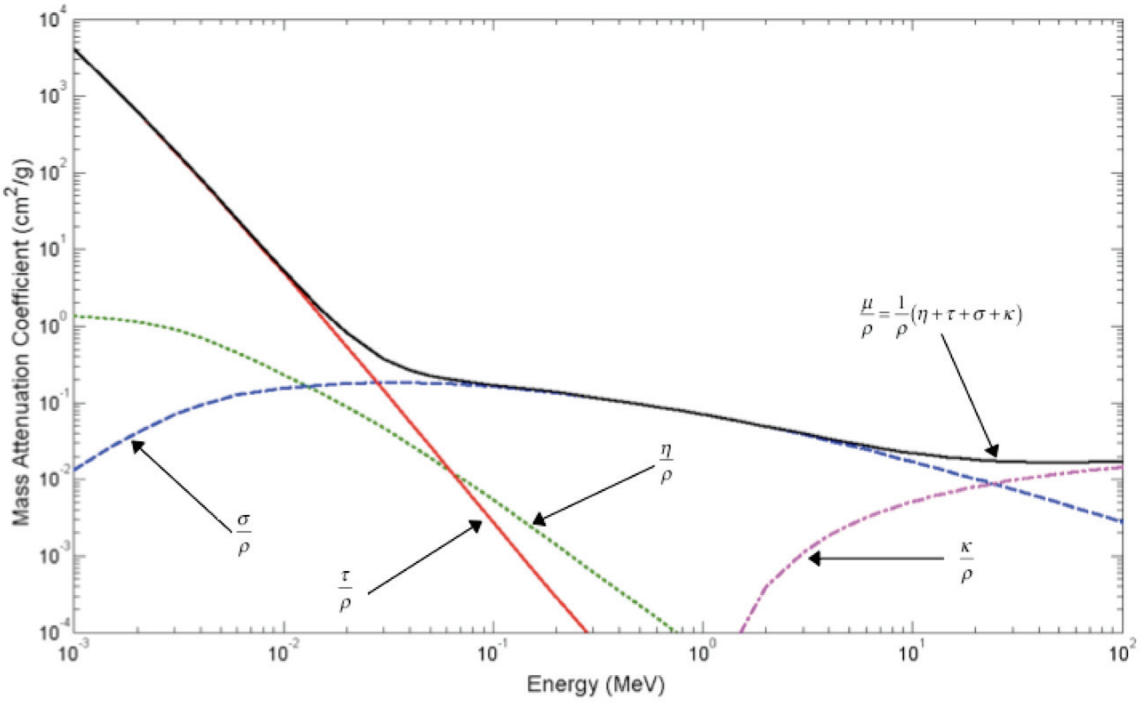

Figure 2.10 Mass attenuation coefficient μ/ρ plotted against photon energy hν in the energy range of 1 keV to 100 MeV for water. Also shown are the individual coefficients for Rayleigh scattering (η/ρ), photoelectric effect (τ/ρ), Compton scattering (σ/ρ) and pair production including triplet production (κ/ρ). Data was obtained from the National Institute of Standards and Technology (NIST), Washington, DC[27].

When the mass attenuation coefficient is multiplied by density the linear attenuation coefficient μ is determined. This value is useful in describing attenuation of the photon beam through a medium. As illustrated in figure 2.11, if a monoenergetic parallel photon beam consisting of a large number of photons N_o was incident on a flat plate of material of thickness x perpendicular to the photon beam, then the number of photons dN at a thickness of dx would have the following relationship:

$$\frac{dN}{N} = -\mu dx. \qquad \text{Eq 2.36}$$

Integrating over the depth x from 0 to x and the corresponding photon populations from N_o to N(x), gives:

$$\int_{N_o}^{N(x)} \frac{dN}{N} = -\mu \int_0^x dx, \qquad \text{Eq 2.37}$$

$$\ln \frac{N(x)}{N_o} = -\mu x, \qquad \text{Eq 2.38}$$

$$N(x) = N_o e^{-\mu x}. \qquad \text{Eq 2.39}$$

This shows the standard exponential relationship for monoenergetic photon beams. This model is an ideal case and assumes simple absorption with scattering or secondary radiation. In the broad beam geometry, scattered radiation can increase the detected signal.

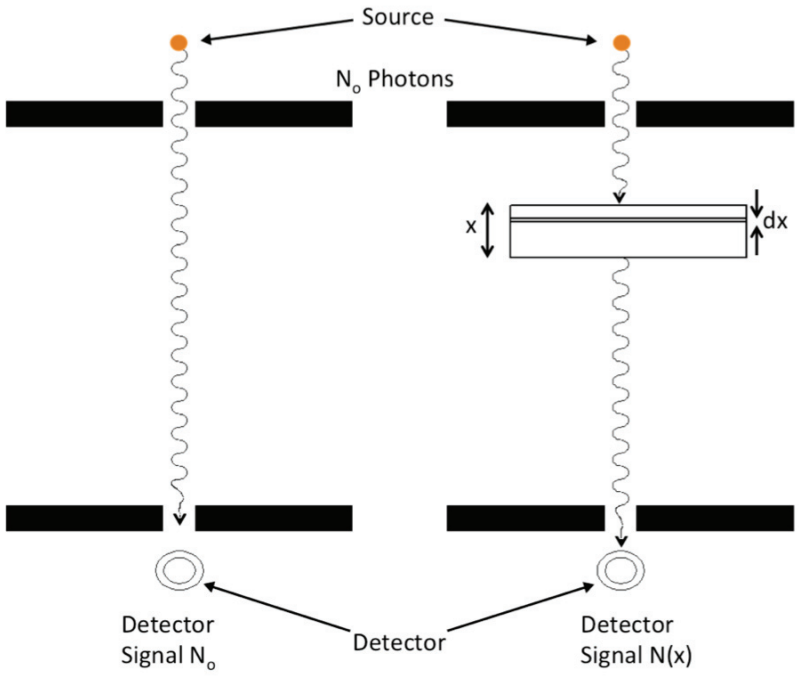

Figure 2.11 Measurement of exponential photon attenuation in a narrow beam geometry[4,5].

CHAPTER 3 BEAM GENERATION IN A LINEAR ACCELERATOR

This chapter addresses modern clinical linear accelerators, with a focus on their various components and functions.

In modern radiation therapy, electrons are most commonly accelerated to the necessary velocity through a linear accelerator, or linac. Linacs are isocentrically-mounted machines that allow electrons to be accelerated to kinetic energies ranging from 4 MeV to 25 MeV[5]. In a modern linac, electrons are produced in an electron gun. In Varian linacs, the electron gun is a triode design, which is composed of a heated cathode, a grid and a perforated grounded anode. The triode gun, shown in figure 3.1, has two adjustable parameters utilized in this work: (i) the gun High Voltage (HV) and the grid voltage. The gun HV and grid voltage have adjustable voltages ranging from -3kV to -30 kV and -80 V to 300 V, respectively. For the 6 MV therapeutic beam in a Varian linac, the HV and grid voltage are approximately -15 kV and 110 V, respectively. Within the cathode, usually composed of porous tungsten and barium, electrons are thermionically emitted and focused into a pencil beam approximately 3 mm in diameter that is accelerated through the anode, at which point the electrons drift into the accelerating waveguide. The grid functions to vary the beam current and is used to turn on or hold off the beam.

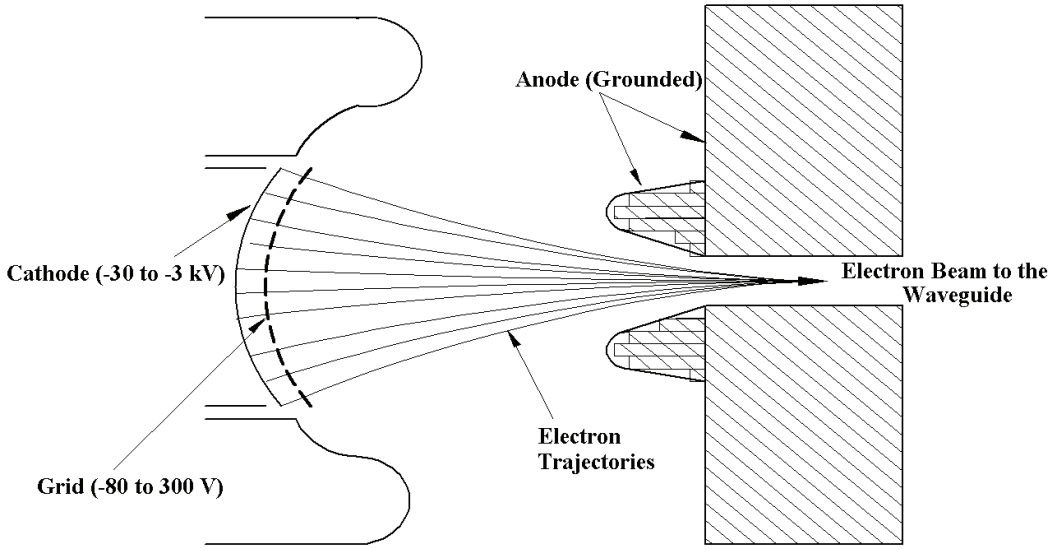

Figure 3.1 A triode electron gun showing the cathode, grid, anode and their associated voltage ranges as well as electron trajectories within the gun[28].

The radiofrequency (RF) power used in the accelerating waveguide is generated in a klystron operating in the S-band (2856 MHz). These RF waves are transferred to the accelerating waveguide through an evacuated waveguide. Within the accelerating waveguide, the transfer of RF power field accelerates electrons, thereby gaining kinetic energy.

Focusing coils encompass the accelerating waveguide to form a solenoid that produces a magnetic field parallel to the waveguide axis. The solenoid is used to limit the expansion of the electron beam diameter within the waveguide. Surrounding the accelerating waveguide at both ends are two steering coils, which form an orthogonal dipole magnet to permit horizontal and vertical deflections of the electron beam. At the entrance of the waveguide, these are used to correct for errors in the angle of injection of the beam from the electron gun. At the exit of the waveguide, these are used to

correct for any error in the angle between the waveguide axis and the entrance to the bending magnet.

As a result of the length of high-energy linacs (approximately 150 cm at 25 MeV for a standing wave waveguide), the accelerating waveguide is positioned orthogonal to the linac head. To steer the electron beam from the accelerating waveguide to the linac head, three achromatic magnets are used to form the bending magnet, which rotates the electron beam through 270°. For the beams generated here, the bending magnet current was adjusted to allow the selection of electron energy exiting the bending magnet.

The electron beam strikes a thick target (110% of R_{CSDA}) within the linac head, to produce bremsstrahlung and characteristic x-rays, which generate the polyenergetic photon beam. As a result of bremsstrahlung production at these electron kinetic energies being largely forward directed (Fig 2.5), the photon beam is attenuated by the flattening filter to produce an uniform intensity photon beam that has a flat profile within the central 80% region at a depth of 10 cm in water at a source-to-surface distance (SSD) of 100 cm for the largest field size possible, typically 40x40 cm^2.

The delivered dose is monitored using two transmission ionization chambers, called monitor chambers, permanently placed within the central axis of the linac head. The monitor chambers provide a dose and dose rate measurement by relating the time integrated signal (units of monitor unit or MU) such that 1 MU is equal to 1 cGy delivered in a water phantom at a pre-defined depth, for example at a depth of 5 cm, and SSD of 95 cm, with a 10 x 10 cm^2 field. The monitor chambers also monitor the

flatness and symmetry of the beam and if necessary can provide information to actively steer the electron beam through a feedback loop to provide the correct flatness and symmetry. Two monitor chambers are used for safety, with one as a primary and the other as a secondary backup. If the primary chamber fails, the secondary will terminate the beam once the prescribed number of MUs has elapsed.

A conical aperture filled with vacuum and collimated by tungsten forms the primary collimation. The primary collimator forms a circle at isocenter with a radius of 20 cm, which defines the maximum possible radiation field. Secondary and tertiary collimation devices define the shape of the irradiated field. Two sets of independent tungsten blocks, called jaws, compose the secondary collimation. The jaws define square and rectangular fields with a maximum dimension of 40 x 40 cm^2. The jaws move in an arc such that their edges are parallel to the beam at all angles. The thicknesses of the jaws are designed such that no more than 2% of the primary beam is transmitted through them. The multileaf collimator (MLC) is the tertiary collimation system. An MLC is typically composed of 120 computer-controlled tungsten leaves that form highly irregular fields.

Clinical electron beams are also possible with most linacs. To use therapeutic electron beams, the x-ray target arm is retracted, allowing the electron pencil beam to travel through the vacuum, beryllium exit window and air. The flattening filter is replaced with an electron scattering foil, which scatters the electron beam to cover large clinical field sizes. Due to the high electron scatter on other components of the linac head and in air, a unacceptablably high penumbra is created. As a result the MLC

leaves are retracted, the jaws opened to a slightly larger than intended field size and an applicator is added to the linac head to collimate the electron beam. On a Varian linac, the applicator extends 95 cm from the source and is capable of holding Cerrobend cut outs that shape the electron beam into irregular fields.

CHAPTER 4 X-RAY DETECTION AND MEASUREMENT

In this chapter, devices and instrutments used for the detection of radiation are discussed, including: thermoluminescent dosimeters, ionization chambers, semiconductor dosimeters and electronic portal imaging devices.

4.1 THERMOLUMINESCENCE DOSIMETRY

Certain materials can retain some of the absorbed energy when irradiated. This energy is then released as photons with energy in the ultraviolet, visible or infrared energy domain. This is known as luminescence. Two types of luminescence are known, fluorescence and phosphorescence. Fluorescence and phosphorescence occur through the same mechanisms and only vary in the time delay between stimulation and the emission of a photon. Fluorescence occurs with a time delay ranging from 0.1 to 10 ps and phosphorescence occurs with a time delay greater than 10 ps[29]. These materials are stimulated using either light or heat. In the case of thermoluminescence, heat is used to stimulate the material. A thermoluminescent material or dosimeter (TLD) is a dielectric material that has imperfections in the crystal lattice. These imperfections provide centers that serve as either traps or luminescence centers[4,29]. When irradiated with a photon beam, secondary electrons are produced through the interactions discussed in section 2.3. The secondary electrons are largely responsible for any absorbed energy; these electrons then produce many free electron-hole pairs. In a TLD, traps serve to capture free electrons or holes in an electrical potential well. An electron or hole can be stored in a trap for hours to months depending of the composition of the crystal. Fading, or trap leakage, can occur when traps are unable to hold their electrons

or holes under ambient temperatures[4,29]. When heated, electrons or holes have sufficient energy to be promoted to the conduction band and can migrate to a luminescence center, at which point the recombination of the electron and hole result in the emission of a light photon. Traps and luminescence centers can be naturally occurring or introduced to the crystal through vacancies or impurities. Common tissue equivalent TLDs used clinically are TLD-100 (LiF:Mg,Ti, Z_{eff} = 8.2) and TLD-800 ($Li_2B_4O_7$:Mn, Z_{eff} = 7.4)[4].

The measurement of thermolunminescence light emitted from a TLD is done with a TLD reader. A TLD reader is composed of a heater pan, a thermocouple, and a photomultiplier tube. The TLD is typically heated using N_2 gas or by an intense light spot. The resulting thermoluminescent light is detected using the photomultiplier tube[4,29]. The resulting light output plotted against temperature is known as a glow curve. For $Li_2B_4O_7$:Mn, the dosimetric region of the glow curve is between 140°C and 220°C with a maximum (glow peak) at 180°C[4]. At temperatures above the dosimetric range, blackbody radiation and spurious thermolunminescence emission produce non-dose related light[4]. At temperatures below the dosimetric range, the temperature does not provide enough energy for the electrons or holes to be promoted to the conduction band. The dose is determined by correlating the total light output in the dosimetric region to a calibration dose. A dose accuracy of 1.5% to 2% and precision of 1% to 4% with TLDs can be achieved if the following conditions are met: the heating cycle is reproducible within the linear region of dose, has constant response with photon energy and the TLD is read before fading has become appreciable (approximately 10% within

the first month for TLD-800s and less than 5% for the first three months for TLD-100s)[4,30].

4.2 Ionization Chamber Dosimetry

An ionization, or ion chamber, is one of the most simple and popular dosimeters used in radiation therapy. An ion chamber is composed of four main components: an inner central electrode, outer wall electrode and an air filled chamber. When in use the ion chamber is connected to a separate device called an electrometer. As discussed in section 2.3, when photons interact with matter secondary electrons are produced through photoelectric, Compton and pair production events. These secondary electrons can be produced outside the wall, in the wall or within the gas itself, however the chamber wall is generally thin (less than 1 mm) and composed of a low-Z material, so as to not attenuate the electrons or photons[4,29]. As discussed in section 2.1, as the secondary electrons transverse matter they can ionize the atoms or molecules in the gas. A potential difference is applied to the electrodes, which causes the negative and positive ions to be attracted to the anode and cathode, respectively. The electrometer measures the amount of charge collected and supplies the potential difference across the electrodes.

The dose to the gas, $D_{g,}$ is then given as:

$$D_{gas} = \frac{Q}{m}\left(\frac{\bar{W}}{e}\right)_{gas}, \qquad \text{Eq 4.1}$$

where

Q is the measured charge,

m is the mass of the gas,

$\left(\frac{\bar{W}}{e}\right)_{\text{gas}}$ is the energy lost in gas per coulomb of charge released (33.97 J/C in air).

Equation 4.1 only provides limited information about the dose to the gas and does not provide any information about the dose to the medium. To calculate the dose to the medium, Bragg-Gray cavity theory is applied[4]:

$$D_{med} = D_{gas} \cdot {}_{m}\bar{S}^{med}_{gas}\rho, \qquad \text{Eq 4.2}$$

where

D_{med} is the dose to the medium,

${}_{m}\bar{S}^{med}_{gas}$ is the ratio of the average mass collisional stopping power of medium to gas for electrons,

ρ is the perturbation correction factor accounting for all the possible perturbations to the absorbed dose to the medium caused by the ion chamber inserted at the point of measurement.

However, the use of equation 4.2 can be difficult to calculate dose to the medium for a polyenergetic beam. Equation 4.2 also neglects the creation of delta rays from hard collisions within the cavity[29]. The simplest means to determine the dose to the medium is to use the TG-51 protocol. TG-51 involves using an absorbed dose to water calibration factor, $N_{D,w}^{^{60}Co}$, a quality conversion factor, k_Q, and corrections to account for temperature, pressure, humidity, polarity effects, ion chamber collection inefficiency and the electrometer reading in true Coulombs. The ion chamber and electrometer must be sent to a standards lab to determine $N_{D,w}^{^{60}Co}$ and the electrometer reading in true

Coulombs. k_Q acts to convert the calibration factor for ^{60}Co beam to an arbitrary beam quality. k_Q is a function of beam quality and is ion chamber dependent. However, the TG-51 formalism cannot be strictly followed for a low-Z target beam as k_Q is not known. Instead, an absolute dosimetry, such as a TLD, can be used to cross-calibrate the ion chamber. If this is done correctly, a conversion from the charge collected to the dose at a certain temperature and pressure can be determined. Accounting for temperature and pressure, the dose to the medium is:

$$D_{med} = Q \cdot k \left(\frac{T}{T_m}\right)\left(\frac{P_m}{P}\right), \quad \text{Eq 4.3}$$

where

k is the cross-calibration factor in cGy per pC,

T_m is the temperature at the time of calibration in Kelvin,

P_m is pressure at the time of calibration in kPa,

T is the measured temperature,

P is the measured pressure.

4.2.1 Percent Depth Dose

Percent depth dose (PDD) curves are used to characterize the beam quality of generated photon and electron beams. PDD curves measure the central axis dose distribution inside a phantom, usually water, and are normalized to maximum dose, D_{max}, at the depth of maximum dose, z_{max}. Therefore the PDD value for a give depth, field size, source-to-surface distance (SSD) and photon beam energy is defined as:

$$PDD(z,A,f,h\nu) = 100 \times \frac{D(z)}{D_{max}(z_{max})}, \quad \text{Eq 4.4}$$

where

D is the dose at depth z,

A is the field size defined at the surface,

f is the SSD,

hv is the photon beam energy.

The geometry for measuring PDD distribution is illustrated in figure 4.1.

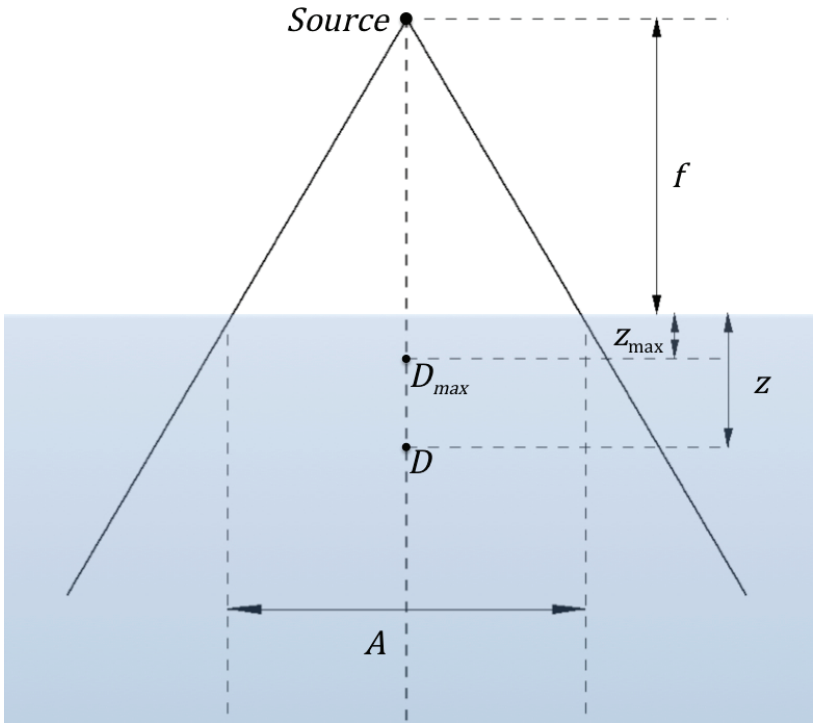

Figure 4.1 Geometry for measurement of PDD distributions. D is the measured dose at a depth z normalized to the maximum measured dose D_{max} at depth z_{max}, for a given field size A and source-to-source distance f.

PDD curves are useful as they allow comparison of various energy photon or electron beams. Megavoltage photon PDD curves are generally described in terms of several points or regions: the surface dose, $D_{surface}$, the build-up region and the exit dose, D_{exit}. Megavoltage electron beams are typically described in terms of the maximum range, R_{max}, the practical range, R_p, and the depth of the 90% and 50% PDD,

R_{90} and R_{50}, respectively. The practical range is the depth at which the tangent line plotted through the steepest section of the PDD (typically R_{50}) intersects with the extrapolation line of the bremsstrahlung background. The maximum range is the depth at which the extrapolation of the PDD tail meets the bremsstrahlung background. R_{max} is the largest penetration depth of electrons in the medium. Examples of these terms can be seen in figure 4.2, which shows PDDs of Monte Carlo simulated clinical 6 MV photon and 4 MeV electron beams. For the photon beam, the buildup region is the range of depths between the surface and z_{max} in which charge particle equilibrium is reached. The fall-off region is the region between z_{max} and the exit of the phantom and is exponential in nature. For the purposes of the work presented here, photon and electron PDDs were collected using an ionization chamber and p-type electron field diode, respectively.

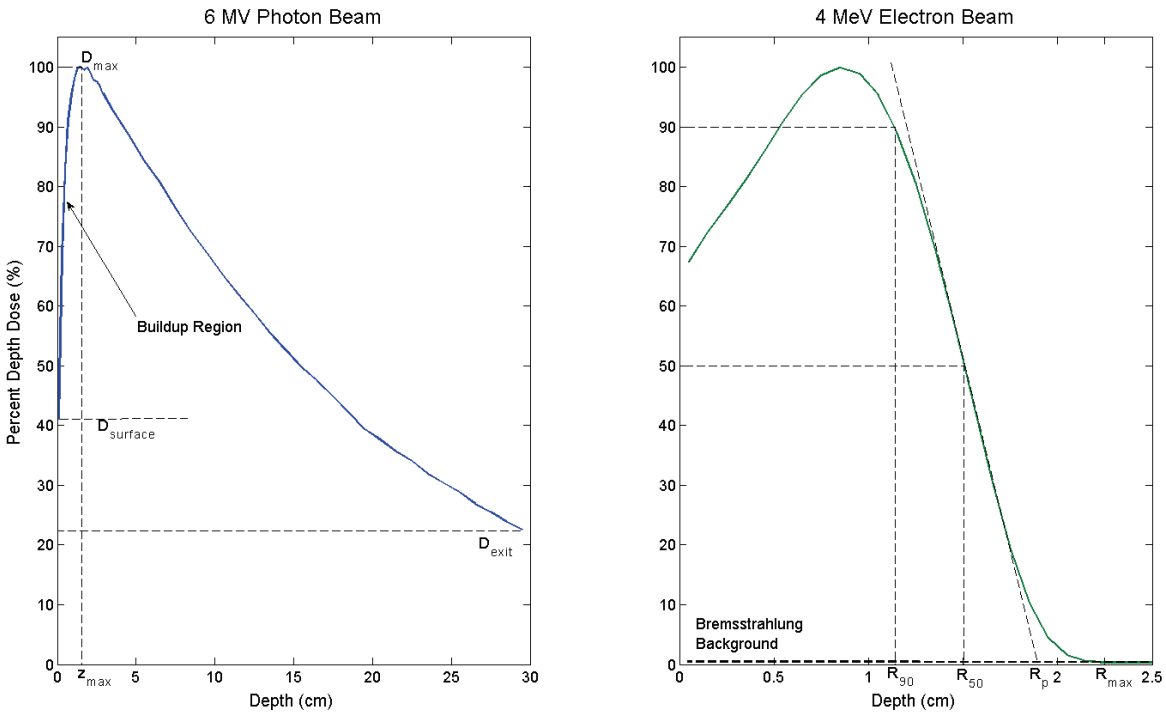

Figure 4.2 Monte Carlo simulated PDD curves of a clinical 6 MV photon beam and 4 MeV electron beam. Illustrated on the 6 MV plot are the surface dose, $D_{surface}$, the maximum dose, D_{max} and corresponding depth z_{max}, the exit dose, D_{exit}, and the buildup region. Illustrated on the 4 MeV plot is the practical range, R_p, the maximum range, R_{max}, and the 90% and 50% dose depths, R_{90} and R_{50}, respectively.

4.3 SEMICONDUCTOR DOSIMETRY

Silicon diodes are strictly relative dosimeters and should not be used as an absolute dosimeter; this is largely due to the variation in their sensitivity with radiation damage[4,29]. Silicon diode dosimeters are an unbiased p-n junction diodes. Diodes used in radiation therapy are made by taking a p-type silicon and doping the surface with an n-type silicon. This is referred to as a p-Si dosimeter. A p-Si dosimeter is preferred for dosimetry as it is less susceptible to radiation damage and has a smaller dark current than an n-Si dosimeter[4,29].

The diode dosimeter works in a similar manner as a TLD, in that as primary or secondary electrons traverse the diode, electron-hole pairs are created throughout the diode. The charges created within the n-type silicon diffuse into the depletion region and are attracted under the intrinsic electric potential to the p-type silicon. This creates a current in the reverse direction of the diode[4,29].

Silicon diodes are preferred for electron and low energy photon measurements due to the lower backscatter compared to germanium diodes. The small size of the diode is also advantageous in certain situations such as: for small field measurements in stereotactic radiosurgery, in the photon beam penumbra region or for low energy electron beam percent depth dose measurements. For higher energy photon measurements, an attenuating layer is placed below the diode to absorb any backscattered photons which can cause spurious results.

4.4 Electronic Portal Imaging Devices

In the past, patient verification images for alignment relative to isocenter involved using film emulsion coupled to a scintillating phosphor and high-Z screen, called a film cassette. A digital system called an electronic portal imaging device (EPID) is used in modern radiation therapy. As shown in figure 4.1, megavoltage EPIDs are generally composed of three main components: a high-Z build-up plate, a scintillating phosphor and a photodiode array.

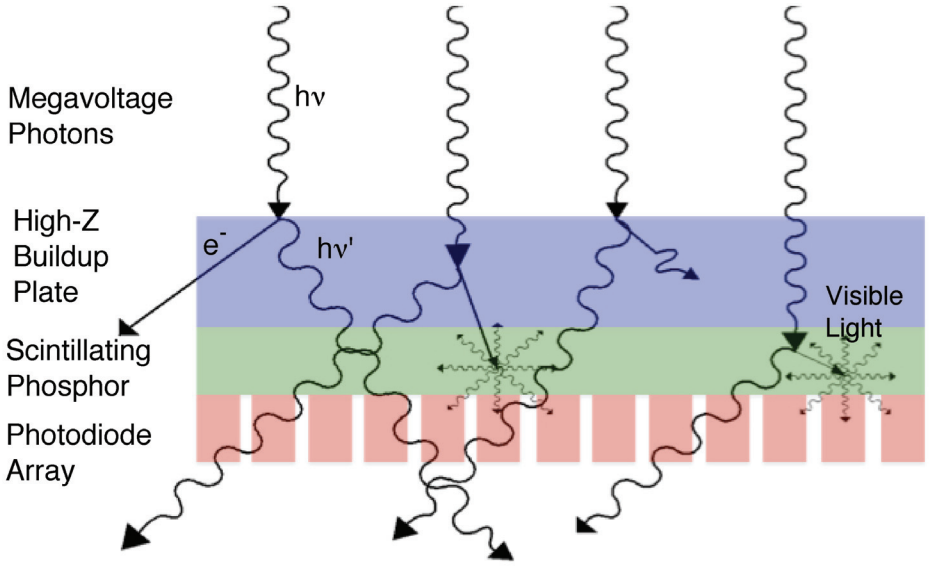

Figure 4.3 A typical amorphous silicon (a-Si) EPID composed of a high-Z buildup plate, scintillating phosphor and a photodiode array. Also shown are megavoltage photons incident on the EPID, producing scattered photons and secondary electrons through Compton events. The secondary electrons are interacting with the phosphor to produce visible light, which can be detected by the photodiodes.

EPIDs are similar to film cassettes in that it is an indirect detection system. Indirect means that photons in the megavoltage energy range are detected by interacting with a high-Z build-up plate to produce Compton recoil electrons, which then interact with the scintillating phosphor to produce visible light that can be detected by the array of photodiodes. A relatively thick high-Z material is used for the build-up plate to increase the efficiency of the EPID. This is accomplished by increasing the cross-section for Compton and photoelectric events, while maintaining a thickness that does not attenuate the secondary electrons produced and removes low energy scattered photons from the object being imaged. Within the scintillating phosphor, the secondary electrons interact with orbital electrons to promote them to a higher energy level, resulting in an unstable state. In re-establishing equilibrium, the orbital electrons

transition back to their lower energy level and visible light photons are emitted. A common phosphor used is gadolinium oxysulfide doped with terbium (Gb_2O_2S:Tb). Gb_2O_2S:Tb has a relatively high index of refraction, as a result over 60% of the produced visible light is internally reflected at the surfaces of the phosphor[31,32]. The thickness of the phosphor layer is optimized in terms of image spatial resolution and detection efficiency. Spatial resolution is degraded as the thickness of the phosphor is increased and the efficiency is increased as thickness increases. Visible light photons are subsequently detected by the photodiodes.

Each pixel within the EPID is a discrete amorphous silicon photodiode arranged in a two dimensional grid. The photodiodes are coupled to a thin-film transistor array. Each pixel within the array incorporates a thin-film switch connected to a capacitive device. The switch of every pixel in a row is connected to a single conductive line. During irradiation, the switches are non-conductive, this causes the charge to be integrated in the capacitive device of each pixel. During readout, the switches are made conductive and the integrated charge within each capacitor is readout row by row. External electronics form data lines down each column of the array. The data lines function to complete the Cartesian coordinates during readout. Upon the completion of readout, each pixel is reinitialized and the switches made non-conductive[33].

For the research reported here, a Varian aS1000/IAS3 system was used. The aS1000/IAS3 imaging system uses an IDU20 EPID. The IDU20 consists of a 1 mm copper plate, a Gb_2O_2S:Tb phosphor approximately 0.13 g/cm^2 thick and a 1024x768 array of photodiodes switched by thin-film transistors deposited on a glass substrate.

CHAPTER 5 MONTE CARLO SIMULATIONS

In this chapter, the Monte Carlo method is discussed, starting with a brief history and introduction, followed by a description of the EGSnrc Monte Carlo code used in this work and ending with an introduction to the variance reduction techniques used.

5.1 Introduction

Monte Carlo simulations use random number sampling of known probability distributions to determine a result. The Monte Carlo method is most useful when investigating a stochastic event, in which the outcome of any one event is unknown, but the probability distribution is known. An example of this is determining the depth a photon travels in water before interacting.

Comte de Buffon's needle problem is one of the earliest forms of Monte Carlo. The needle problem estimates π by tossing n needles of length L on a set of parallel lines spaced a distance d apart and counting the number of needles, t, that touch the parallel lines (Fig 5.1). The probability, p, that a needle touches a line is

$$p = \frac{t}{n} = \frac{2L}{\pi d}. \qquad \text{Eq 5.1}$$

By rearranging equation 5.1, π can be estimated with the accuracy increasing as n increases.

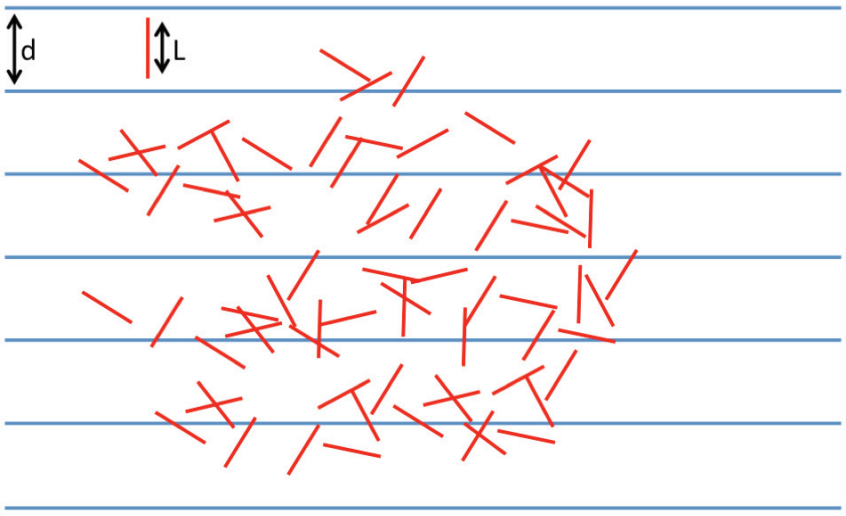

Figure 5.1 An illustration of Comte de Buffon's needle problem.

Modern Monte Carlo started at the Los Alamos Scientific Laboratory by Stanisław Ulam and John von Neumann to study neutron diffusion in matter. In his 1963 book, *Monte Carlo Calculation of the Penetration and Diffusion of Fast Charged Particles*, Martin J. Berger outlined the condensed history technique (CHT) which is the basis for most modern photon and electron transport Monte Carlo codes[34,35]. In the energies used in radiation therapy, a secondary electron undergoes approximately 10^6 elastic and inelastic collisions until it is locally absorbed. The tracking of electrons in a simulation accounts for the majority of the simulation time. CHT exploits the fact that most electron interactions result in extremely small changes in angle and direction and can therefore be grouped into a single "step" that represents the aggregate effect of many interactions. CHT allows for simulation of charged particles in a reasonable and accurate fashion, yet to further increase the efficiency of a Monte Carlo simulation, variance reduction techniques must be used. For the research reported here, the EGSnrc[36,37] Monte Carlo code was used. BEAMnrc[38] and DOSYXZnrc[37] user codes were used to

model radiation transport through the linacs and dose distributions in phantoms, respectively.

5.2 EGSnrc

Electron Gamma Shower, or EGS, is the electron-photon Monte Carlo transport code used throughout this project. EGS code was conceived from the pioneering work by Richard Ford and Ralph Nelson at the Stanford Linear Accelerator Center (SLAC)[34,35]. The first readily available version of EGS was the third generation, or EGS3. Upon the release of EGS3 in 1978, the code system quickly became the industry standard for designing detectors in high-energy physics[35]. This was partly a result of being freely distributed from SLAC, something that continues today at the National Research Council of Canada (NRC)[34]. EGS3 was capable of transporting photons with energy of 1 keV to 100 GeV and charged particles with energy from 1.5 MeV (total energy) to 100 GeV, through any element (Z = 1 to 100), compound or mixture. Due to the relatively high lower energy limits the EGS3 code was extended to have kinetic energy cut-offs of 10 keV charged particles[35]. This version was called EGS4 and was released in 1985. The work by David Rogers resulted in many of the changes to EGS3[35]. His work made it possible to allow the user to control code parameters around the electron step-size. Since this time, the NRC has undertaken a major re-work of the EGS4 system, resulting in the EGSnrc code. Many of these changes include a variety of enhancements in the CHT implementation and in some of the underlying cross sections[36].

The EGSnrc code can be described as several separate components: the PEGS4 media data file, the EGS code, HOWFAR and HOWNEAR, AUSGAB and user codes. The PEGS4 file contains information regarding the physical properties and interaction cross section of materials. The EGS code contains the subroutines used to simulate the transport of photons and light charged particles. HOWFAR and HOWNEAR specify information about the geometry and handle the transport of radiation between different materials. AUSGAB scores the results of the simulation and controls variance reduction techniques. User codes are user written codes that allow the user to run and gather the results of the simulation; examples of user codes include BEAMnrc, DOSXYZnrc, FLURZnrc, CAVRZnrc and SPRRZnrc.

For the purposes of this work, BEAMnrc and DOSXYZnrc were used. BEAMnrc code simulates radiotherapy beams generated in medical linacs and x-ray tubes. Rogers *et al*[38]. first released BEAM in 1995. BEAMnrc allows the user to design a linac through a series of individual component modules (CM), each of which operates independently from each other CM, and is contained between two planes that are perpendicular to and centered on the vertical z-axis[38]. This is shown visually in figure 5.2. To design a linac, the user first selects the CMs to be used. The CMs used in this work are SLABS, FLATFILT, JAWS, MIRROR and PYRAMIDS. The linac is then compiled. At this point, the user can input parameters for each CM that define the position, composition and geometry. Additionally, the user must define parameters such as the initial electron distribution, run time, the number of histories and the location of the scoring plane(s)[38].

The end result of a BEAMnrc simulation is a phase space file which contains data relating to particle energy, position, direction, charge, weight and place of last interaction for every particle crossing the scoring plane[38]. Prior to the start of the simulation, the user must define the location of the phase space and must be placed at the exit side of a CM. A phase space can be used as an input file for additional BEAMnrc or DOSXYZnrc simulations. The phase space can also be analyzed using a program called BEAMdp[39].

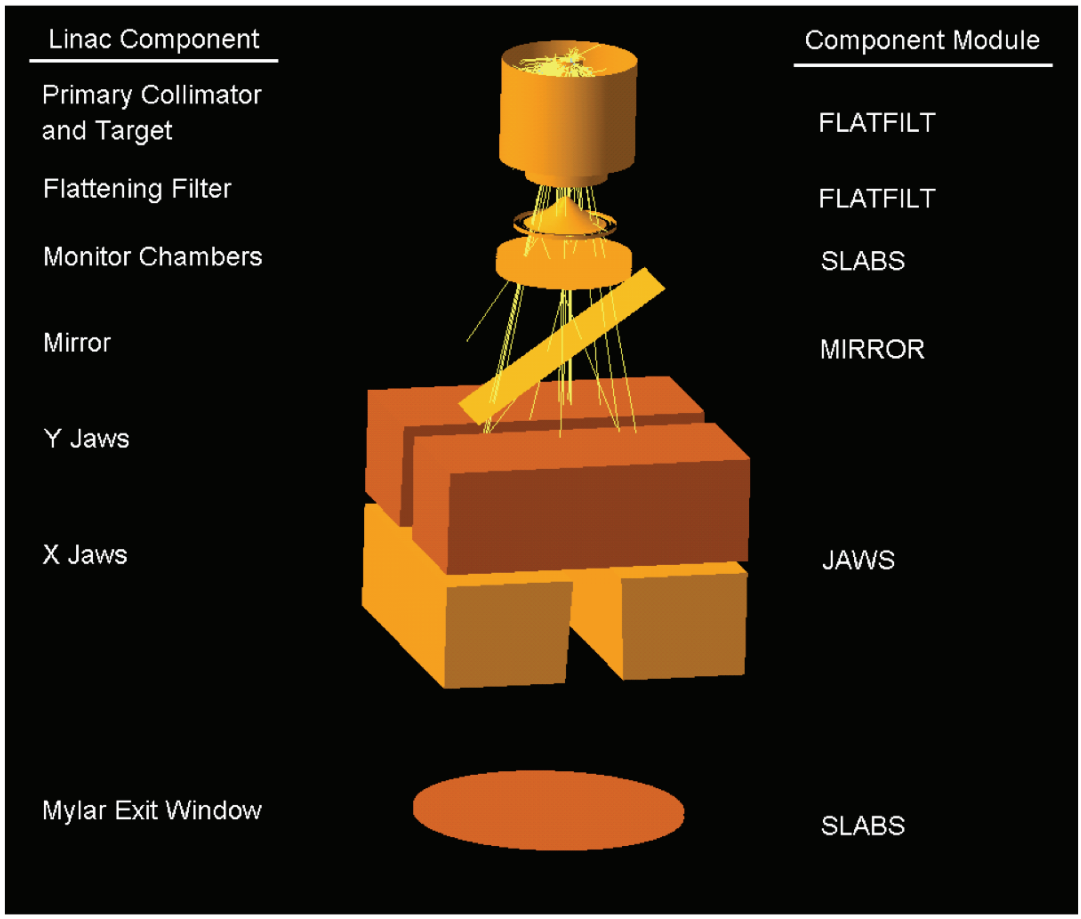

Figure 5.2 BEAMnrc simulation of a 6 MV Varian linac with electrons incident on a tungsten and copper target with bremsstrahlung photons (yellow). Shown (from the top down) is the primary collimator and target (FLATFILT), flattening filter (FLATFILT), monitor chamber (SLABS), mirror (MIRROR), Y and X jaws (JAWS) and mylar exit window (SLABS).

DOSXYZnrc[37] simulates photon and light charged particle transport through a medium and scores the energy deposited per primary particle. The user can use mono-energetic beams, predefined spectra or a phase space as sources. The medium can be either a user defined volume or a CT data set.

BEAMdp[39], or BEAM data processor, allows the user to analyze the phase space to derive characteristics such as fluence versus position, spectral distributions, energy

fluence, mean energy distributions and can also allow the user to combine two phase space files together.

5.3 VARIANCE REDUCTION TECHNIQUES

The efficiency of a Monte Carlo simulation is inversely proportional to the statistical variance and the time required to obtain this variance[40]. As a result, in order to reduce the time and maintain the same statistical variance, the efficiency of the simulation must increase. As stated earlier, CHT greatly improves the efficiency of simulation, however, it is generally not considered an approximate efficiency improving technique (AEIT) as every Monte Carlo simulation uses the CHT for charged particle transport[40]. In EGSnrc, several AEITs are generally used to improve the efficiency of a simulation, these include: range rejection, transport cut-off and bremsstrahlung splitting.

Range rejection: In range rejection, the residual range of an electron is calculated. If the range is such that it cannot escape with threshold energy from the region, its history is terminated, depositing all of its energy at that point. An energy threshold is applied as the technique ignores the creation of bremsstrahlung or annihilation photons as the electron or positron continues to slow down. The efficiency of this technique is proportional to the energy threshold, however setting the threshold energy too high can result in erroneous results[38,40].

Transport cut-off: If a particle's energy falls below a cut-off energy the particle's history is terminated and all of its energy is deposited at that point. Two separate transport cut-off energies are typically defined for electrons and photons. For the megavoltage

energies simulated in radiotherapy, the photon transport cut-off energy (PCUT) and electron transport cut-off energy (ECUT) are typically set to 10 keV and 0.521 or 0.700 MeV (including the rest mass), respectively.

Bremsstrahlung Splitting: Bremsstrahlung splitting involves creating *N* bremsstrahlung photons at each bremsstrahlung interaction site and reducing their statistical weights by a factor of 1/*N*. However, in doing this many secondary electrons are created by the *N* photons, thereby increasing the computational time. As a result, Russian Roulette is played on these secondary electrons. This has the result of restricting the number of electrons to the same number as would occur if bremsstrahlung splitting was not used, essentially "shooting down" every *N*-1 electrons, thereby increasing the weight of the remaining electrons by a factor of *N*. There are currently several bremsstrahlung splitting techniques: uniform (UBS), selective (SBS) and directional bremsstrahlung splitting (DBS)[38].

For the purposes of this work, SBS was used in all linac simulations. SBS was used for consistency with Orton and Robar[7], who previously validated the models. SBS involves creating a uniform distribution of photons at the bremsstrahlung event, but, depending upon the direction of the electron relative to the field-of-interest (FOI) (e.g. the field size at isocenter), a maximum or minimum splitting number is applied. If the electron is moving towards the FOI, the maximum splitting number is applied. If the electron is moving in the opposite direction of the FOI, a minimum splitting number is applied, typically one-tenth of the maximum splitting number. The size of the FOI is recommended by Rogers *et al*.[41] to be 10 cm larger than the largest field size set by the

linac collimation, for example, a 10 × 10 cm^2 field defined at isocenter would have a FOI of 20 × 20 cm^2. SBS improves the efficiency of the simulation by a factor of approximately 20 without Russian roulette and 65 with Russian roulette[40,42].

CHAPTER 6 IMAGING PHYSICS

In this chapter, imaging physics is discussed, including: a brief introduction, the mathematics behind image reconstruction and how it is applied to computed tomography and cone-beam computed tomography.

6.1 Introduction

Radiographic imaging relies upon the variation in the mass attenuation coefficient between different tissues within the body. Hendee and Ritenour[6] describe the human body as composed of three main body tissues: fat (adipose), muscle and bone, with air present in the lungs, sinuses and gastrointestinal tract.

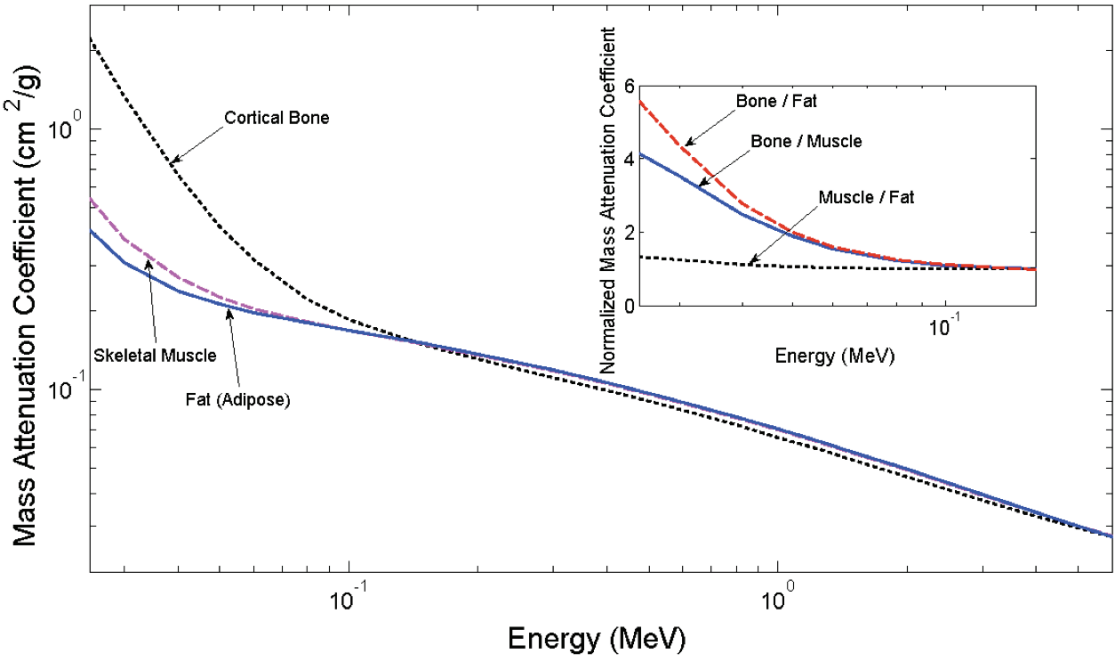

Figure 6.1 Mass attenuation coefficients in the diagnostic and therapeutic energy domain for cortical bone, skeletal muscle and fat (adipose). Inserted figure shows the normalized mass attenuation coefficients for bone and fat, bone and muscle and muscle and fat. Data was obtained from the National Institute of Standards and Technology (NIST), Washington, DC[27].

As shown in figure 6.1, low energy photons provide the greatest variation in the mass attenuation coefficient between the main body tissues. This is a result of the large photoelectric cross section in this energy range. At higher energies, the difference in the mass attenuation coefficients between the main body tissues is minimal, this is due to Compton interactions dominating in this energy range. As shown in table 6.1 and in equation 2.25 and 2.27, this is due to the small variation in the electron density as compared to the large difference in the effective atomic number between the main body tissues.

Table 6.1 Properties of tissue constituents of the human body[6].

Tissue	Effective Atomic Number	Density (kg/m^3)	Electron Density (electrons/kg)
Muscle	7.4	1.00	3.36 x 10^{26}
Fat	5.9-6.3	0.91	3.34-3.48 x 10^{26}
Bone	11.6-13.8	1.65-1.85	3.00-3.10 x 10^{26}

As a result of the variation in tissue composition along a ray-line, the number or intensity of photons detected varies. Starting with equation 2.38 for a monoenergetic beam, the attenuation of photons as they propagate through biological tissue can be written as:

$$\ln \frac{N_o}{N} = \int_{Ray} \mu(x,y) ds. \qquad \text{Eq 6.1}$$

This is a line integral and is the basis for planar imaging and image reconstruction.

6.2 Fourier Slice Theorem and Filtered Backprojection

Figure 6.2 shows an object f(x,y) being imaged and its resulting projection $P_\theta(t)$. The equation of a line from AB is defined as:

$$x\cos\theta + y\sin\theta = t. \qquad \text{Eq 6.2}$$

With this, the value of the $P_\theta(t)$ can be defined with the following integral:

$$P_\theta(t) = \int_{(\theta,t)\ \text{line}} f(x,y)ds = \int_{-\infty}^{\infty}\int_{-\infty}^{\infty} f(x,y)\ \delta\left(x\cos\theta + y\sin\theta - t\right)\ dxdy \qquad \text{Eq 6.3}$$

Equation 6.3 is known as the Radon transform of $P_\theta(t)$ for the function f(x,y). Combining many sets of parallel line integrals forms a complete projection.

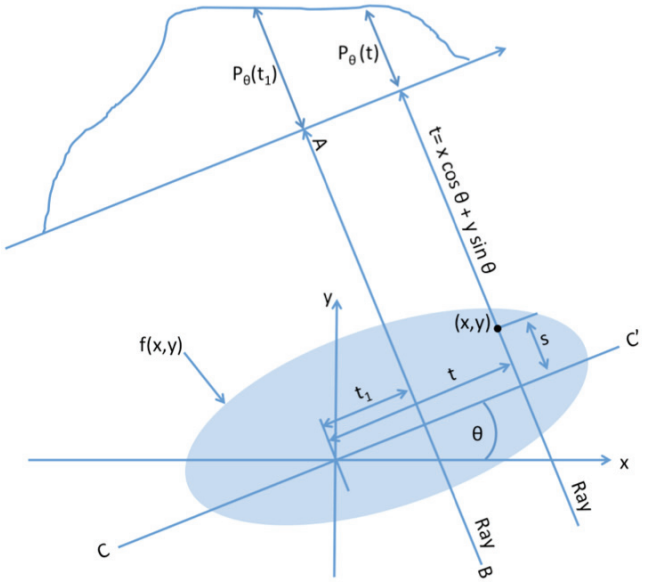

Figure 6.2 An object f(x,y) being irradiated by parallel rays to form a projection $P_\theta(t)$ at angle θ[43].

To estimate the original object from the projection data, a technique called the Fourier slice theorem is used. This involves taking the Fourier transform of a parallel projection and setting it equal to a slice of the two-dimensional (2D) Fourier transform of the original object. It is then possible to estimate the original object by performing the inverse 2D Fourier transform. The 2D Fourier transform of the image is defined as:

$$F(u,v) = \int_{-\infty}^{\infty} \int_{-\infty}^{\infty} f(x,y)\, e^{-j2\pi(ux+vy)}\, dxdy. \qquad \text{Eq 6.4}$$

And the Fourier transform of the projection at angle θ is defined as:

$$S_\theta(w) = \int_{-\infty}^{\infty} P_\theta(t) e^{-j2\pi wt} dt. \qquad \text{Eq 6.5}$$

In the (t,s) coordinate system, a projection along line of constant t can be written as:

$$P_\theta(t) = \int_{-\infty}^{\infty} f(t,s)\, ds, \qquad \text{Eq 6.6}$$

the Fourier transform in equation 6.5 becomes:

$$S_\theta(w) = \int_{-\infty}^{\infty} \left[\int_{-\infty}^{\infty} f(t,s) ds \right] e^{-j2\pi wt} dt, \qquad \text{Eq 6.7}$$

in the (x,y) coordinate system this becomes:

$$S_\theta(w) = \int_{-\infty}^{\infty} \int_{-\infty}^{\infty} f(x,y)\, e^{-j2\pi w(x\cos\theta + y\sin\theta)}\, dxdy. \qquad \text{Eq 6.8}$$

This gives both Fourier transforms in terms of the spatial frequency *w*, such that

$$S_\theta(w) = F(w\cos\theta, w\sin\theta). \qquad \text{Eq 6.9}$$

From this taking projections of an object at angles θ_1, θ_2, …, θ_n and the Fourier transform of each projection, the values of F(u,v) can be determined. Knowing F(u,v) allows f(x,y) to be recovered by taking the inverse Fourier transform:

$$f(x,y) = \int_{-\infty}^{\infty} \int_{-\infty}^{\infty} F(u,v)\, e^{j2\pi(ux+vy)}\, dudv. \qquad \text{Eq 6.10}$$

An example of how the number of projections increases the accuracy in recovering an object is shown in figure 6.3.

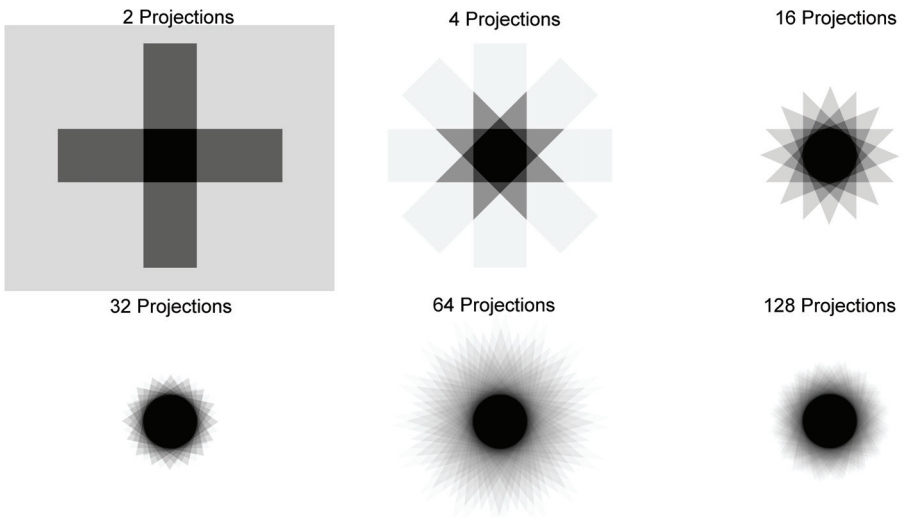

Figure 6.3 Simple backprojection with increasing projections to show improvement in the reconstructed image.

6.2.1 Parallel Ray Reconstruction

Fourier slice theorem can provide an estimate of the object given that enough projections are taken at enough angles, however in practice this leads to high density within the center and severe blurring in the reconstructed image (Fig 6.4). To correct this, the projections are filtered in either the real or frequency domain. The reconstruction can be then split into two parts: filtering and backprojection. A common filter used is a ramp filter. In the frequency domain, a ramp filter is the absolute value of *w*. The filter has the properties of filtering out low frequencies and passing high frequencies, with a linear behaviour between low and high frequencies. This has the effect of emphasising high contrast (high frequency) and minimizing blurring (low frequency). However, as a consequence of a ramp filter, unwanted noise could be created as a result of the emphasis of high frequencies. As a result, several other high-pass filters are commonly used such as the Stepp-Logan, cosine, Hamming or Hann.

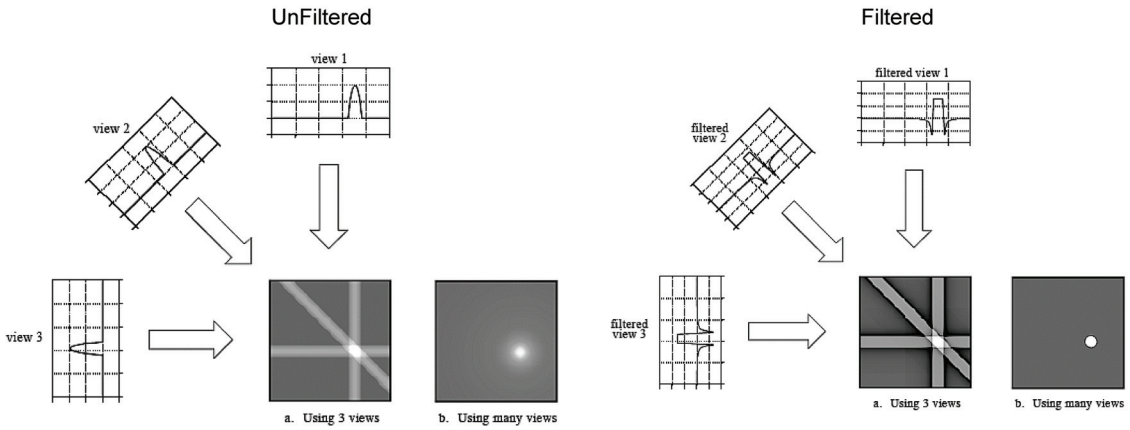

Figure 6.4 An example of filtered and unfiltered backprojection and the resulting image quality of each. The figure was taken with permission from *The Scientist and Engineer's Guide to Digital Signal Processing*[44].

The backprojection is simply the summation of the entire 2D inverse Fourier transforms of each filtered projection. The algorithm for filtered backprojection is then:

1) Measure projection, $P_\theta(t)$
2) Fourier transform $P_\theta(t)$ to find $S_\theta(w)$
3) Multiply $S_\theta(w)$ by a filter
4) Sum the inverse Fourier transform of the filtered projections

Mathematically, this algorithm begins with equation 6.5 in polar coordinates (w,θ):

$$f(x,y) = \int_0^{2\pi} \int_0^{\infty} F(w,\theta)\, e^{j2\pi w(x\cos\theta + y\sin\theta)}\, w\, dw\, d\theta. \qquad \text{Eq 6.11}$$

Equation 6.11 can be simplified to give:

$$f(x,y) = \int_0^{\pi} \left[\int_{-\infty}^{\infty} F(w,\theta)\, w e^{j2\pi wt} dw \right] d\theta. \qquad \text{Eq 6.12}$$

Substituting the Fourier transform of the projection at angle θ, equation 6.12 becomes:

$$f(x,y) = \int_0^{\pi} \left[\int_{-\infty}^{\infty} S_\theta(w)\, |w| e^{j2\pi wt} dw \right] d\theta = \int_0^{\pi} Q_\theta(t) d\theta. \qquad \text{Eq 6.13}$$

where $Q_\theta(t)$ represents the filtered projection of $S_\theta(w)$. However, since not every angle between 0 and π will have a projection, equation 6.13 is approximated with N projections as:

$$f(x,y) = \frac{\pi}{N} \sum_i^N Q_{\theta_i}(t). \qquad \text{Eq 6.14}$$

6.3 CT Reconstruction

Practically, parallel-ray projections are not taken to reconstruct images. This method is inherently slow due to the acquisitions of a relatively small volume of tissue in a parallel ray. Clinically, a point source is used to acquire a two-dimensional (2D) fan (Fig. 6.5a) or a three-dimensional (3D) cone (Fig. 6.5b) of tissue, these techniques are known as computed-tomography (CT) and cone-beam computed-tomography (CBCT), respectively.

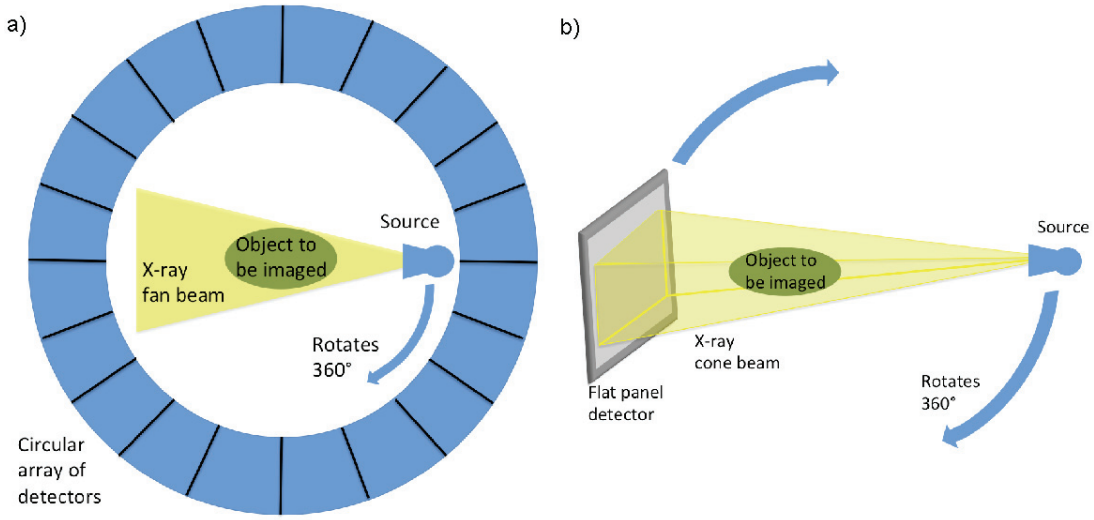

Figure 6.5 (a) Fan-beam computed tomography and (b) cone-beam computed tomography.

6.3.1 Fan-Beam Reconstruction

In fan-beam CT, a series of thin axial projections are acquired from a source that emits a narrow fan of radiation that is rotated around the object and then detected by a concave spherical detector. An image is reconstructed by modifying equation 6.13 to account for the fan-beam orientation used:

$$f(x,y) = \int_0^{2\pi} \frac{D^2}{L(x,y,\beta)} \widetilde{R_\beta}\left(\beta,\gamma(x,y,\beta)\right)d\beta, \qquad \text{Eq 6.15}$$

where

β is the angle of rotation between the source and the reference axis,

γ is the angle of rotation within the fan,

D is the source to axis of rotation distance,

$L(x,y,\beta)$ is the point spread distance and is equal to

$(D^2 + x\cos\beta + y\sin\beta)^2 + (-x\sin\beta + y\cos\beta)^2$,

$\widetilde{R_\beta}\left(\beta,\gamma(x,y,\beta)\right)$ is the weighted and ramp filtered projection at angle β,

$\gamma(x,y,\beta)$ is the ray intersecting the calculation point and is equal to

$$\tan^{-1}\frac{-x\sin\beta + y\cos\beta}{D + x\cos\beta + y\sin\beta}$$

If the detector used is not concave, but flat equation 6.15 becomes:

$$f(x,y) = \int_0^{2\pi} \frac{D^2}{U(x,y,\beta)^2} R_\beta^F\left(\beta,u(x,y,\beta)\right)d\beta, \qquad \text{Eq 6.16}$$

where

$U(x,y,\beta)$ is the distance between the source and the line parallel with the detector that intersects the image point (x, y) and is equal to

$$U(x,y,\beta)=D+x\cos\beta+y\sin\beta,$$

$R_{\beta}^{F}(\beta,u(x,y,\beta))$ is the weighted and ramp filtered projection at angle β,

$u(x,y,\beta)$ is the detector position and is equal to

$$u(x,y,\beta)=D\frac{-x\sin\beta+y\cos\beta}{D+x\cos\beta+y\sin\beta}.$$

A series of 2D reconstructions or "slices" are then stacked along the axis of rotation to form a 3D image.

6.3.2 Cone-Beam Reconstruction

In CBCT, a source emits a broad cone of radiation, which is rotated around an object and is typically detected by a flat detector. CBCT images are reconstructed using a modified version of equation 6.16 to account for the cone geometry, which is essentially composed of a stack of fan-beams. In 1984, Feldkamp, Davis and Kress[45] (FDK) outlined an algorithm to reconstruct CBCT images, in which $R_{\beta}(t,u,v)$ is read row by row in the *u* direction (Fig 6.6). Each value of *u* along the line BC is first pre-weighted to account for the cone geometry and that the detector is flat and not a concave sphere. The pre-weight takes into account the fan and cone angle (i.e. the vertical and horizontal angle of the cone from the central axis) and is defined as:

$$R_{\beta}^{'}(\beta,u,v)=R_{\beta}(\beta,u,v)\frac{\sqrt{D^2+u^2}}{\sqrt{D^2+u^2+v^2}}. \qquad \text{Eq 6.17}$$

where

$v(x,y,z,\beta)$ is equal to $z\frac{D}{D+x\cos\beta+y\sin\beta}$.

This has the effect of projecting the cone-beam data detected at point B on to the scanning plane (t,u) at point x', and for a single plane, it can be ramp filtered and reconstructed using equation 6.15.

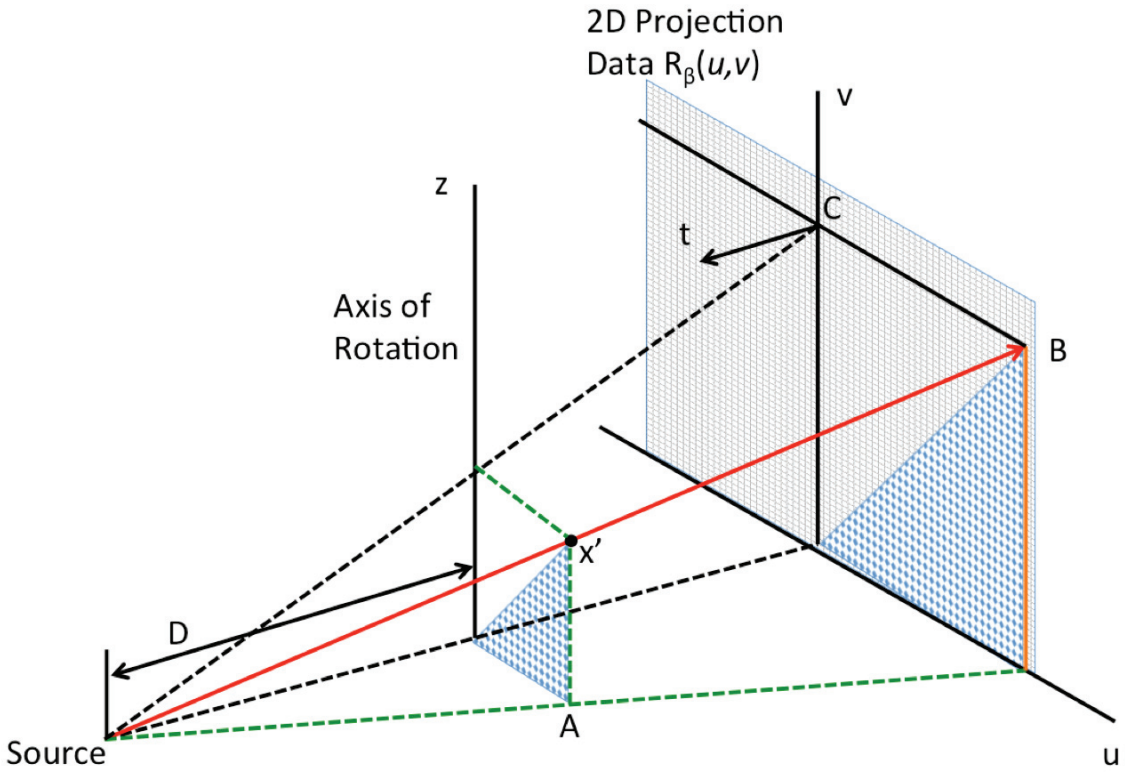

Figure 6.6 Projection of the cone-beam data $R_\beta(\beta,u,v)$ at point (u,B) back onto the scanning plane (t,u) at point x'.

CHAPTER 7 MATERIALS AND METHODS

7.1 LOW-Z TARGET BEAM PRODUCTION

The 6 MV and low-Z target beams were generated using a Varian 2100EX linear accelerator (Varian Medical Systems, Inc., Palo Alto, CA). Figure 7.1 shows the two separate low-Z targets we investigated: (i) 6.7 mm thick aluminum (ρ=2.69 g/cm^3) and (ii) 7.6 mm thick carbon (ρ=1.88 g/cm^3).

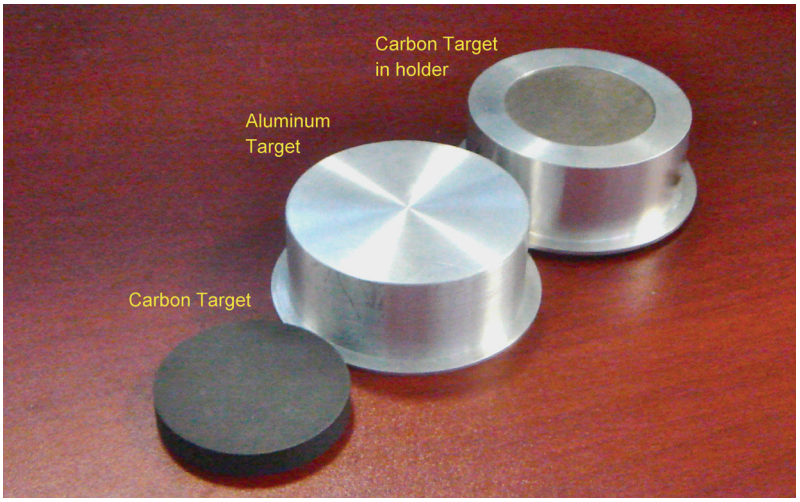

Figure 7.1 The two low-Z targets used to produce photon beams below 2.40 MeV. Shown are the 2.35 MeV carbon target, aluminum target and the 2.35 MeV carbon target in its aluminum holder.

The aluminum target was originally designed and used by Robar *et al.*[17] previously for a 3.5 MV beam. The thickness of the carbon target was calculated to coincide with the CSDA range for a 2.5 MeV electron. While an increase in low-Z target thickness slightly degrades spatial resolution[18], a "full-thickness" target alleviates the need for a polystyrene filter to absorb transmitted electrons and increases the production of lower energy photons[9]. As described previously[7,17,18], when used experimentally, the carousel

was operated in manual mode and the appropriate target is rotated into the beam line via a rotary switch. For this work, the linac was operated in electron mode and equipped with a dedicated 4 MeV program board used for research purposes only. The bending magnet was adjusted to tune the beam energy down from the nominal operating point of 4.5 MeV to the lower energies required. As shown in figure 7.2 the low-Z targets were mounted to the beam side of the carousel. The elevated target holder vertically offsets the target 0.9 cm from the beryllium exit window of the primary collimation vacuum. By keeping the target as close as possible to the beryllium exit window the amount of electron scattering in air is minimized[7,15,18].

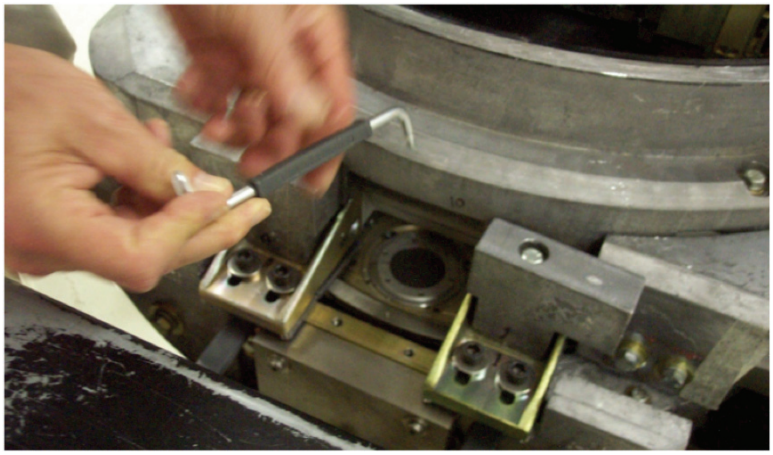

Figure 7.2 Low-Z target being installed in the linac carousel.

7.1.1 Beam Tuning

Adjustment of the bending magnet current can be used to select the mean energy of electrons exiting the bending magnet, with electrons outside the mean energy being stopped within the linac head. When using this technique, the number of electrons within the selected energy window decreases when the selected energy

differs from the nominal energy for the selected mode. This is due to the irregular electron spectra exiting the waveguide. Although the electron energy spectrum exiting the waveguide is often approximated as Gaussian[46–48], in fact, it can be highly asymmetric[46,47] with a sharp decrease in electron population away from the nominal energy. An example of this can be seen in the work by Wei *et al.*[46], which gives electron spectra reconstructed from depth dose curves. Their results demonstrate that low-energy electrons, e.g., ranging from 1 to 3 MeV, are present in a 6 MeV spectrum, however, the relative fluence of these electrons is approximately one hundredth of that at the nominal energy. As a result, any lowering of the incident electron energy results in a considerably lower beam current exiting the bending magnet and, for our application, significantly protracted image acquisition times. A solution, without significant alteration to the waveguide, is to increase the total current exiting the waveguide. To observe slight changes in beam current, a 4 MeV tantalum electron scattering foil was inserted into the beam line via a rotatory switch controlling the carousel. The linac was operated in 4 MeV electron mode at a MU rate of 1000 MU/min with the dose servos turned off. In maximizing beam current, we optimized the combination of two parameters: gun High Voltage (HV) and grid voltage, over the full ranges of each parameter recommended by the manufacturer for clinical operation. Course setting of both parameters is done inside the gun deck of the linear accelerator, while the grid voltage may also be fine-tuned from outside the room with the beam on using the "gun-I" potentiometer. The process of maximizing beam current thus involved: i) setting the first gun HV value in the range, ii) setting the first grid voltage

coarse value on the gun deck, iii) fine-tuning the grid voltage with the beam on and iv) recording the maximum achievable dose rate. For the same gun HV setting, the next coarse grid HV value was then set on the gun deck, and fine-tuned. After exploring the full allowable range of grid HV, the next gun HV setting was chosen on the gun deck. This was repeated to produce a two dimensional matrix of measured dose rate values, from which the optimal combination of the two parameters was chosen. Finally, for this combination, the solenoid and buncher cavity steering set points were tuned on the program board to further tune beam current. To avoid potential damage, the examined range did not exceed the recommendations by Varian. Finally, once the final tuning was complete, the scattering foil was replaced by either aluminum or carbon targets for x-ray production.

7.1.2 Electron Energy Determination

Over the low electron energy range produced here, the relationship between bending magnet and electron energy was not known precisely based on manufacturer specifications. To determine incident electron energy, the 4 MeV tantalum electron scatting foil described previously was rotated into the beam line. Percent depth dose (PDD) curves were measured in a 50x50x50 cm^3 scanning water tank (Scandtronix, Uppsala, Sweden) with a p-type silicon electron field diode (EFD, Scandtronix, Uppsala, Sweden) at a source to surface distance (SSD) of 100 cm and with a 10x10 cm^2 electron applicator. Measurements were taken at 0.2 mm intervals. These curves were then matched to Monte Carlo PDD curves of known electron energy.

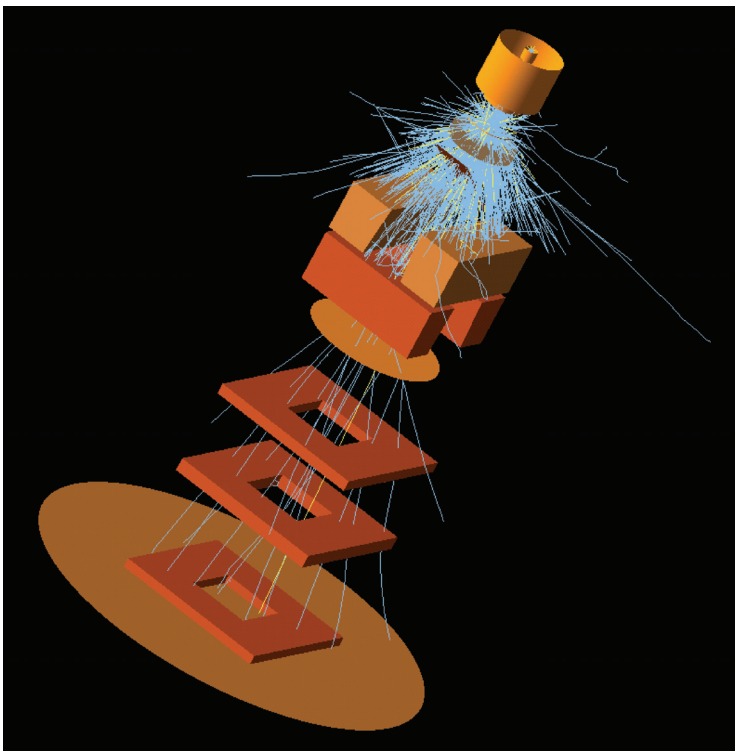

Figure 7.3 BEAMnrc simulation of 2.35 MeV electrons (blue) incident on a tantalum electron scattering foil with bremsstrahlung photons (yellow). Shown (from the top down) is the primary collimator (FLATFILT), Ta scattering foil (FLATFILT), monitor chamber (SLABS), mirror (MIRROR), jaws (JAWS), mylar exit window (SLABS) and the electron applicator (PYRAIMDS).

BEAMnrc[38] (Fig. 7.3) and DOSXYZnrc[37] were used to simulate the linac and water phantom. All simulations were run in accordance with the physical set-up using validated models provided by Orton and Robar[7]. Parallel beams of mono-energetic electrons were used with a spot size of 0.1 cm. $3x10^8$ and $1.8x10^9$ particle histories were simulated in BEAMnrc and DOSXYZnrc, respectively. Global electron (ECUT) and photon (PCUT) transport cut-off energies of 0.521 MeV and of 0.010 MeV, respectively, were used. The incident electron energy was varied in 0.025 MeV increments between 1.700 MeV to 2.500 MeV and plotted in MATLAB (Mathworks, Natick, MA) against the measured data.

7.1.3 Photon Measurements

Given that low-Z target photon beams have not been produced previously using the low electron energies considered here, it was of interest to examine depth dose characteristics. Photon depth dose measurements were acquired using a 50x50x50 cm^3 water tank with 0.015 cm^3 (PTW N31014, Freiburg, Germany) and 0.125 cm^3 (PTW N31010, Freiburg, Germany) cylindrical ion chambers. For all measurements, an SSD of 100 cm and a field size of 10x10 cm^2 were used. The 0.015 cm^3 ion chamber was used for measurements shallower than 1.0 cm below the surface to provide resolution in the build-up region, while the 0.125 cm^3 ion chamber was used for improved signal-to-noise characteristics at greater depths. These two sets of data were concatenated at a depth of 1.0 cm and the resultant curve was normalized to the maximum dose. In the build-up region the use of a parallel plate ionization chamber was investigated, however, for the beam lines investigated, the 0.015 cm^3 cylindrical ion chamber produced more consistent readings within this region. Photon depth dose measurements were acquired for both carbon and aluminum targets, for the minimum and maximum energies examined in this investigation, which, using the method described in section 7.1.2, were determined to be 1.90 MV and 2.35 MV.

7.1.4 Photon Monte Carlo Simulations

In order to study changes in photon fluence with energy and target material, BEAMnrc[38] was used to simulate the linac beam-line. The linac was modeled in accordance with the physical set-up using validated models provided by Orton and Robar[7] (Fig 7.4). $1.1x10^8$ incident electron histories were run for the aluminum and

carbon targets, with energies of 1.90 and 2.35 MeV. Linac collimation was set to a field size of 10x10 cm^2 (specified at isocenter). Selective bremsstrahlung splitting was used, and as recommended by Rogers *et al.*[41] an effective splitting field size of 20x20 cm^2 was used at an SSD of 100 cm with minimum and maximum bremsstrahlung splitting numbers of 100 and 1000, respectively. PCUT and ECUT were set to 0.010 MeV and 0.700 MeV, respectively. ECUT was increased from 0.521 MeV to improve the efficiency in simulating electron transport within the low-Z target. For confirmation of the modeled spectra, relative depth doses were run for the aluminum target at 1.90 MV and 2.35 MV in DOSXYZnrc[37] and compared to corresponding measured results. To determine the spectral distributions, BEAMdp[39] was used to analyze the phase space data. To determine the source of the photons and their resultant spectral contribution, the LATCH feature was utilized to identify the origin of generated photons. In addition to simulating the two homogeneous carbon or aluminum targets, a carbon target with various thickness of copper (on the exit side) was modeled to examine the requirements for filtration of very low energy (e.g. < 25 keV) photons that would contribute to superficial patient dose but not image formation.

Figure 7.4 Monte Carlo simulation of the Varian 2100EX linac with the therapeutic target and flattening filter removed and a carbon target placed at the level of the flattening filter

7.2 IMAGING SYSTEM AND IMAGE QUALITY

7.2.1 aS1000/IAS3 Image System

An aS1000/IAS3 system (Varian Medical Systems, Inc.) was used for all imaging. The system was setup as a stand-alone configuration separate from the clinical imaging system on the treatment unit. The aS1000 panel (IDU20) has an active area of 30x40 cm^2 and includes a 1.0 mm Cu build-up plate, a Gd_2O_2S:Tb scintillating phosphor layer and a 1024x768 array of photodiodes switched by thin-film transistors deposited on a glass substrate. The number of monitor units (MU) per exposure was varied to control the dose to the phantoms, where the IAS3 allows cMU control of this parameter. Prior to imaging, flood field and dark field calibrations were performed where the former has the effect of correcting for the forward peaked nature of the low-Z target, flattening

filter free beam. The dark field image corrects for dark currents within the detector and variability in amplification of collected charge among multiplexed detector elements.

7.2.2 Contrast-to-Noise Ratio

To observe changes in contrast-to-noise ratio (CNR) with target material and energy, a contrast phantom was constructed for planar imaging. The phantom, shown in figure 7.5, consisted of an 18x18x3 cm^3 block of polystyrene with six circular holes of 2.5 cm diameter each for tissue equivalent materials (Gammex, Middleton, WI). To measure dose, a channel was added along the phantom midline to accommodate a 0.125 cm^3 cylindrical ion chamber (PTW N31010, Freiburg, Germany). The chamber was calibrated for the low-Z target beams by measuring the dose per MU in Solid Water (Gammex, Middleton, WI) with thermoluminescent dosimeters (TLDs) (TLD-800, Saint-Gobain Crystals, Hiram, OH) at an SSD of 95 cm and depth of 5 cm with a 10x10cm^2 (defined at isocenter) field size. Manganese doped lithium tetraborate ($Li_2B_4O_3$:Mn) TLDs were used due to their minimal energy dependence[4] (0.9 at 30 keV/^{60}Co). The TLDs were then removed and replaced by the ionization chamber in the same location to obtain a conversion from collected charge to cGy. This was done for the 2.35 MV carbon and aluminum target beams. CNR was calculated as:

$$\mathrm{CNR}=\frac{\left|P_{\mathrm{material}}-P_{\mathrm{polystyrene}}\right|}{\sqrt{\sigma^2_{\mathrm{material}}+\sigma^2_{\mathrm{polystyrene}}}}, \qquad \text{Eq 7.1}$$

where

$P_{material}$ is the average pixel value within the insert,

$P_{polystyrene}$ is the average value of the surrounding polystyrene,

$\sigma_{material}$ is the average noise within the material,

$\sigma_{polystyrene}$ is the average noise in the surrounding polystyrene.

Pixel values in the surrounding polystyrene were measured within two concentric circles with radii of 1.8 and 2.1 cm (measured at isocenter). Error bars were found by calculating the mean and standard deviation of CNR measured in multiple images.

Figure 7.5 The CNR phantom with tissue equivalent inserts.

7.2.3 Relative Modulation Transfer Function

Images of the QC3 phantom[49] were taken to measure the relative modulation transfer function (RMTF) of the system. These images were analyzed according to the method outlined by Rajapakshe *et al.*[49], where the relative modulation transfer function (RMTF) is defined as:

$$\mathrm{RMTF}=\frac{\mathrm{M(f)}}{\mathrm{M(f_1)}} \quad , \qquad \text{Eq 7.2}$$

where *M(f)* is the output modulation of the line pair in a region of interest and $M(f_1)$ is the output modulation for the lowest frequency line pair region. As suggested by Droege and Morin[50], the output modulation is obtained by using the relationship between the signal amplitude and its variance and is given by:

$$\mathrm{M^2(f)}=\sigma_{\mathrm{m}}^2\mathrm{(f)}\text{-}\sigma^2\mathrm{(f)}, \qquad \text{Eq 7.3}$$

where $\sigma_m^2(f)$ is the measured total variance within a region of interest and $\sigma^2(f)$ is the variance due to random noise within the region of interest. The variance due to random noise as calculated by Rajapakshe *et al.*[49] is given by:

$$\sigma^2\mathrm{(f)}=\frac{\sigma_{\mathrm{sub}}^2}{2}, \qquad \text{Eq 7.4}$$

where $\sigma^2(f)$ represents the variance within the region of interest of two subtracted images. Error bars were found by calculating the mean and standard deviation of RMTF measured in multiple image sets.

7.3 Planar Image Quality below 2.4 MeV

7.3.1 Contrast-to-Noise Ratio

To observe changes in image quality with changing energy and target composition the CNR phantom was imaged at 1.90, 2.15 and 2.35 MV with both aluminum and carbon targets. The setup for imaging was as follows: the gantry and couch were rotated to 90°, the imaging panel was placed in a stand located on the couch with fine adjustment screws and levelled to ensure orthogonality of the panel and

the beam axis, a source-to-detector distance (SDD) of 140 cm was set. During imaging, the phantom was oriented as shown in figure 7.6, such that the circular cross sections of material regions faced the beam and the phantom was centered on the linac isocenter. Images were acquired with dose values at the phantom center ranging from approximately 0.01 to 0.16 cGy. This low dose range was chosen to match a typical anticipated dose per projection used in CBCT, given that this is a likely application of the low-Z target beam[17]. While the 3 cm thick phantom in figure 7.5 allows sensitivity in measuring changes of CNR with beam parameters, it is not representative of typical patient separation. Thus, the experiment was repeated with the phantom padded by 5 cm of solid water on the source side and 7 cm on the detector side, for a total phantom thickness of 15 cm. The tissue substitutes used were 2.5 cm in diameter and 3.0 cm thick and simulated cortical bone 30% (electron density relative to water, ρ_e^w= 1.28), inner bone (ρ_e^w= 1.09), brain (ρ_e^w= 1.05) and breast (ρ_e^w= 0.96).

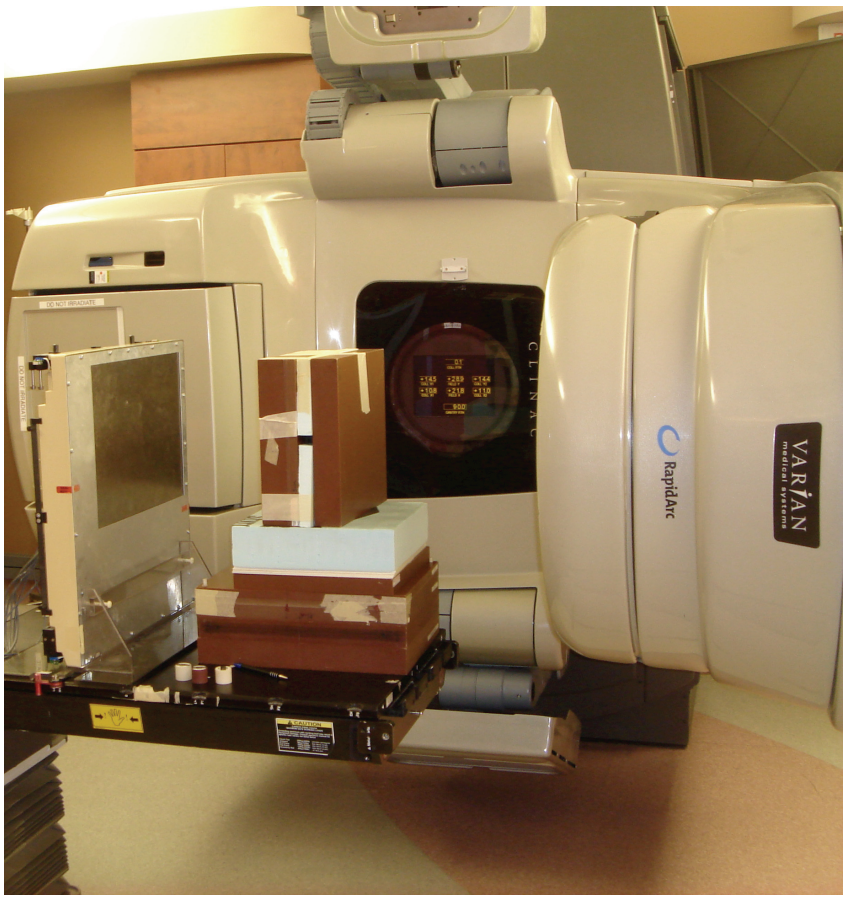

Figure 7.6 The experimental setup for planar imaging.

7.3.2 Spatial Resolution

To observe changes in spatial resolution with varying energy, the QC3[49] (SeeDOS Ltd., Bedfordshire, UK) spatial resolution phantom was imaged with the 1.90, 2.15 and 2.35 MV/Carbon beams. The QC3 (Fig 7.7) phantom contains line pair regions of 0.1, 0.2, 0.25, 0.4 and 0.75 line pairs per mm that consist of alternating bars of lead and Delrin (Fig 7.7). The same setup was used as described in section 7.3.1 with the CNR phantom being replaced by the QC3 phantom. An approximate imaging dose of 0.19 cGy was delivered to the center of the phantom located at isocenter.

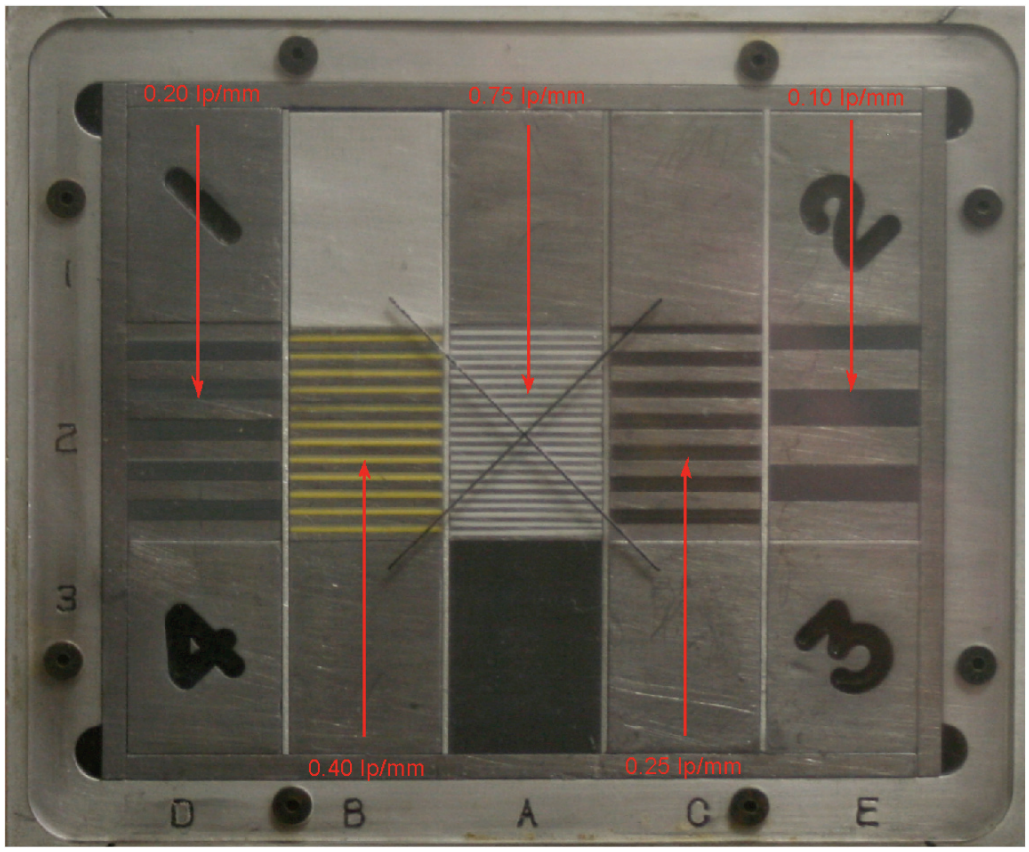

Figure 7.7 The QC3 phantom with spatial resolution regions shown.

7.3.3 Qualitative Planar Imaging

Planar imaging of a sheep head was done to observe the qualitative effects on imaging with changes in target composition and energy. For these images, the CNR phantom was replaced with a sheep head and all other setup parameters were unchanged. An approximate imaging dose of 0.14 cGy was delivered to the center of the head located at isocenter. Images were acquired at 2.35 MV with both carbon and aluminum target beams and a 6 MV therapeutic beam. The resultant images were analyzed in MATLAB and were compared with identical gray level window settings.

7.4 The Effect of Copper in the IDU20

7.4.1 Monte Carlo Simulations

In order to study the effects of the copper conversion plate on the 2.35 and 7.00 MV spectra, Monte Carlo simulations were run using BEAMnrc[38]. The 7.00 MV beam was used to investigate the dependence of the effect of the copper layer on beam energy. The linac and IDU20 were modeled in accordance to the physical setup using validated models provided by Orton and Robar[7]. It should be noted that these models were originally of an aS500 imaging panel, however comparing the two detectors, the physical composition is relatively consistent with the main difference being the number of pixels within the active area of the detector. 2.0×10^7 incident electron histories were run for both 2.35 and 7.00 MV beams. Linac collimation was set to match the active area of the detector at a source to detector distance of 140 cm. Selective bremsstrahlung splitting was used, and as recommended by Rogers *et al.*[41], an effective splitting field size of 50 x 50 cm^2 was used for source-to- surface distance (SSD) of 140 cm with minimum and maximum bremsstrahlung splitting values of 200 and 1000, respectively. ECUT and PCUT cut-off energies of 0.700 MeV and of 0.010 MeV, respectively, were used. The resulting phase space was recorded at the exit side of the copper conversion plate, above the phosphor. To study the effect of the copper conversion plate thickness on the energy spectra, the thickness was varied in 0.2 mm increments from 0 mm to 1.6 mm, corresponding with the physical setup of experiments, as described below. To determine the spectral distributions, BEAMdp[39]

was used to analyze the phase space data. The resulting data was analyzed and plotted using MATLAB.

The IDU20 was also modeled in DOSXYZnrc[37] to determine the effect the thickness of the copper conversion plate has on detector response. Similar to the methods used by Roberts *et al.*[15,21], mono-energetic pencil beams of varying energy from 0.010 MeV to 7.00 MeV were incident on the detector, and the detector response was quantified by scoring dose deposited in the phosphor screen per incident particle. 5.0×10^7 incident photons were used for all simulations, with PCUT and ECUT set to 0.010 MeV and 0.521 MeV, respectively. For increased accuracy in electron transport within the phosphor layer of the IDU20, a lower ECUT value was used in this simulation. Detector response simulations were repeated for 0 mm, 1.0 mm and 1.6 mm copper thicknesses. The dose distributions were analyzed with MATLAB and plotted with energy fluence for 2.35 and 7.00 MV/Carbon beams.

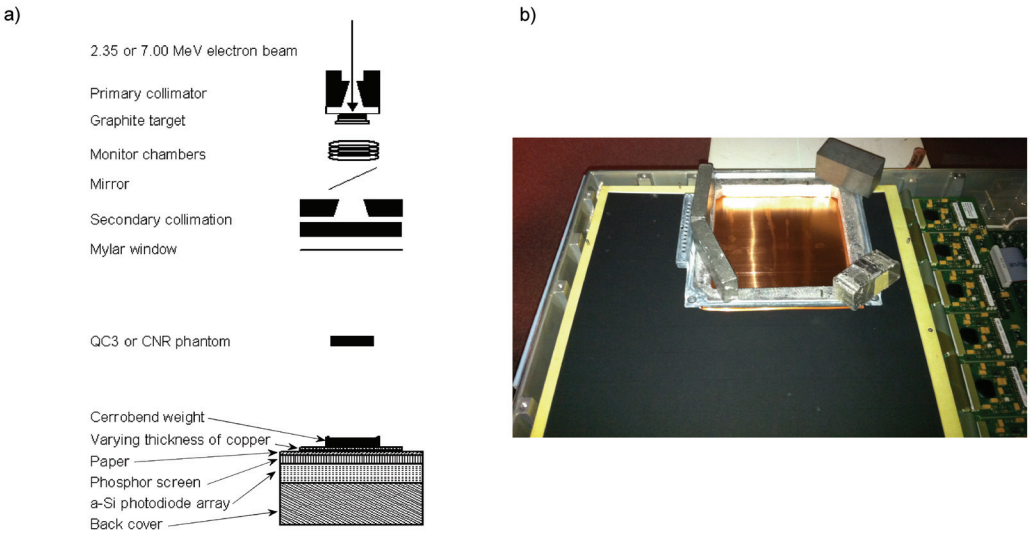

Figure 7.8 Diagram of the full imaging system, (a) A schematic drawing on the linac and detector. (b) A photo of the detector with the cover off with copper plates and Cerrobend weights.

7.4.2 Planar Image Quality – Physical Measurement

To observe changes in image quality with varying thicknesses of copper, the gantry was rotated to zero degrees (in IEC coordinates) and the detector was oriented perpendicular to the central axis at an SDD of 140 cm, a schematic diagram of the experiment is shown in figure 7.8a. To decrease the amount of backscatter radiation, Styrofoam blocks supported the detector from the floor. The detector cover, foam spacing materials and copper conversion plate were removed. To vary the thickness of copper, 14 x 14 x 0.02 cm^3 copper sheets were stacked on the paper sheet covering the scintillator. This allowed for the thickness of copper to range from 0 mm to 1.6 mm in 0.2 mm increments. To compress the copper sheets, a customized Cerrobend frame was manufactured to apply pressure around the periphery of the stacked copper sheets, and the weight of the frame was increased until it was observed that all layers of copper were compressed firmly against the panel. To quantify changes in image quality, the planar CNR (Fig 7.5) and QC3 (Fig 7.7) spatial resolution phantom were alternately positioned on the central axis. The tissue substitutes used were 2.5 cm in diameter and 3.0 cm thick and simulated cortical bone 60% (ρ_e^w= 1.69), cortical bone 30% (ρ_e^w= 1.28), inner bone (ρ_e^w= 1.09), brain (ρ_e^w= 1.05) and lung (ρ_e^w= 0.44). A relatively thin phantom was used as it allows sensitivity in measuring changes of CNR with copper thickness. The beam was collimated to 10x10 cm^2 at an SSD of 140 cm. An imaging dose of 0.02 cGy was delivered to the center of the CNR phantom to be representative of the approximate dose per projection given in CBCT. A higher dose of 0.19 cGy was delivered

to the center of the QC3 phantom for spatial resolution measurements. A higher dose was used as a consequence of high noise at 0.02 cGy resulting in spurious results.

Planar imaging of a sheep head was done to qualitatively observe the effect the copper conversion plate has on planar image quality at both low and high energies. The setup for imaging of the head was as follows: the gantry and couch were rotated to 90°, the imaging panel was placed in a stand located on the couch with fine adjustments screws and leveled to ensure orthogonality of the panel and the beam axis, and the head was centered at isocenter and an SDD of 130 cm. As a result of the increased thickness of the sheep head, compared to the CNR phantom a higher dose was used. All imaging involved an approximate dose of 0.26 cGy delivered to the center of the head. Images were first taken with the copper conversion plate within the detector. The copper plate was then removed and replaced with a 2.1 mm sheet of foam (to ensure adequate compression of the panel assembly) and the detector was reassembled. Images were then acquired without the copper conversion plate present within the detector. Images were analyzed in MATLAB and were compared with identical gray level window settings.

7.4.3 Cone Beam CT Image Quality

CBCT images were acquired using the method described previously by Robar *et al*[17]. As shown in figure 7.9, this involved arranging the beam and detector as described above for planar imaging of the sheep head and rotating the object on a rotation stage consisting of a micro stepping motor (Intelligent Motion Systems, Inc., Marlborough, CT).

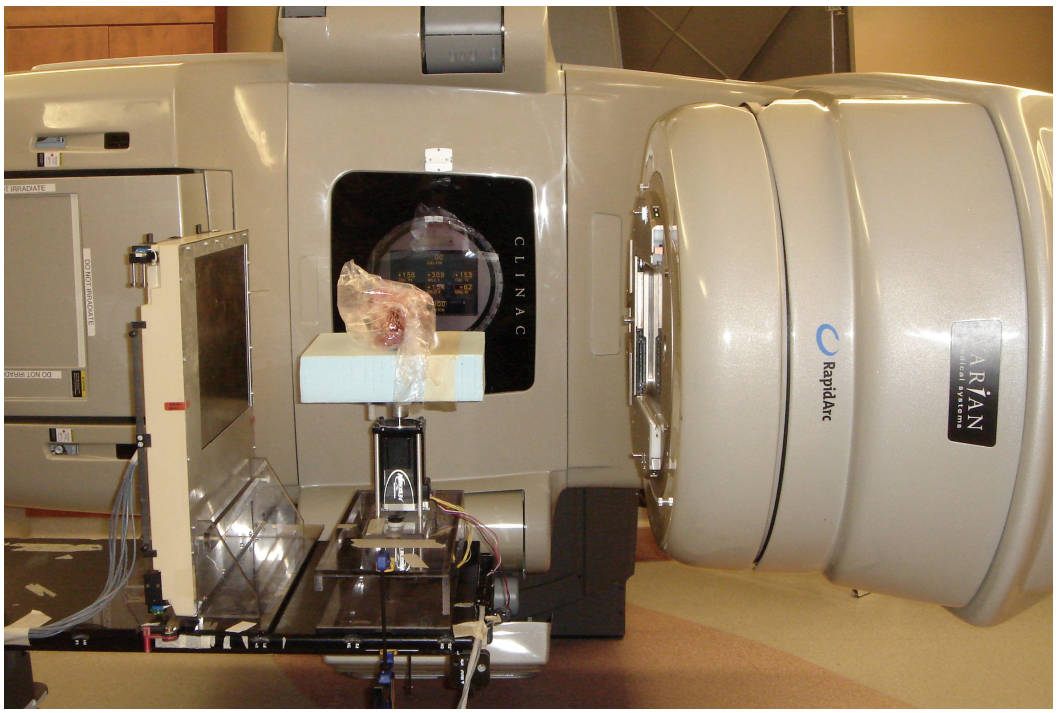

Figure 7.9 The setup for CBCT imaging: the object (sheep head) on the rotation stage situated between the linac head and IDU20.

The rotation stage was aligned such that the axis was at the isocenter. Image acquisition control was accomplished using MATLAB with the Digital I/O toolbox. All projection images were saved in DICOM format and subsequently read by the reconstruction software. Image reconstruction was done using the Feldkamp Davis Kress (FDK) algorithm[45] implemented in MATLAB. The phantom (Fig 7.10) used for CBCT was cylindrical, 12.1 cm in diameter by 6.1 cm in length, composed of polystyrene and contained the same tissue substitutes as described above for planar imaging. Tissue substitute materials were 2.5 cm in diameter and 7 cm in length. CBCT images were acquired both with and without the copper conversion plate present in the detector, with central doses to the phantom ranging from 1.1 to 11.8 cGy. Imaging was repeated for both the 2.35 MV/Carbon and 7.00 MV/Carbon beams. CNR was measured as

described in equation 7.1, with the exception that error bars were calculated by measuring the mean and standard deviation of CNR in three slices above and below the analyzed slice.

Figure 7.10 The CNR phantom used for CBCT with the tissue substitute materials.

To observe qualitative changes, CBCT imaging of the sheep head was done as well, for both beam energies, with and without the copper plate. An approximate imaging dose of 4.1 cGy was delivered to the center of the head located at isocenter. The resultant images were analyzed in MATLAB and were compared with identical gray level window settings.

CHAPTER 8 RESULTS AND DISCUSSION

8.1 BEAM CURRENT MAXIMIZATION

After adjusting the bending magnet shunt current only, with the scattering foil in place, the electron MU rate was approximately 600 MU/min at 2.35 MeV. As shown in figure 8.1, upon altering the voltage of the electron gun and grid to the optimal setting, the MU rate increased to approximately 2800 MU/min. The MU rate gradually decreases as the incident electron energy is decreased to 1.90 MeV, below which a sharp drop was observed from approximately 1400 MU/min to 20 MU/min. Due to this, it does not appear possible to operate at a lower energy with this current setup. With the carbon and aluminum targets in place, a MU rate was observed ranging from 5-9 MU/min and 3-6 MU/min, respectively. Prior to adjustments, this rate was 0-1 MU/min. With these improvements in beam current, it is now possible to acquire multiple low-Z target images per second at doses typical of CBCT projections. It should be noted that the monitor chamber was not calibrated and that these are only relative MU rate measurements. However, with the carbon target in place, a dose rate of 0.7 cGy/min was measured with a 0.125 cm^3 cylindrical ion chamber (PTW N31010, Freiburg, Germany) at an SSD of 95 cm and depth of 5 cm in water for a 10 x 10 cm^2 field (defined at isocenter).

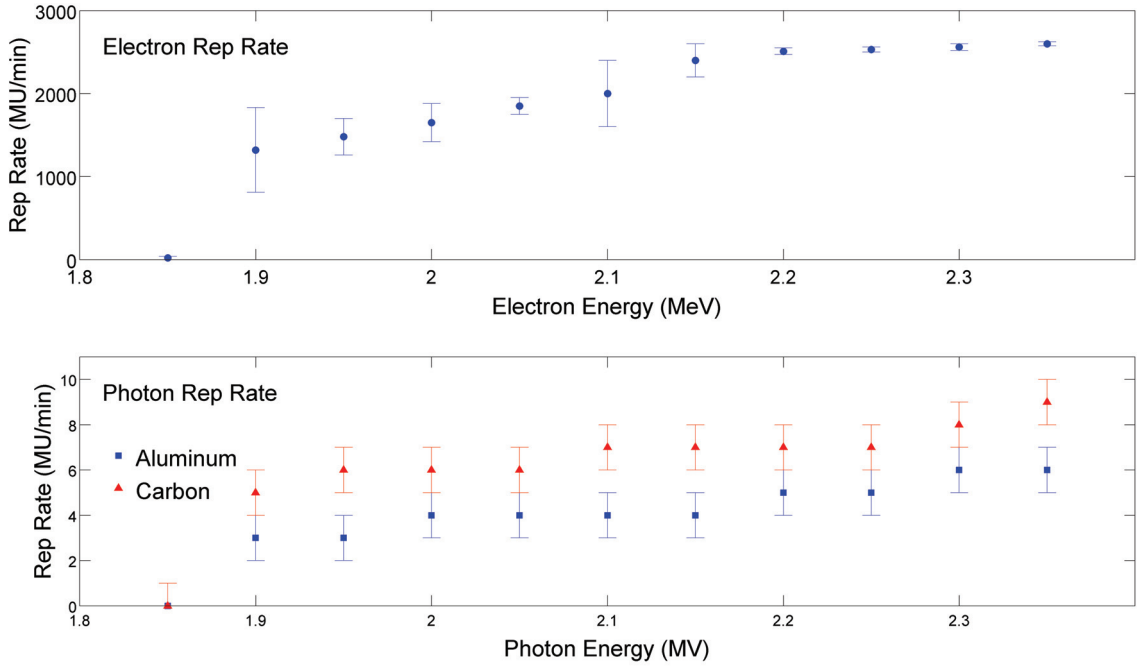

Figure 8.1 MU rate in relation to electron energy for both electrons and photons. The upper plot shows observed MU rate with tantalum scattering foil in place. The lower plot shows observed MU rate with aluminum and carbon targets in place. Error bars are generated from the observed variation in MU rates.

8.2 Incident Electron Energy

Figure 8.2 shows the experimentally measured and Monte Carlo modeled electron PDD curves for energies ranging from 1.90 MeV to 2.35 MeV. The measured and modeled data show excellent agreement in the dose build-up and fall-off region of the PDD, with a slight variation where the central axis depth dose curve meets the bremsstrahlung background. The depth of the 90% PDD (R_{90}) ranges from 2.9 mm to 4.3 mm for 1.90 MeV and 2.35 MeV, respectively. Beyond the build-up region, the dose quickly decreases with R_{50} ranging from 4.2 mm to 6.1 mm for 1.90 MeV and 2.35 MeV, respectively, and the maximum range is less than 9.0 mm for the 2.35 MeV electron

beam. To our knowledge, these are the lowest energy beams used in conjunction with a low-Z target produced with a megavoltage Varian linac[15–17].

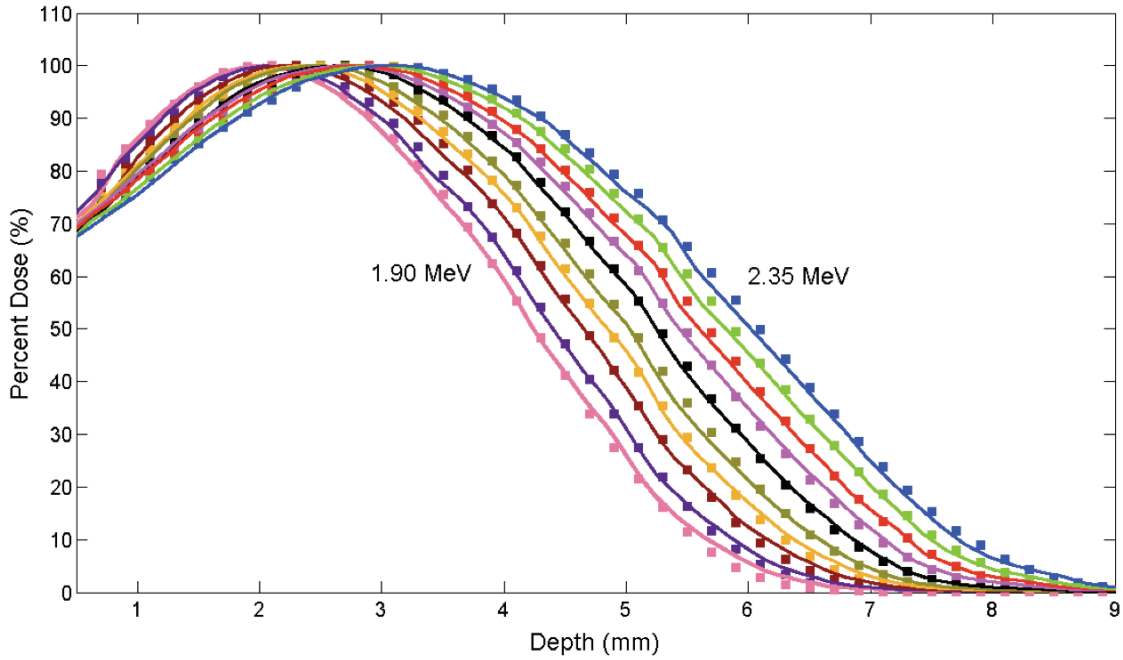

Figure 8.2 Experimental (curves) and Monte Carlo (points) electron percent depth dose curves ranging from 1.90 MeV to 2.35 MeV.

8.3 Photon Beam Characteristics

Figure 8.3 shows measured percent depth dose curves normalized to maximum dose for 1.90 and 2.35 MeV electron beams incident on the aluminum and carbon targets. Also shown are modeled depth dose curves for the aluminum target. Because of the low dose rates produced, relatively few depths were measured compared to the number of modeled depths. As expected, as energy was lowered the dose at a given depth was decreased. At 2.35 MV, we observed d_{max} at 0.6 ± 0.1 cm and 0.4 ± 0.1 cm for the aluminum and carbon targets, respectively. No distinguishable shift in d_{max} towards the surface is observed when decreasing the incident electron energy from 2.35 MV to

1.90 MV. For comparison, Faddegon *et al.*[14] and Sawkey *et al.*[16] reported a d_{max} between 0.9 cm and 1.1 cm for 4.2 MV/Carbon beams, respectively. Compared to the 4.2 MV/Carbon beam generated by Faddegon *et al.*[14], the 2.35 MV/Carbon beam is significantly less penetrating shown by a 25% decrease in percent dose at 10 cm depth. Compared to the 4 MV/Aluminum investigated by Orton and Robar[7], the percentage of photons within the diagnostic energy range was enhanced by approximately 9% and 13% when decreasing the incident electron energy to 2.35 and 1.90 MeV, respectively, on an aluminum target. At a depth of 10 cm, a decrease in percent dose of 20% and 22% was observed when changing the target from aluminum to carbon at 2.35 MV and 1.90 MV, respectively.

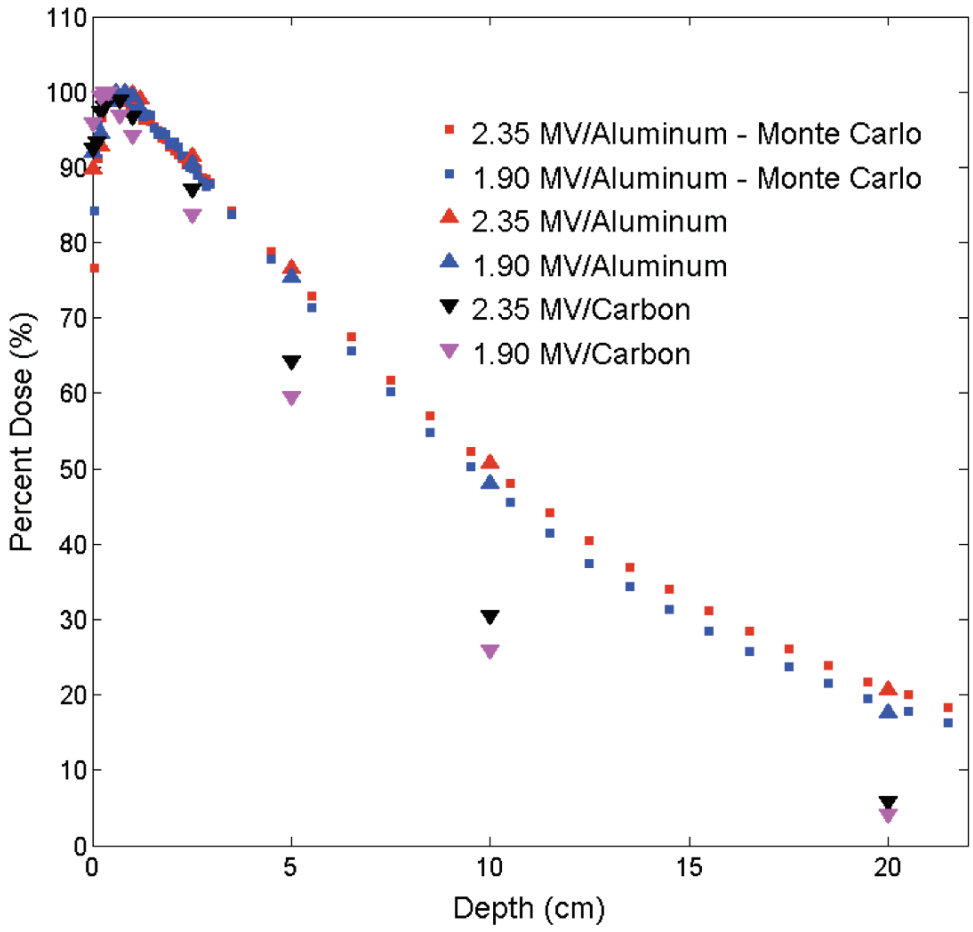

Figure 8.3 Percent depth doses for both aluminum and carbon targets are shown as well as corresponding Monte Carlo modeled depth dose curves for the aluminum target.

These observations indicate that the aluminum target produces a harder beam compared to the carbon target. This is confirmed when examining the spectral distributions shown in figure 8.4, which shows that the mode of the spectrum is shifted from 50 keV to 20 keV when replacing aluminum with carbon, and significantly more photons exist below 40 keV (25% for carbon compared to 6% with aluminum). This is caused by the reduced hardening of the beam through photoelectric absorption, by the lower-Z target material. The mean energies of the four low-Z beams are 202, 240, 312

and 266 keV for the 1.90 MV/Carbon, 2.35 MV/Carbon, 1.90 MV/Aluminum and 2.35 MV/Aluminum beams, respectively.

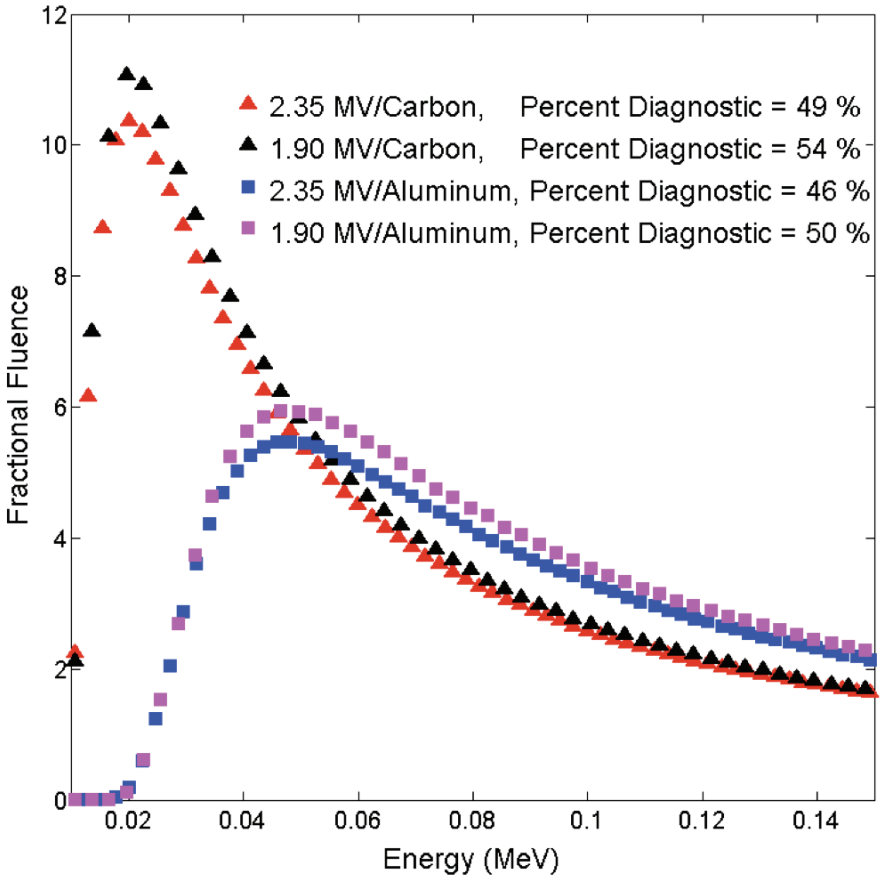

Figure 8.4 Monte Carlo generated spectral distributions for carbon and aluminum targets over the diagnostic energy range (25 to 150 keV), for the maximum and minimum energies used.

Figure 8.5a illustrates the sources of photon generation within the linac. At 2.35 MeV, approximately 12% to 17% of photons are generated within the beryllium exit window of the primary collimator, with 87% to 83% being generated in the aluminum and carbon targets, respectively. The amount of photons generated in the exit window was relatively minor compared to that reported by Roberts *et al.*[15] in an Elekta linac, in which approximately 71% of the beam was generated in the nickel exit window and 28%

in the carbon target. The considerable population of very low energy photons from the carbon target may increase patient dose without contributing to image formation. Figure 8.5b shows 2.35 MV/Carbon spectra for various thicknesses of copper on the exit side of the target. The percentage of photons below 25 keV can be reduced by half with as little as 25 µm of copper.

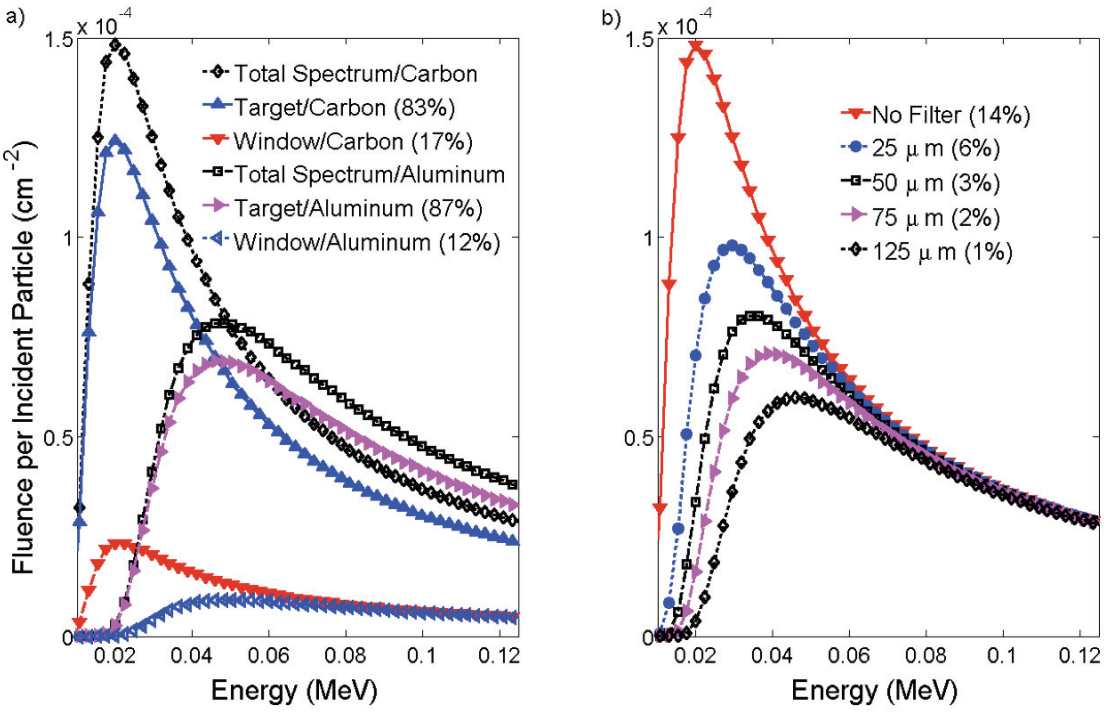

Figure 8.5 Left figure shows Monte Carlo generated spectral distributions for the beryllium exit window and the carbon and aluminum targets, at 2.35 MV. Right figure shows Monte Carlo generated spectral distributions at 2.35 MV for the carbon target with various thickness of copper (on the exit side) and the percentage of photons with energy less than 25 keV.

8.4 PLANAR IMAGE QUALITY

8.4.1 Contrast-to-Noise Ratio

Figure 8.6 shows planar CNR images of the cortical bone insert with 6 MV therapeutic, and 2.35 MV carbon and aluminum beams at 0.01, 0.05 and 0.10 cGy for a thin (3 cm) and a thick (15 cm) phantom. These images show that CNR is improved with increased dose and a decreased phantom thickness and also highlight the difference in image quality between a 6 MV therapeutic beam and the low-Z target beams.

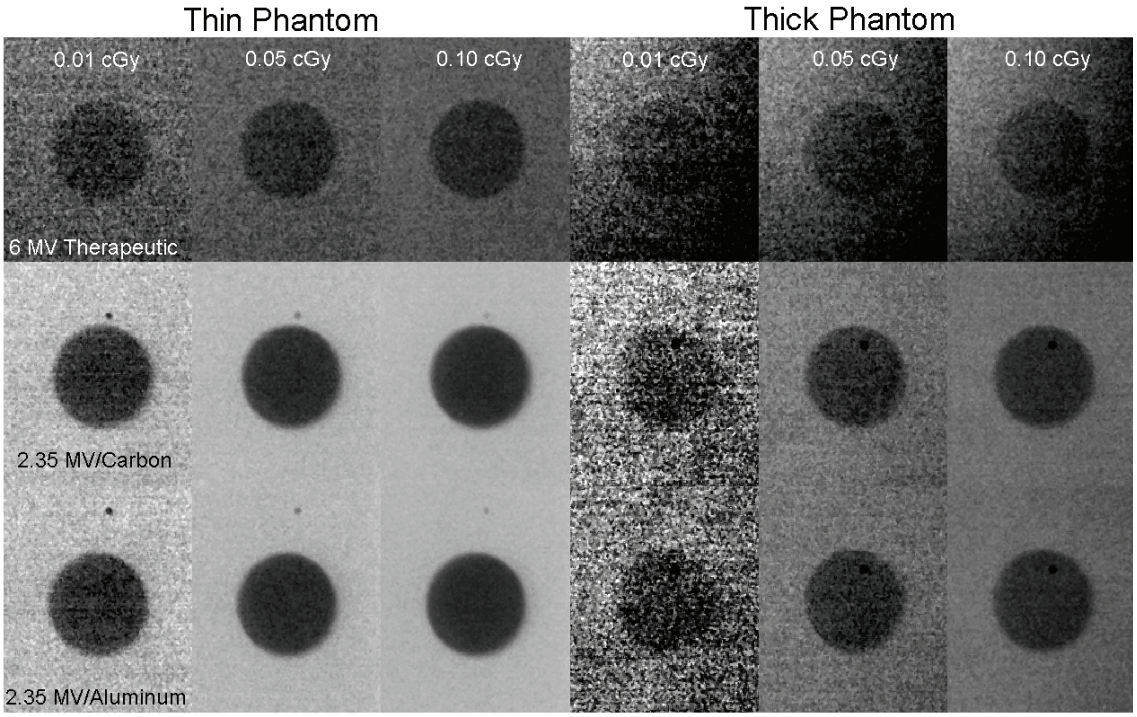

Figure 8.6 Planar images of the cortical bone insert at 2.35 MV with both aluminum and carbon targets and 6 MV therapeutic beam at 0.01, 0.05 and 0.10 cGy for both thin (3 cm) and thick (15 cm) phantoms.

Figure 8.7 shows the corresponding thin phantom CNR results for cortical bone, inner bone, brain and breast inserts as a function of dose at the center of the phantom a for 6 MV therapeutic, 2.35 MV/Carbon and 2.35 MV/Aluminum beam. At approximately 0.05

cGy, CNR values between a 6 MV therapeutic beam and the low-Z target beams were increased by a factor ranging from 6.2 to 7.4, 8.5 to 9.7, 6.7 to 7.5 and 2.2 to 2.7 for cortical bone, inner bone, brain and breast, respectively. It is notable that even for this thin phantom, the CNR values for the 6 MV beam do not exceed 1.0, except for cortical bone. This implies that these objects are not distinguishable from the surrounding medium.

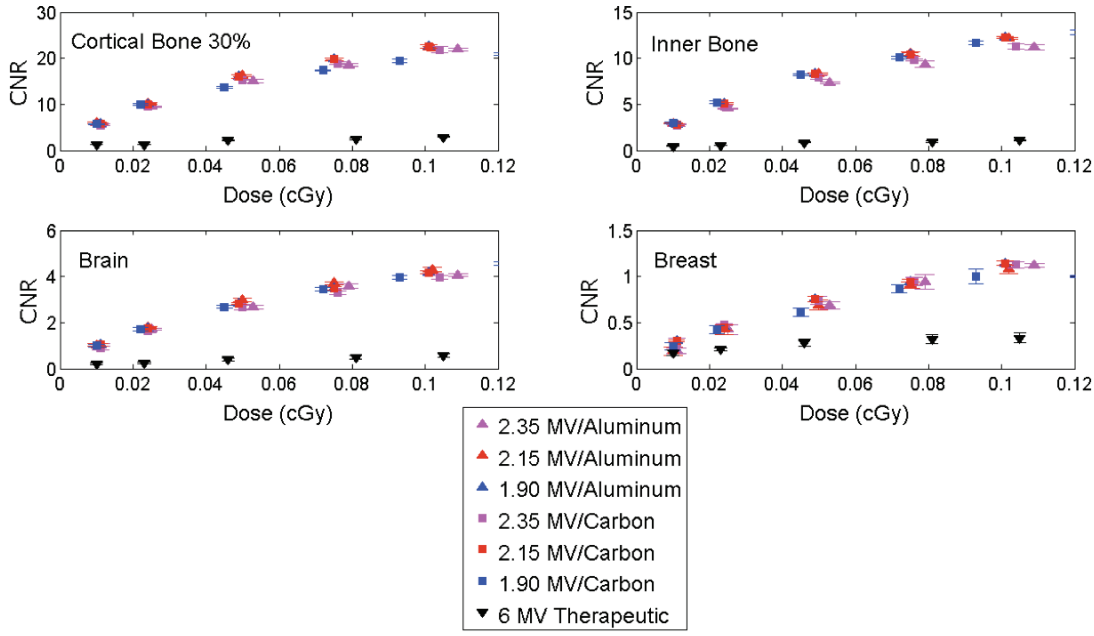

Figure 8.7 Contrast-to-noise ratio results of the thin (3 cm) phantom for the four materials used at 1.90, 2.15 and 2.35 MV with both aluminum and carbon targets. For comparison, a 6 MV therapy beam is also shown.

Figure 8.8 shows the corresponding thick phantom CNR results. At approximately 0.05 cGy, CNR values between a 6 MV therapeutic beam and the low-Z target beams were increased by a factor ranging from 3.7 to 4.3, 5.0 to 6.0 and 7.2 to 10.0 for cortical bone, inner bone, and brain, respectively, with no significant improvement for breast material for the thick phantom. No measureable improvement in CNR was seen with

reduction of energy from 2.35 MV to 1.90 MV, or between target materials, for both thick and thin phantoms. Ideally, an increase in CNR should be observed for the lowest energy and atomic number material[7,9,13,17]. However, figure 8.4 illustrates that the relative increase in photon fluence for carbon is primarily for the spectral component below approximately 50 keV. In this very low energy range, a significant proportion of photons will be absorbed within the phantom or within the copper layer in the detector, thereby not contributing to imaging data[12]. Previous measurements of CNR[9,11–13,15,17] with low-Z target beams have involved a variety of materials and phantom geometries, and therefore it is in general difficult to compare our results directly to CNR values reported in the work of others. However, extrapolating the reduction of measured CNR with the fivefold increase in phantom thickness, we would expect that the gains in planar CNR reported here improved upon the 2.7-3.8 reported by Robar *et al.*[17] for a 22.5 cm thick water phantom. Although this direct comparison is difficult, it is intuitive that increasing the proportion of photons in the diagnostic energy range from 37% reported by Orton and Robar[7] for a 4.0 MV/Aluminum to approximately 50% should improve the CNR characteristics.

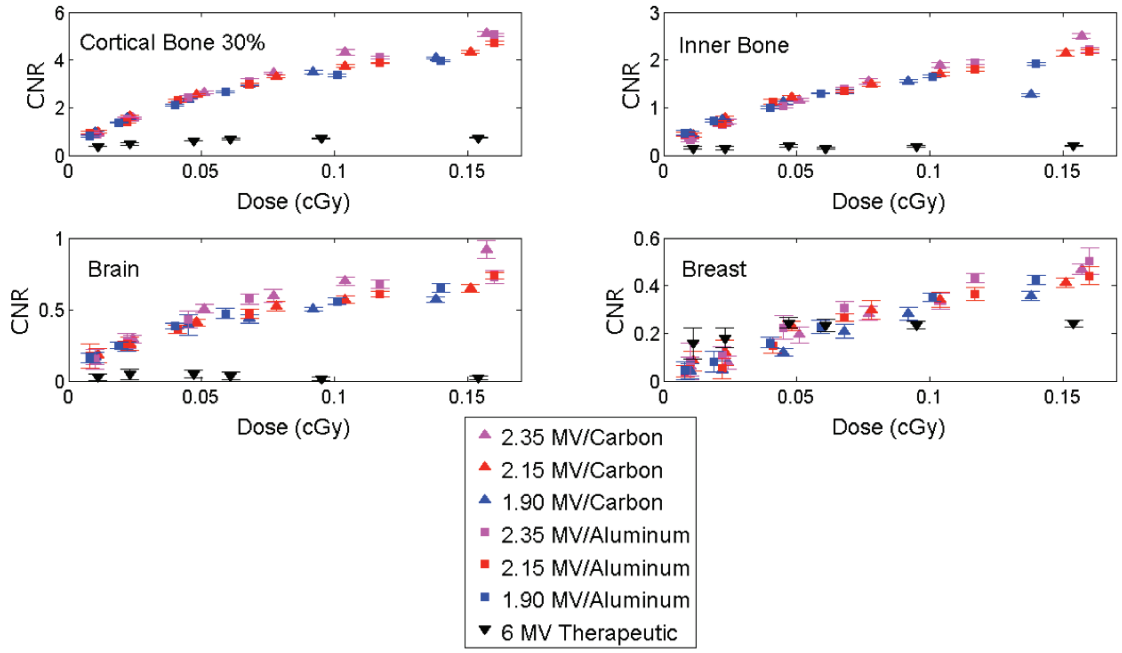

Figure 8.8 Contrast-to-noise ratio results of the thick (15 cm) phantom for the four materials used at 1.90, 2.15 and 2.35 MV with both aluminum and carbon targets. For comparison, a 6 MV therapy beam is also shown.

8.4.2 Spatial Resolution

Figure 8.9 show RMTF curves of the QC3 phantom, for the carbon target at 1.90, 2.15 and 2.35 MV and for the 6 MV therapeutic beam. Measured spatial resolution is consistent with Connell and Robar[18], Roberts *et al.*[15] and Sawkey *et al.*[16], with a spatial frequency of 0.40 lp/mm being distinguishable. Slight degradation of the spatial resolution is apparent with the low energy carbon target beams, compared to 6 MV. The frequency where RMTF equals 0.5, or f_{50}, decreases by approximately 0.1 lp/mm, from 0.42 lp/mm for the 6 MV beam to 0.32 lp/mm for the low-Z beam. With beams of 4.5 MV/Tungsten and 7.0 MV/Beryllium, Connell and Robar[18] showed a relative reduction of f_{50} by 10.4%-15.5% compared to a 6 MV therapeutic beam. As reported by Roberts *et al.*[15] and Connell and Robar[18], the loss of spatial resolution results from larger angle

electron scatter in the target when decreasing incident electron energy. In our data, small decreases of RMTF (by 3% and 10% at 0.20 lp/mm and 0.40 lp/mm, respectively) are observed with a reduction of beam quality from 2.35 to 1.90MV. These are minor changes in RMTF compared to that observed by Connell and Robar[18]; however the work by this group involved a comparatively larger reduction of beam quality, from 7 to 3.5 MV.

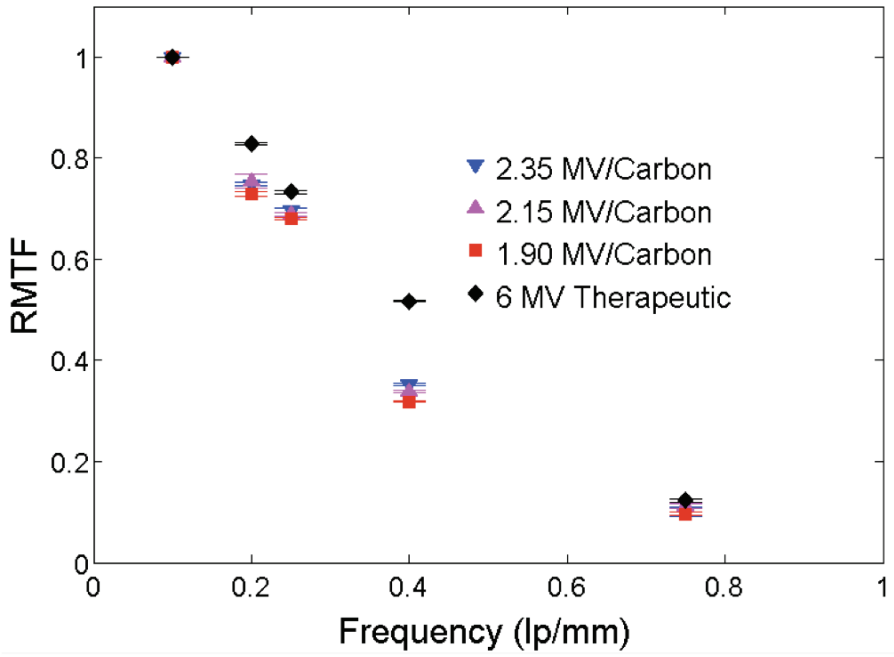

Figure 8.9 Relative modulation transfer function for 1.90, 2.15 and 2.35 MV/Carbon beams and a 6 MV therapeutic beam.

8.4.3 Qualitative Imaging

Figure 8.10 shows planar sagittal images of a sheep head at 2.35 MV with both carbon and aluminum targets and a 6 MV therapeutic beam. Relatively little variation in image quality is observed between the aluminum and carbon targets, which is consistent with the observations above. Images with the 2.35 MV beams show

significant enhancement in image quality compared to a 6 MV therapeutic beam, in both bone and soft tissues. Roberts *et al.*[15] have shown similar gains in planar image quality between their low-Z target beam line and a 6 MV therapeutic beam in planar images of a head and neck phantom.

In summary, given i) that the beam current is maximized at 2.35 MV, thus shortening imaging times, ii) that there is no measurable improvement in CNR compared to the lowest achievable energy and iii) that there is no significant variation in spatial resolution for the carbon target, 2.35 MV appears to be the optimal selection for low-Z target imaging over the range explored here. Based on the observations and constraints encountered in this study, 2.35 MV with a carbon target should be the suggested normal operating energy for further low-Z imaging with this linac.

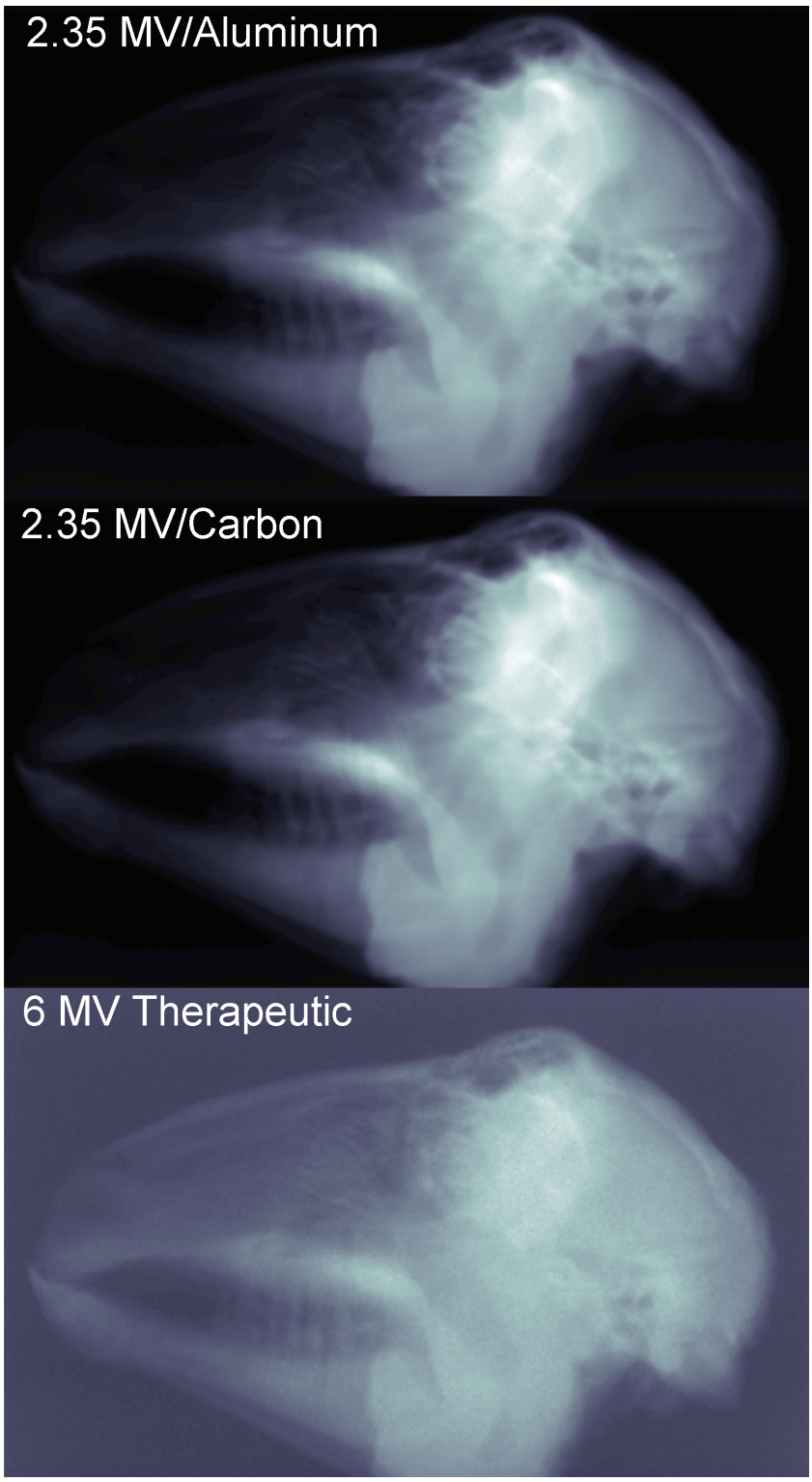

Figure 8.10 Planar sagittal images of a sheep head at 2.35 MV with both carbon and aluminum targets and a 6 MV therapeutic beam.

8.5 Monte Carlo Characterization of the IDU20 with Copper Thickness

Figure 8.11 shows modeled fractional fluences at the exit side of the copper conversion plate, illustrating the effect of various copper thicknesses on the energy spectrum, over the range from 25 keV to 150 keV, for both 2.35 and 7.00 MV/Carbon beams. When increasing copper thickness greater than 0 mm, the fluence below 100 keV is significantly attenuated, and accordingly the percentage of diagnostic photons is reduced.

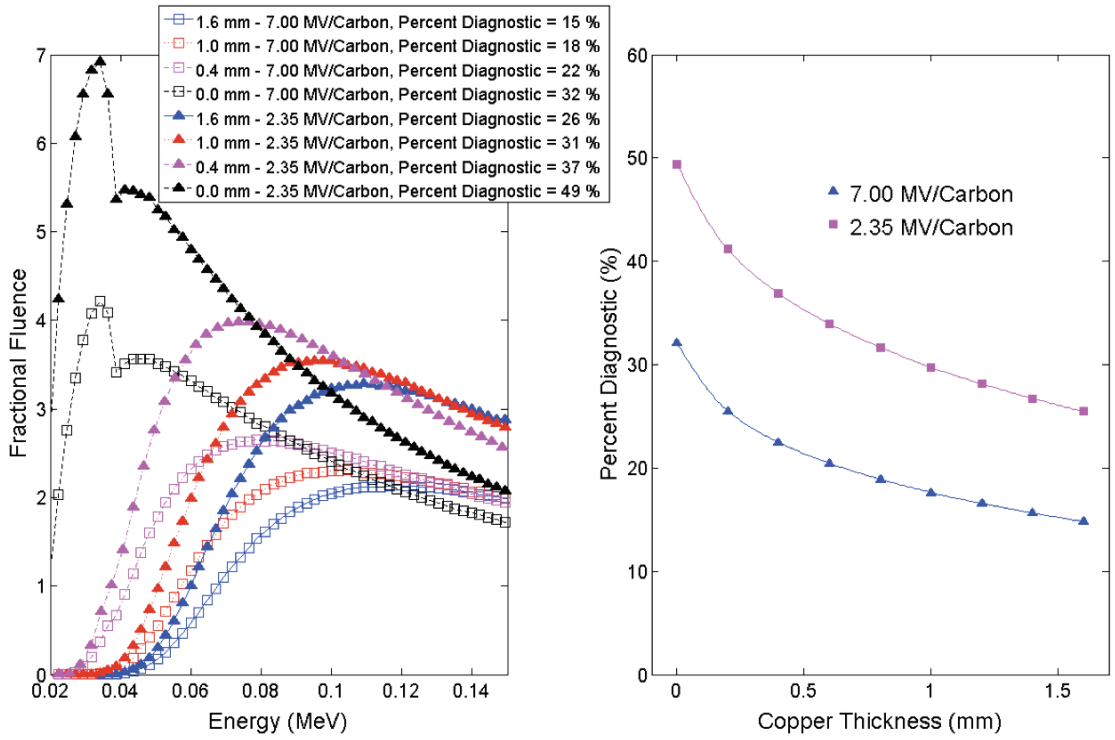

Figure 8.11 a) shows the diagnostic spectral distribution with 0 mm, 0.4 mm, 1.0 mm and 1.6 mm of copper present in the detector for 2.35 MV/Carbon and 7.00 MV/Carbon beams. b) shows the percentage of photons within the diagnostic energy domain (25 to 150 kV) at the phosphor surface as a function of copper thickness.

It should also be noted that for the copper-free cases, the increase in fluence below 38 keV in the spectra was due to the presence of barium (k-edge at 37.45 keV) within the detector cover. For the 2.35 MV/Carbon beam, the diagnostic photon population (25 keV to 150 keV) was decreased by 20% with the standard 1.0 mm copper conversion plate in place, compared to 0 mm of copper. A corresponding 15% decrease was observed for the 7.00 MV/Carbon beam.

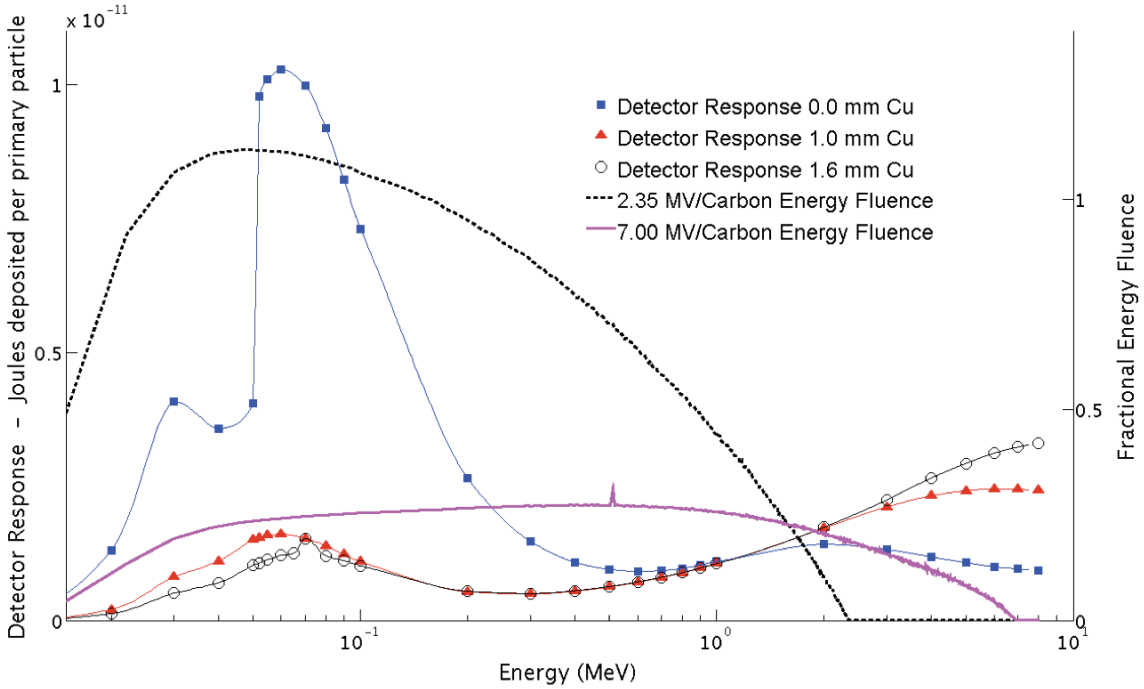

Figure 8.12 Response curves for 0 mm, 1.0 mm and 1.6 mm thick copper layers within the IDU20 and photon energy fluence produced with the 2.35 MV/Carbon and 7.00 MV/Carbon beams.

Figure 8.12 illustrates the energy response of the IDU20 with various thicknesses of copper, as well as the photon spectra produced with the 2.35 and 7.00 MV/Carbon beams. With no copper present in the IDU20, detector response peaks at approximately 60 keV and decreases rapidly with increasing photon energy. When copper was placed

within the IDU20, the response at 60 keV was suppressed by factors of 6.4 and 8.5 for 1.0 mm and 1.6 mm thicknesses, respectively. At 0.8 MeV the response was approximately the same regardless of copper thickness, above which the responses diverge with increasing energy. This figure demonstrates that the 2.35 MV/Carbon beam contains a substantial fluence of photons within the peak detector response region (approximately 30 to 120 keV). For the 7.00 MV/Carbon beam, peak fluence occurs at approximately 400 keV, at which point the response is locally minimized for the copper-less detector. In summary, the results of Figures 8.11 and 8.12 indicate that copper removal is advantageous for either low-Z target beam with regard to maximizing the diagnostic population reaching the phosphor, and particularly for the 2.35 MV/Carbon beam, for which the energy spectrum is well matched to the detector response. The detector response curves shown here agree with similar results given by Roberts *et al.*[15] and Faddegon *et al.*[14] for an Elekta iViewGT (Elekta AB, Stockholm, Sweden) and a Perkin Elmer XRD 1640 AG9 panel (Perkin Elmer, Inc., Waltham, MA), respectively. Both of these detectors include a 1.0 mm copper plate, a gadolinium oxysulphate scintillating layer and an array of photodiodes[22,51]. Both authors have shown that a high-Z scintillating material strongly interacts with the diagnostic portion of the energy spectrum. Roberts *et al.*[15,21] also show the detector response for an Elekta XVI panel (Elekta AB, Stockholm, Sweden), which differs substantially in design, with the omission of a copper conversion plate and replacement of the gadolinium oxysulphate scintillating layer by columnar, thallium doped, caesium iodide (CsI:Tl) crystal. The responses of this detector and the IDU20 without copper are similar in that they share a

peak response at approximately 50 to 70 keV and a local minimum between approximately 500-600 keV, with the main difference in responses being in energies less than 40 keV.

8.6 Planar Image quality with Copper Thickness

8.6.1 Contrast-to-Noise Ratio

Figure 8.13 shows image CNR as a function of copper thickness for various tissue equivalent materials. For most materials, with the exception of lung, image CNR decreases quickly with the addition of the first few 0.2 mm thick layers of copper and approaches a relatively constant CNR value beyond 0.8 mm of copper. The rapid degradation in CNR with the first few layers corresponds to the decrease in the diagnostic fluence with copper shown in figure 8.11; both the fluence in the diagnostic range and CNR show the largest decreases with the addition of the first 0.4 mm of copper. With no copper present, image CNR was increased by factors of 1.6, 2.3, 3.2, 1.4 and 2.3 for cortical bone 60%, cortical bone 30%, inner bone, brain and lung, respectively, compared to the standard 1.0 mm of copper. Similar gains in CNR were observed for the 7.00 MV/Carbon beam, with factor increases ranging from 1.6 to 4.0, however, the absolute values of CNR were typically less than half of those observed at 2.35 MV. The results presented here confirm the modeled results of Orton and Robar[7], in that a gain in image contrast was observed with the removal of the copper layer.

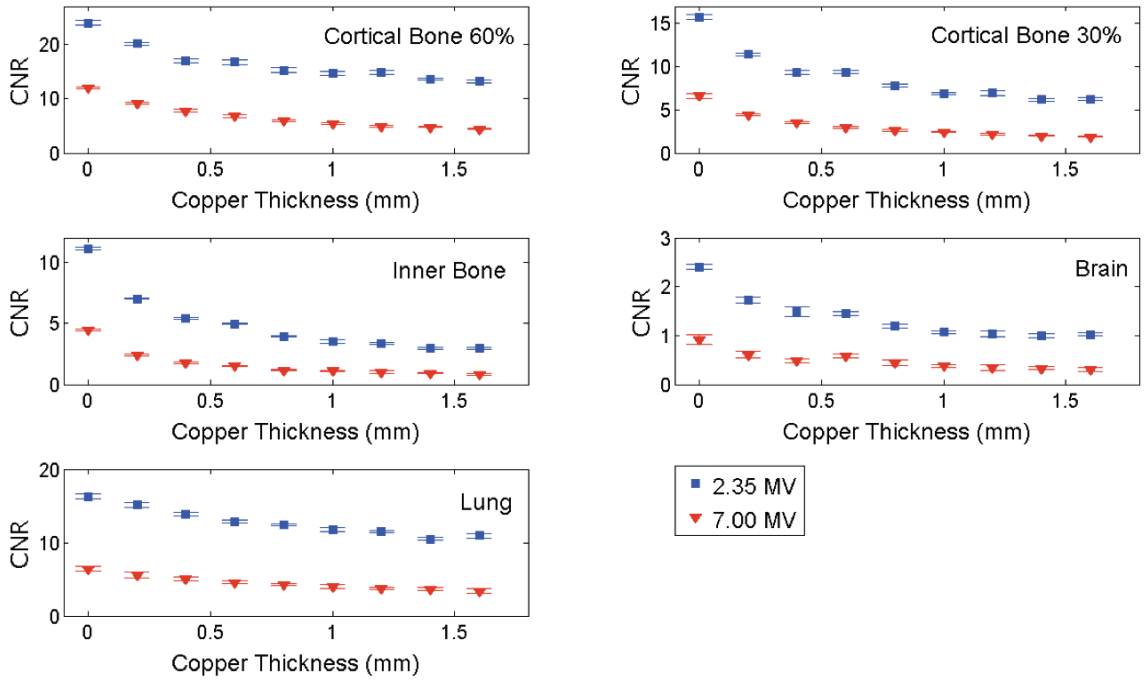

Figure 8.13 Planar image contrast-to-noise ratio as a function of copper thickness for both 2.35 MV/Carbon and 7.00 MV/Carbon beams, for cortical bone 0% (top-left), cortical bone 30% (top-right), inner bone (middle-left), brain (middle-right) and lung (bottom-left).

8.6.2 Spatial Resolution

Figure 8.14 shows RMTF at various thicknesses of copper for the 2.35 and 7.00 MV/Carbon beams. At most frequencies there appears to be little variation with changing copper thickness. At 0.25 lp/mm, there is a detectable but small change in RMTF, with relative improvement of RMTF by 18% and 15% for the 2.35 and 7.00 MV/Carbon beams, with removal of the 1.0 mm copper layer. The frequency where RMTF equals 0.5, or f_{50}, did not vary significantly with copper removal for either low-Z target beam. With the 1.0 mm copper layer, a decrease is seen in f_{50} of 0.03 lp/mm when reducing electron energy from 7.00 to 2.35 MeV. In comparison, Connell and

Robar[18] reported a change in f_{50} of approximately 0.02 and 0.03 lp/mm for beryllium and aluminum target beams, when reducing the incident electron energy from 7.0 to 4.5 MeV.

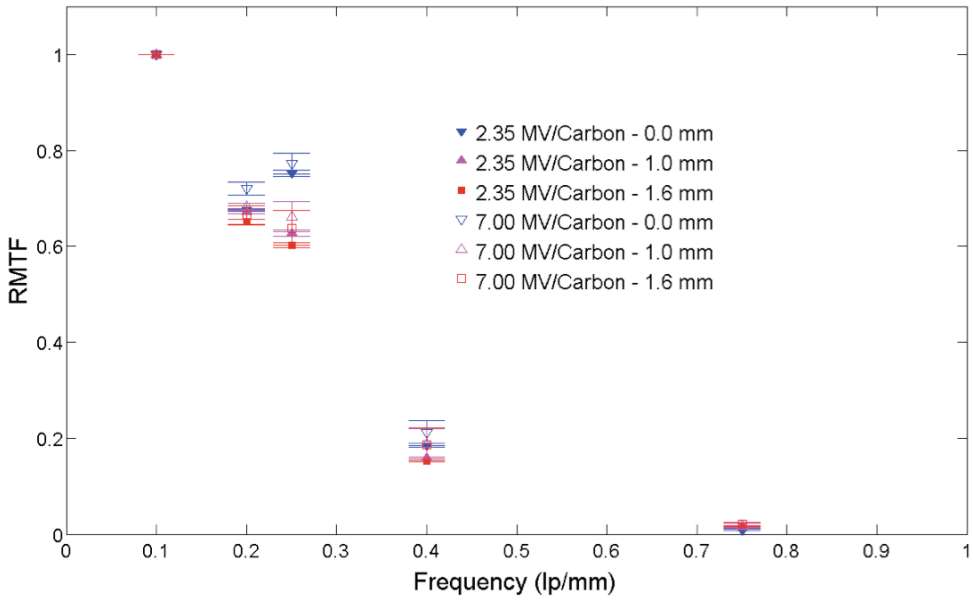

Figure 8.14 Relative modulation transfer function (RMTF) for 0.0mm, 1.0 mm and 1.6 mm thick copper layers in the IDU20 detector for 2.35 MV/Carbon and 7.00 MV/Carbon beams.

8.6.3 Qualitative Imaging

Figure 8.15 shows planar sagittal sheep images both with and without the copper conversion plate for the 2.35 and 7.00 MV/Carbon beams. The images show increased image contrast with the removal of the copper conversion plate, compared to images with the copper conversion plate in place. This is most noticeable within the sqaumous, nasal and mandible regions. Since these changes in image quality are relatively minor between the four images, the differences are highlighted in the profiles shown in figure 8.16, in which the contrast is notably increased with the removal of the

copper conversion plate for the 2.35 MV/Carbon beam. Figure 8.16 also shows slight loss of fine detail when using the 2.35 MV/Carbon beam compared to 7.00 MV/Carbon. As noted by Connell and Robar[18], this is largely a result of electron beam broadening when decreasing incident electron energy.

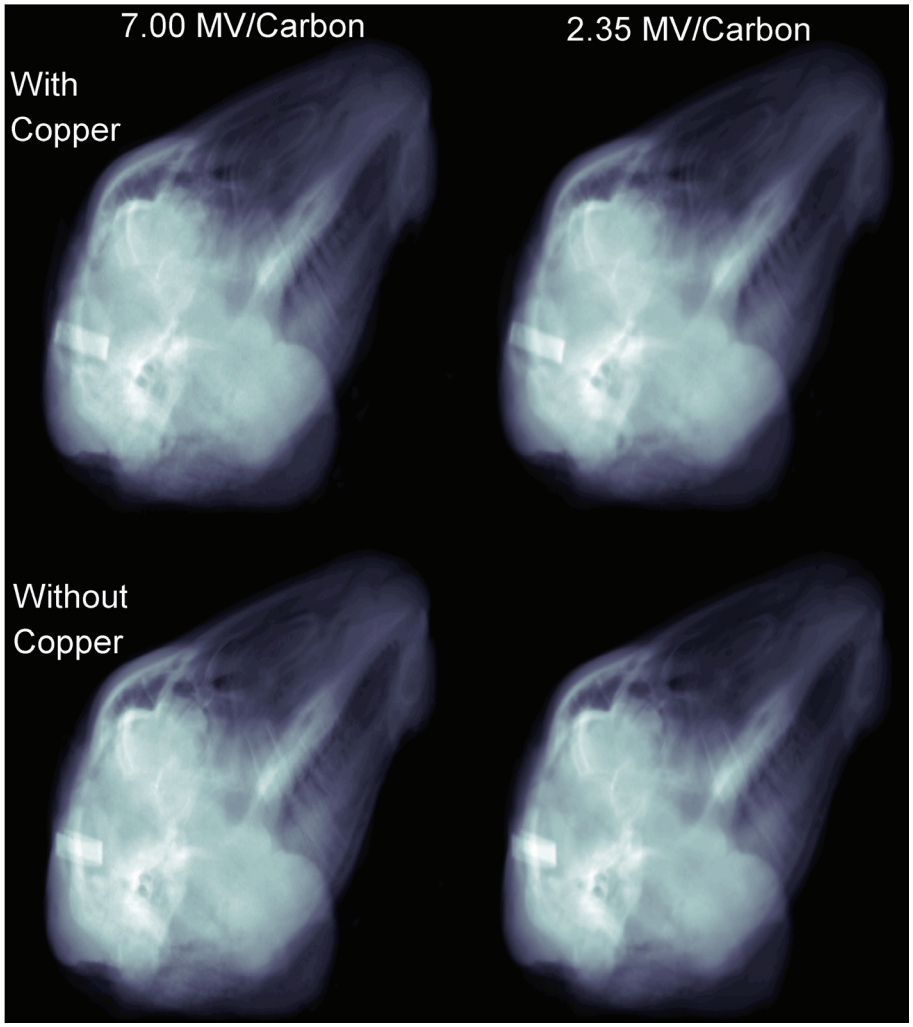

Figure 8.15 Planar imaging of a sheep head at 0.26 cGy (at isocenter) for both 0.0 mm (right) and 1.0 mm (left) of copper within the detector at both 2.35 (bottom) and 7.00 MV/Carbon (top). For comparison, the images where normalized to the pixel value at a point within all the images and with identical gray level window settings.

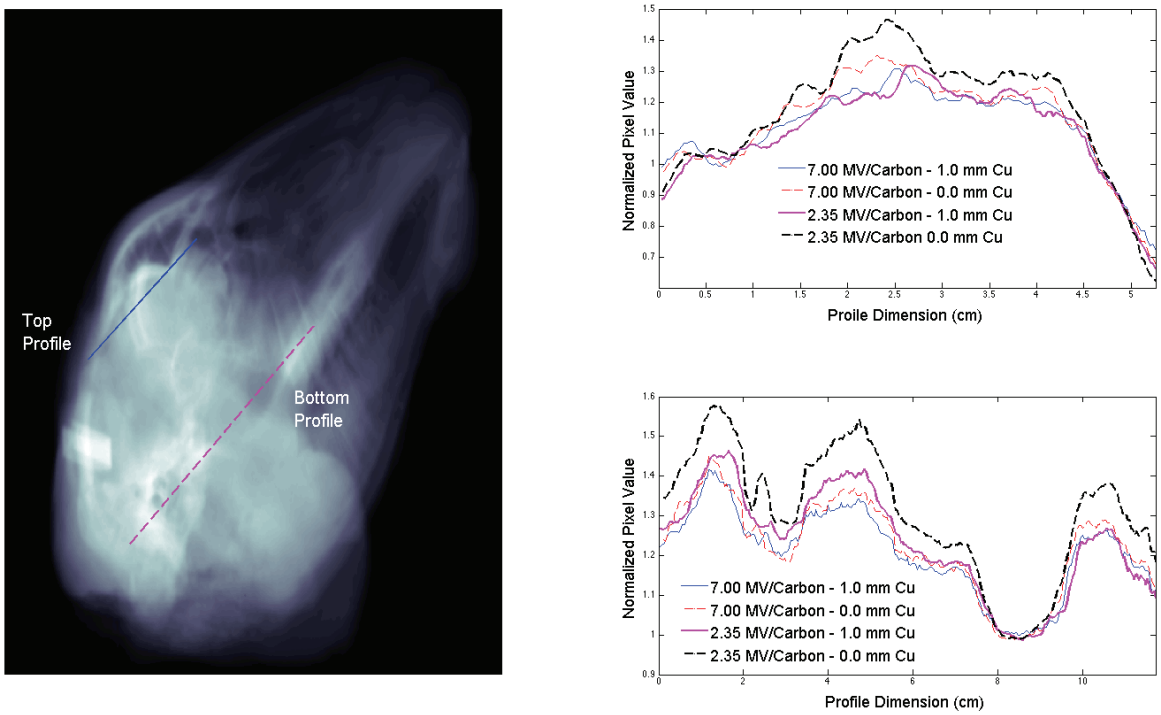

Figure 8.16 Profiles of figure 8.15 with and without the copper conversion plate within the detector for 2.35 MV/Carbon and 7.00 MV/Carbon beams.

8.7 Cone Beam CT Image Quality with Copper Thickness

8.7.1 Contrast-to-Noise Ratio

Figure 8.17 shows CBCT images of tissue equivalent materials in polystyrene both with and without copper using the IDU20 for the 2.35 MV/Carbon and 7.00 MV/Carbon beams. The CBCT images show greater contrast with the copper conversion plate removed for both 7.00 and 2.35 MV/Carbon, with the greatest improvement seen for 2.35 MV/Carbon. This is evident also in the corresponding CNR curves as a function of dose, shown in Figure 8.18. At approximately 4.1 cGy and for the 2.35 MV/Carbon beam, for example, copper removal produced improvement of CNR by factors of 1.5, 1.9, 2.1, 1.4 and 1.3 for cortical bone 60%, cortical bone 30%, inner bone, brain and

lung, respectively. Similar factor increases are seen for the 7.00 MV/Carbon beam, but as for the planar imaging results, CNR values are typically half of that observed for 2.35 MV/Carbon.

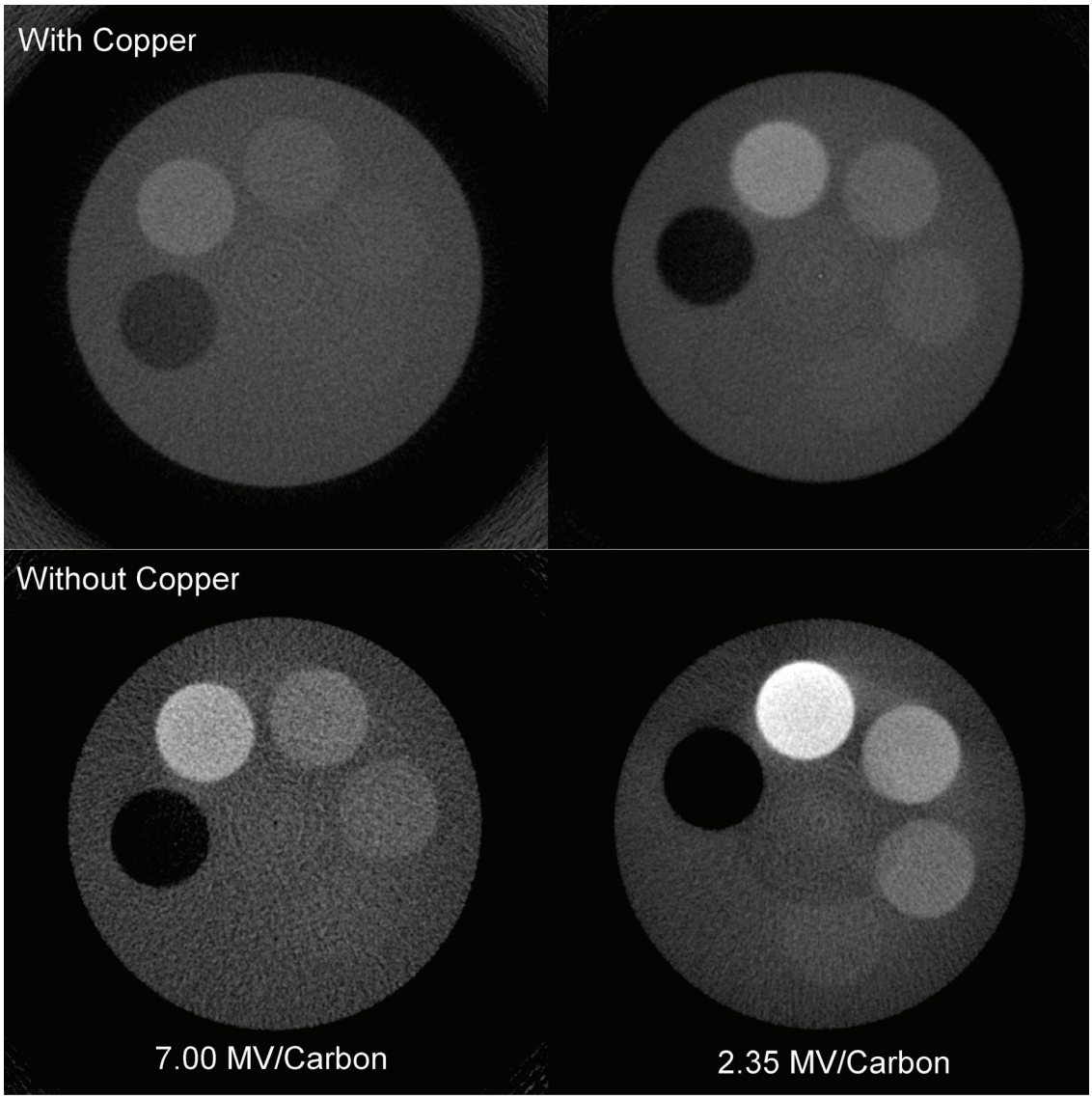

Figure 8.17 Cone beam computed tomography images at approximately 4.1 cGy with copper plate (top) and without copper (bottom) in the detector, with the 7.00 MV/Carbon and 2.35 MV/Carbon beams.

The CNR improvement with copper removal seen here are comparable in magnitude to the factor 1.64 gain in CNR observed by Breitbach *et al.*[23] when using a

segmented ceramic Gb_2S_2O scintillator, compared to a standard 1.0 mm copper conversion plate with Gb_2S_2O scintillating phosphor. However, this group used a different beam-line[14] within a Siemens linac at 4.2 MV.

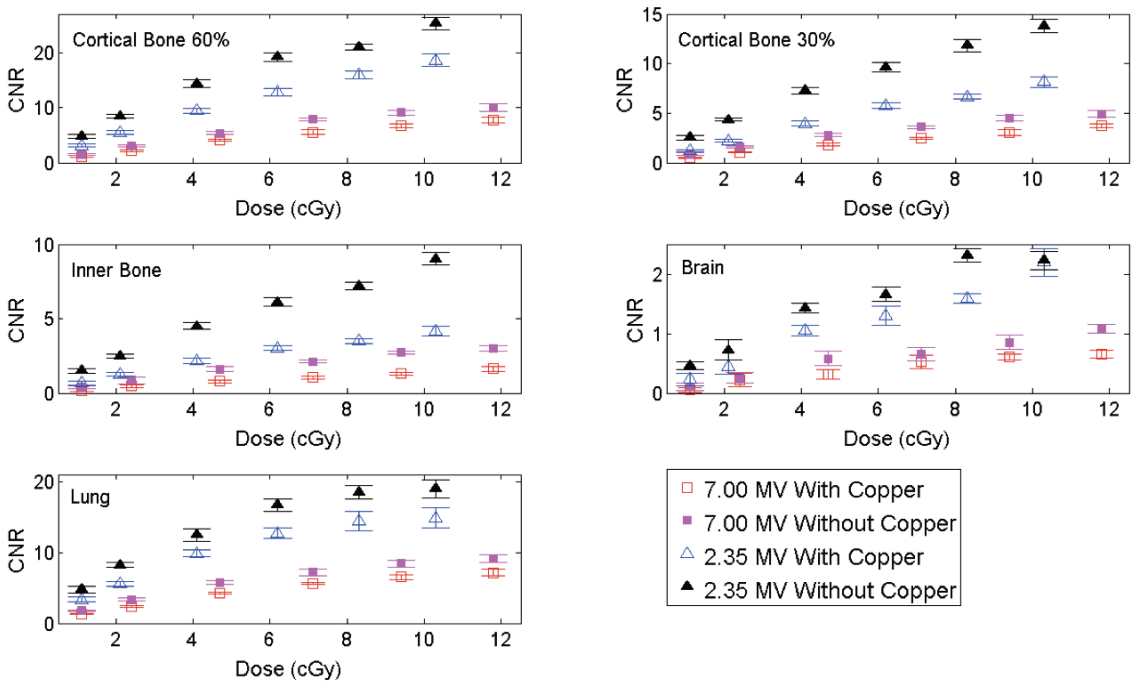

Figure 8.18 Contrast-to-noise ratios of tissue substitutes in CBCT images as a function of dose, comparing the 2.35 MV/Carbon and 7.00 MV/Carbon beams both with and without copper present in the detector.

8.7.2 Qualitative Imaging

Figure 8.19 shows axial CBCT images of the sheep head with and without the copper conversion plate for the 2.35 MV/Carbon and 7.00 MV/Carbon beams. These images highlight the effect the presence of copper in the IDU20 has on image contrast-to-noise characteristics. This can be seen in the bony structures of the skull and in the nasal cavity. When imaged with the 2.35 MV/Carbon beam, these structures are clearly visualized without copper present, compared to the image acquired with the copper

layer. These trends are also present in the 7.00 MV/Carbon images, however, the CNR is clearly degraded. These images taken here agree with the qualitative findings reported by Faddegon *et al.*[14], in which there is an overall improvement in bone and soft tissue visibility with copper removal; however, in this work we show that the reduction of energy to 2.35 MeV offers an overall improvement in image quality. While we believe that a more efficient detector, such as a crystalline scintillator, would be preferable[15,21], these results demonstrate that substantial improvements in image quality may be realized with a standard MV EPID following removal of the copper conversion plate. It should be noted that the ring artifacts present in figures 8.17 and 8.19 are due to defects within the detector when imaged with a low-Z target beam. This is caused by an imperfect dark field correction of images by the acquisition system.

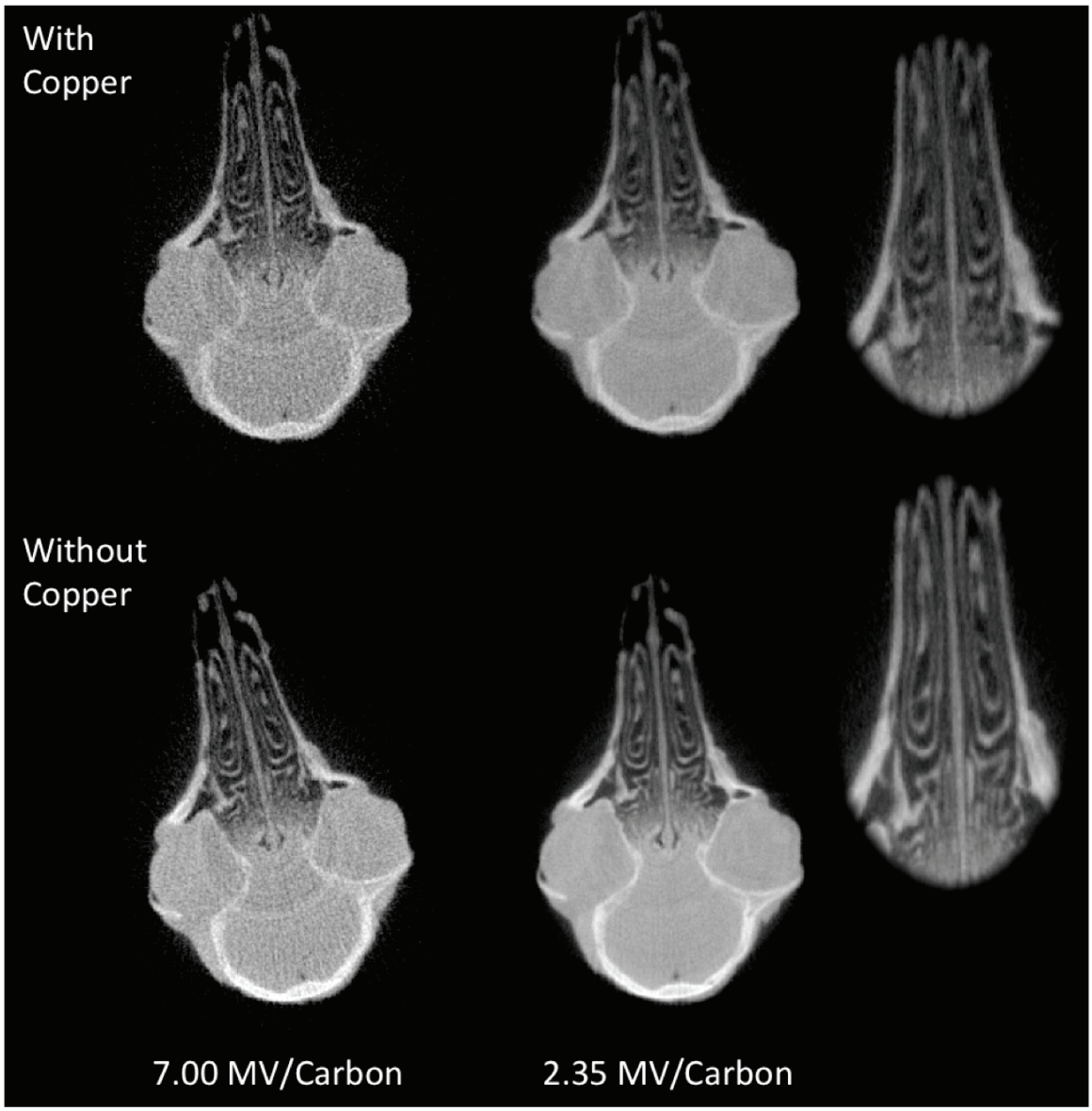

Figure 8.19 CBCT images of a sheep head at approximately 4.1 cGy (at isocenter) with copper plate (top) and without copper (bottom) in the detector, the 7.00 MV/Carbon (left) and 2.35 MV/Carbon (center) beams. The two images on the right are magnified views of the nasal cavity for the 2.35 MV/Carbon beam.

CHAPTER 9 CONCLUSIONS

9.1 SUMMARY OF WORK

9.1.1 Beam Optimization

In this work, it has been shown that it is possible to decrease the incident electron energy produced by a Varian 2100EX linac to values ranging from 1.90 MeV to 2.35 MeV. In electron mode, beam current can be increased from approximately 600 MU/min to 2800 MU/min by altering set points of the electron gun, grid, solenoid and bunching magnets, thereby deceasing image acquisition times. While it is possible to lower the incident electron energy further, below 1.90 MeV, the beam current falls sharply to an impractical value. Lowering the incident electron energy and increasing the beam current has optimized the photon beams for imaging, yielding approximately 50% of generated photons within the diagnostic energy domain. For both aluminum and carbon targets this allowed an approximate increase in CNR of cortical bone ranging from 6.2 to 7.4 and 3.7 to 4.3 for a thin and thick phantom, respectively, compared to 6 MV therapy beam. Slight relative decreases by 3% and 10% at 0.20 lp/mm and 0.40 lp/mm, respectively, were observed in spatial resolution when lowering from 2.35 MV to 1.90 MV. Planar images of a sheep head showed that the 2.35 MV carbon and aluminum target beams produced enhancements to image quality compared to a 6 MV therapeutic beam, in both bone and soft tissues. Based on the observations and constraints encountered in this study, 2.35 MV with a carbon target should be the suggested normal operating energy for further low-Z imaging with this linac.

9.1.2 Detector Optimization

In this work, it has been shown that the removal of the copper conversion plate within an IDU20 EPID can significantly improve image contrast and CNR when used in conjunction with low-Z target imaging beams. The presence of the copper conversion plate caused a decrease in the diagnostic population by 20% and 15% for 2.35 MV/Carbon and 7.00 MV/Carbon, beams, respectively. Removal of the copper conversion plate caused the peak response within the detector to improve by a factor of 6.4. Planar images acquired with a copper-less detector showed a factor gain in CNR ranging from 1.4 to 3.2 and 1.6 to 4.0, for 2.35 MV/Carbon and 7.00 MV/Carbon beams, respectively, compared to the standard 1.0 mm of copper. Similar gains in CNR were observed in CBCT images, where CNR was improved by a factor ranging from 1.3 to 2.1. Spatial resolution for either beam was not affected significantly by copper removal. Qualitative imaging of a sheep head showed that there was an increase in planar and CBCT image contrast with a copper-less detector. From this work it is clear that the copper plate should be removed in future low-Z imaging.

9.2 Current and Future Work

9.2.1 Volume-of-Interest CBCT

Using the 2.35 MV/Carbon beam line, a proof of concept paper regarding volume of interest (VOI) CBCT has been published by Robar *et al*[52]. In this work, the MLC is used to truncate the beam at each projection to image only a selected volume. Data can then be recovered from truncation artefacts by filling each projection with either digitally

reconstructed radiographs (DRR) or extrapolation. This work has shown that the dose inside and outside the VOI can be reduced by 15% and 75%, respectively. However, no noticeable gains in image CNR were observed using the VOI technique. More complex VOIs are currently being developed and investigated such as multiple and nested VOIs.

9.2.2 Integration of Low-Z beams to treatment planning software

It is of interest to integrate the 2.35 MV/Carbon beam into Varian's Eclipse treatment planning system. This would allow the dose to be accurately modelled and the imaging dose to be incorporated with the planned therapeutic dose. Due to the long acquisition times observed in measuring PDDs for this work, the commissioning data needed for Eclipse has been obtained through Monte Carlo simulations. Currently work is being done to integrate the commissioning data into Eclipse.

9.2.3 Crystalline Based Detector Imaging

Roberts *et al*.[15,21] have previously shown that a caesium iodine based crystalline detector in combination with a reduced energy carbon target beam, can produce significant gains in image quality compared to a 6 MV therapeutic beam with a traditional copper-Gb_2O_2S based Elekta iViewGT. It would be of interest to measure image quality with the 2.35 MV/Carbon beam line and a similar crystalline detector.

9.2.4 Integration with TrueBeam

Two new TrueBeam linacs are currently being installed at the Nova Scotia Cancer Centre. The TrueBeam linacs are a redesigned version of the older Varian linacs, with one major difference being that the waveguide has a continuous energy switch (as

opposed to two energy switch settings at 6 and 18 MeV). This means that electrons could exit the waveguide with a significantly reduced kinetic energy. Roberts *et al*[21]. have previously shown that a continuously variable energy range is possible within an Elekta linac waveguide coupled to a device called a rotovane. With this it is possible to produce electron kinetic energies as low as 1.4 MeV. However, to date the low energy range of a Varian Truebeam waveguide has yet to be fully investigated.

BIBLIOGRAPHY

[1]E. J. Hall and A. J. Giaccia, *Radiobiology for the Radiologist*, 6th ed. (Lippincott Williams & Wilkins, Philadelphia, PA, 2006), p. 656.

[2]Canadian Cancer Society, Statistics Canada, and Public Health Agency of Canada, "Canadian Cancer Statistics 2012," (2012).

[3]American Society for Radiation Oncology, "Statistics," (2010).

[4]F. H. Attix, *Introduction to Radiological Physics and Radiation Dosimetry* (Wiley, 1986).

[5]E. B. Podgorsak, *Radiation Physics for Medical Physicists* (Springer, 2006).

[6]W. R. Hendee and E. R. Ritenour, *Medical Imaging Physics*, Fourth (Wiley-Liss, Inc., New York, NY, 2002).

[7]E. J. Orton and J. L. Robar, "Megavoltage image contrast with low-atomic number target materials and amorphous silicon electronic portal imagers," Phys. Med. Biol. **54**, 1275–1289 (2009).

[8]D. A. Jaffray, J. H. Siewerdsen, J. W. Wong, and A. A. Martinez, "Flat-panel cone-beam computed tomography for image-guided radiation therapy," Int. J. Radiat. Oncol., Biol., Phys., **53**, 1337–1349 (2002).

[9]D. M. Galbraith, "Low-energy imaging with high-energy bremsstrahlung beams," Med. Phys. **16**, 734–746 (1989).

[10]D. W. Mah, D. M. Galbraith, and J. A. Rawlinson, "Low-energy imaging with high-energy bremsstrahlung beams: analysis and scatter reduction," Med. Phys. **16**, 653–665 (1993).

[11]O. Z. Ostapiak, P. F. O'Brien, and B. A. Faddegon, "Megavoltage imaging with low Z targets: implementation and characterization of an investigational system," Med. Phys. **25**, 1910–1918 (1998).

[12]A. Tsechanski, A. F. Bielajew, S. Faermann, and Y. Krutman, "A thin target approach for portal imaging in medical accelerators," Phys. Med. Biol. **43**, 2221–2236 (1998).

[13]S. Flampouri, P. M. Evans, F. Verhaegen, A. E. Nahum, E. Spezi, and M. Partridge, "Optimization of accelerator target and detector for portal imaging using Monte Carlo simulation and experiment," Phys. Med. Biol. **47**, 3331–3349 (2002).

[14]B. A. Faddegon, V. Wu, J. Pouliot, B. Gangadharan, and A. Bani-Hashemi, "Low dose megavoltage cone beam computed tomography with an unflattened 4 MV beam from a carbon target," Med. Phys. **35**, 5777–5786 (2008).

[15]D. A. Roberts, V. N. Hansen, A. C. Niven, M. G. Thompson, J. Seco, and P. M. Evans, "A low Z linac and flat panel imager: comparison with the conventional imaging approach," Phys. Med. Biol. **53**, 6305–6319 (2008).

[16]D. Sawkey, M. Lu, O. Morin, M. Aubin, S. S. Yom, A. R. Gottschalk, A. Bani-Hashemi, and B. A. Faddegon, "A diamond target for megavoltage cone-beam CT," Med. Phys. **37**, 1246–1253 (2010).

[17]J. L. Robar, T. Connell, W. Huang, and R. G. Kelly, "Megavoltage planar and cone-beam imaging with low-Z targets: Dependence of image quality improvement on beam energy and patient separation," Med. Phys. **36**, 3955–3963 (2009).

[18]T. Connell and J. L. Robar, "Low-Z target optimization for spatial resolution improvement in megavoltage imaging," Med. Phys. **37**, 124–131 (2010).

[19]M. F. Fast, T. Koenig, U. Oelfke, and S. Nill, “Performance characteristics of a novel megavoltage cone-beam-computed tomography device.,” Phys. Med. Biol. **57**, N15–N24 (2012).

[20]D. A. Roberts, V. N. Hansen, M. G. Thompson, G. Poludniowski, A. Niven, J. Seco, and P. M. Evans, “Comparative study of a low-Z cone-beam computed tomography system,” Phys. Med. Biol. **56**, 4453–4464 (2011).

[21]D. A. Roberts, V. N. Hansen, M. G. Thompson, G. Poludniowski, A. Niven, J. Seco, and P. M. Evans, “Kilovoltage energy imaging with a radiotherapy linac with a continuously variable energy range,” Med. Phys. **39**, 1218–26 (2012).

[22]B. A. Faddegon, M. Aubin, A. Bani-Hashemi, B. Gangadharan, A. R. Gottschalk, O. Morin, D. Sawkey, V. Wu, and S. S. Yom, “Comparison of patient megavoltage cone beam CT images acquired with an unflattened beam from a carbon target and a flattened treatment beam,” Med. Phys. **37**, 1737–1741 (2010).

[23]E. K. Breitbach, J. S. Maltz, B. Gangadharan, A. Bani-Hashemi, C. M. Anderson, S. K. Bhatia, J. Stiles, D. S. Edwards, and R. T. Flynn, “Image quality improvement in megavoltage cone beam CT using an imaging beam line and a sintered pixelated array system,” Med. Phys. **38**, 5969–5979 (2011).

[24]D. A. Jaffray, J. J. Battista, A. Fenster, and P. Munro, “Monte Carlo studies of x-ray energy absorption and quantum noise in megavoltage transmission radiography,” Medical Physics **22**, 1077–88 (1995).

[25]National Institute of Standards and Technology, “Stopping power and ranges for electrons,” (2011).

[26]E. J. Orton, Improved Contrast in Radiation Therapy Imaging Using low-Z Targets and Amorphous Silicon Portal Imagers, Dalhousie University, 2008.

[27]National Institute of Standards and Technology, "Tables of X-Ray Mass Attenuation Coefficients and Mass Energy-Absorption Coefficients from 1 keV to 20 MeV for Elements Z = 1 to 92 and 48 Additional Substances of Dosimetric Interest," (2011).

[28]C. J. Karzmark, C. S. Nunan, and E. Tanabe, *Medical Electron Accelerators*, First Edit (McGraw-Hill, New York, NY, 1993), p. 316.

[29]E. B. Podgorsak, *Radiation Oncology Physics: A Handbook for Teachers and Students* (International Atomic Energy Agency, Vienna, Austria, 2005).

[30]J. J. Wood and W. P. M. Mayles, "Factors affecting the precision of TLD dose measurements using an automatic TLD reader.," Phys. Med. Biol. **40**, 309–313 (1995).

[31]T. Radcliffe, G. Barnea, B. Wowk, R. Rajapakshe, and S. Shalev, "Monte Carlo optimization of metal/phosphor screens at megavoltage energies," Med. Phys. **20**, 1161–9 (1993).

[32]C. Kausch, B. Schreiber, F. Kreuder, R. Schmidt, and O. Dössel, "Monte Carlo simulations of the imaging performance of metal plate/phosphor screens used in radiotherapy," Medical Physics **26**, 2113–24 (1999).

[33]L. E. Antonuk, "Electronic portal imaging devices: a review and historical perspective of contemporary technologies and research.," Phys. Med. Biol. **47**, R31–R65 (2002).

[34]D. W. O. Rogers, "Fifty years of Monte Carlo simulations for medical physics.," Physics in Medicine and Biology **51**, R287–301 (2006).

[35]A. F. Bielajew, H. Hirayama, W. R. Nelson, and D. W. O. Rogers, *History, Overview and Recent Improvements of EGS4 Technical Report PIRS-0436* (NRCC, Ottawa, Canada, 1994).

[36]I. Kawrakow, E. Mainegra-Hing, D. W. O. Rogers, F. Tessier, and B. R. B. Walters, *The EGSnrc Code System: Monte Carlo Simulation of Electron and Photon Transport NRCC Report PIRS-701* (NRCC, Ottawa, Canada, 2011).

[37]I. Kawrakow, "Accurate condensed history Monte Carlo simulation of electron transport. I. EGSnrc, the new EGS4 version," Med. Phys. **27**, 485–498 (2000).

[38]D. W. Rogers, B. A. Faddegon, G. X. Ding, C. M. Ma, J. We, and T. R. Mackie, "BEAM: a Monte Carlo code to simulate radiotherapy treatment units," Med. Phys. **22**, 503–524 (1995).

[39]C. M. Ma and D. W. O. Rogers, *BEAMdp Users Manual NRCC Report PIRS-0509(C)revA* (NRCC, Ottawa, Canada, 2009).

[40]D. Sheikh-Bagheri, I. Kawrakow, B. Walters, and D. W. O. Rogers, in *Integrating New Technologies into the Clinic: Monte Carlo and Image-Guided Radiation Therapy—Proceedings of 2006 AAPM Summer School* (Medical Physics Publishing, Madison, WI, 2006), pp. 71–91.

[41]D. W. O. Rogers, B. Walters, and I. Kawrakow, *BEAMnrc Users Manual NRCC Report PIRS-0509(A)revL* (NRCC, Ottawa, Canada, 2011).

[42]I. Kawrakow, D. W. O. Rogers, and B. R. B. Walters, "Large efficiency improvements in BEAMnrc using directional bremsstrahlung splitting," Medical Physics **31**, 2883–2898 (2004).

[43]A. C. Kak and M. Slaney, *Principles of Computerized Tomographic Imaging* (IEEE Press, 1988), pp. 49–112.

[44]S. W. Smith, *The Scientist and Engineer's Guide to Digital Signal Processing. The Scientist and Engineer's Guide to Digital Signal Processing* (California Technical Pub, San Diego, CA, 1998).

[45]L. Feldkamp, L. Davis, and J. Kress, "Practical cone-beam algorithm," JOSA A **1**, 612–619 (1984).

[46]J. Wei, G. A. Sandison, and A. V. Chvetsov, "Reconstruction of electron spectra from depth doses with adaptive regularization," Med. Phys. **33**, 354–359 (2006).

[47]J. O. Deasy, P. R. Almond, and M. T. McEllistrem, "Measured electron energy and angular distributions from clinical accelerators," Med. Phys. **23**, 675–684 (1996).

[48]B. W. Wessels, B. R. Paliwal, M. J. Parrott, and M. C. Choi, "Characterization of Clinac-18 electron-beam energy using a magnetic analysis method," Med. Phys. **6**, 45–48 (1979).

[49]R. Rajapakshe, K. Luchka, and S. Shalev, "A quality control test for electronic portal imaging devices," Med. Phys. **23**, 1237–1244 (1996).

[50]R. T. Droege and R. L. Morin, "A practical method to measure the MTF of CT scanners," Med. Phys. **9**, 758–760 (1982).

[51]L. Parent, J. Seco, P. M. Evans, A. Fielding, and D. R. Dance, "Monte Carlo modelling of a-Si EPID response: The effect of spectral variations with field size and position," Med. Phys. **33**, 4527 (2006).

[52]J. L. Robar, D. Parsons, A. Berman, and A. Macdonald, “Volume-of-interest cone-beam CT using a 2.35 MV beam generated with a carbon target,” Med. Phys. **39**, 4209–4218 (2012).